Development and Model Application of a Surface- Site- Based Parametrization Framework for Heterogeneous Ice Nucleation

Zur Erlangung des akademischen Grades eines
DOKTORS DER NATURWISSENSCHAFTEN
von der Fakultät für Physik des
Karlsruher Instituts für Technologie (KIT)

genehmigte

DISSERTATION

von

Dipl.-Met. Romy Ullrich

Tag der mündlichen Prüfung: 28. Oktober 2016

Referent: Prof. Dr. Corinna Hoose

Korreferent: Prof. Dr. Thomas Leisner

Abstract

Heterogeneous ice nucleation plays an important role in both mixed- phase and pure ice clouds. In mixed- phase clouds at temperatures above about 238 K, the threshold temperature for the freezing of pure water droplets, all primary ice particles are formed by heterogeneous ice nucleation processes. At lower temperatures in the upper troposphere, however, homogeneous freezing of solution droplets and heterogeneous ice nucleation compete with each other to form pure ice clouds, so- called cirrus clouds. This competition determines the number concentration and size of ice crystals, and thereby the life cycle and optical properties of the cirrus clouds. When simulating clouds, the amount of nucleated ice in dependence of parameters like temperature, humidity and aerosol concentration has to be parametrized in models. In order to develop such parametrizations, comprehensive laboratory and/ or field measurements are needed.
Based on results of 11 years of heterogeneous ice nucleation experiments at the AIDA cloud chamber, a new empirical parametrization framework for heterogeneous ice nucleation was developed as part of this thesis. The framework currently includes desert dust and soot aerosol and quantifies the ice nucleation efficiency in terms of the INAS approach which formulates the ice nucleation activity as a function of the aerosol surface area. This new framework was then implemented into the COSMO- ART model in order to simulate a cirrus cloud in a case study.

The evaluation algorithm for calculating the INAS densities was improved by two extensions yielding to somewhat higher INAS densities compared to previously derived INAS densities.
For desert dust aerosol, the immersion freezing INAS densities n_S follow an exponential fit, well in agreement with an earlier analysis of AIDA experiments. For soot aerosol particles almost no ice nucleation activity was observed in the immersion freezing mode. Therefore, only upper limits for n_S are determined and used to rescale an existing parametrization line.
Below water saturation and at temperatures below about 240 K, the ice nucleation activity in the deposition nucleation mode was also described by an INAS density

which now depends on both the temperature T and the ice saturation ratio S_i. The experimental results were approximated with the following formula

$$n_S(T, S_i) = \exp\left(\alpha\ (S_i - 1)^{1/4}\ \cos\left(\beta\,(T - \gamma)\right)^2\ \mathrm{arccot}\left(\kappa\,(T - \lambda)\right)\right)\ ,$$

where the parameters α, β, γ, κ and λ are specific for the aerosol type. According to the experimental results, the n_S isolines show u- shaped curves in the $S_i - T-$ diagram with positive slopes at higher temperatures, negative slopes at lower temperatures, and a transition regime in between where the n_s value is almost independent of temperature. The negative slopes towards lower temperatures may be explained by Classical Nucleation Theory, whereas the behavior towards higher temperatures may be caused by a pore condensation and freezing mechanism. For desert dust aerosol, the transition occurs at about 205 K, for soot aerosol with a low organic carbon content at about 220 K. In the pore condensation and freezing regime, the n_S isolines for soot aerosol particles are much steeper than for desert dust particles. In the deposition nucleation regime, the n_S values for soot with a higher organic carbon content are shifted towards higher S_i compared to soot with a low organic carbon content.
The new parametrization framework is compared to the empirical framework implemented in the COSMO- ART model. The comparison shows large differences in shape and magnitude of the n_S isolines especially for deposition nucleation. At temperatures below about 240 K, the new framework tends to predict higher n_S values compared to the default scheme. Within the cirrus cloud case study, the new framework therefore predicted more heterogeneously formed and less homogeneously formed ice particles than the other framework. In comparison to aircraft measurements (MACPEX campaign 2011), however, the model tends to underestimate the aerosol load in the flight region and therewith underpredicts the influence of heterogeneous ice nucleation for both frameworks.

Kurzzusammenfassung

Heterogene Eisbildung spielt eine entscheidene Rolle in Mischphasenwolken und reinen Eiswolken. In Mischphasenwolken und bei Temperaturen oberhalb von etwa 238 K, der Grenztemperatur für das Gefrieren reiner Wassertröpfchen, werden fast alle Eispartikel durch heterogene Nukleation gebildet. Bei niedrigeren Temperaturen in der oberen Troposhäre stehen homogenes Gefrieren von Lösungstropfen und heterogene Eisbildung hingegen im ständigen Wettbewerb während der Bildung von reinen Eiswolken, so genannten Zirren. Dieser Wettbewerb bestimmt die Anzahlkonzentration und Größe der Eispartikel, und damit die Lebensdauer und die optischen Eigenschaften des Zirrus. Für die Simulation von Wolken muss die Menge an nukleiertem Eis in Abhängigkeit von Temperatur, Feuchtegehalt und Aerosolmenge parametrisiert werden. Um solche Parameterisierungen entwickeln zu können sind umfassende Labor- und/ oder Feldmessungen nötig.
Basierend auf 11 Jahren Experimente in der AIDA Wolkenkammer zur heterogenen Eisbildung wurde ein neues, empirisches Parameterisierungschema für die heterogene Eisbildung entwickelt. Das Schema umfasst zur Zeit Wüstenstaub Aerosole und Ruß Aerosole und quantifiziert die Eisbildungseffizienz mit dem INAS Ansatz, der die Eisbildungsaktivität als Funktion der Aerosoloberfläche beschreibt. Dieses neue Schema wurde dann in das COSMO- ART Modell implementiert, um eine Eiswolke in einer Fallstudie zu simulieren.

Zunächst wurde jedoch ein neuer Algorithmus zur Auswertung der Experimente entwickelt, der die Abnahme der Gesamtaerosoloberfläche aufgrund unvollständiger Aerosol-zu- Tröpfchen- Aktivierung und die zeitliche Abnahme der Gesamtaerosoloberfläche durch die Eisbildung berücksichtigt.
Die INAS Dichten n_S für das Immersionsgefrieren auf Wüstenstaub folgen einem exponentiellen Verlauf, der mit einer früheren Analyse von AIDA Experimenten gut übereinstimmt. Für Rußpartikel wurde nur schwache Eisbildung im Immersionsgefrier-Bereich beobachtet. Deshalb wurden nur obere Grenzen für die INAS Dichte bestimmt und genutzt, um eine bestehende Parameterisierungskurve zu reskalieren.
Unterhalb der Wassersättigung und Temperaturen unterhalb von 240 K wurde die Eis-

bildungsaktivität auch mit der INAS Dichte beschrieben, die im Depositionsnukleations-Bereich von Temperatur und Eissättigungsverhältnis abhängt. Die experimentellen Ergebnisse wurden durch folgende Formel approximiert

$$n_S(T, S_i) = \exp\left(\alpha\ (S_i - 1)^{1/4}\ \cos\left(\beta\,(T - \gamma)\right)^2\ \mathrm{arccot}\left(\kappa\,(T - \lambda)\right)\right)\ ,$$

wobei die Parameter α, β, γ, κ und λ spezifisch für den Aerosoltyp sind. Bezugnehmend auf die experimentellen Ergebnisse zeigen die n_S Isolinien einen u- förmigen Verlauf im $S_i - T-$ Diagramm mit positiver Steigung bei hohen Temperaturen, negativer Steigung bei niedrigen Temperaturen, und einem Übergangsbereich dazwischen, in dem die n_S Werte kaum von der Temperatur abhängen. Die negative Steigung bei niedrigeren Temperaturen können mit der Klassischen Nukleationstheorie erklärt werden, während die positive Steigung bei höheren Temperaturen wohlmöglich durch einen Porenkondensations- und Porengefriermechanismus hervorgerufen werden. Für Wüstenstaubpartikel liegt der Übergangsbereich bei etwa 205 K, für Rußpartikel bei etwa 220 K. Oberhalb dieses Übergangsbereich sind die n_S Isolinien für den Ruß sehr viel steiler als für den Wüstenstaub. Bei der Depositionsnukleation von Rußpartikel sind die n_S Werte für Ruß mit einem höheren Anteil an organischen Kohlenstoff, im Vergleich zu Ruß mit einem geringen Anteil, zu höheren Eisübersättigungen verschoben.
Das neue Parameterisierungsschema wird mit dem emprischen Schema, welches im COSMO- ART Modell implementiert ist, verglichen. Im Vergleich zeigen sich vorallem für die Depositionsnukleation große Unterschiede in Form und Größenordnung der n_S Isolinien. Bei Temperaturen unterhalb von 240 K sagt das neue Schema dabei höhere n_S Werte voraus als das Standardschema. In der Zirrus- Fallstudie ergaben sich daher für das neue Schema mehr heterogen gebildete und weniger homogen gebildete Eispartikel als für das Standardschema. Im Vergleich zu Flugzeugmessungen (MACPEX Kampagne 2011) unterschätzt jedoch das Modell die Aerosolmenge in der Messregion und -höhe und unterschätzt damit den Einfluss von heterogener Eisbildung bei beiden Schemas.

Contents

1. Introduction

Ever since mankind weather controlled the evolution of whole cultures. Since ancient people realized the connection between clouds, precipitation and the actual weather situation, they tried to understand and predict the formation of clouds. Therefore, they were capable to adjust their hunting, seeding and harvesting to the annual cycle of the weather. This culminates in the effort to actively influence the weather by making clouds rain. In spite of many contributions in understanding cloud physics, there are still open questions like the formation of ice in clouds which this work is dedicated to.
A cloud is defined as „a visible aggregate of minute water droplets and/ or ice particles in the atmosphere above the earth's surface"(American Meteorological Society, 2016). According to this definition two ice containing types of clouds are distinguished: mixed-phase clouds and pure ice clouds. During the lifetime of mixed- phase clouds, the minute particles grow to precipitating particles. Thereby, 50 % of all global precipitation events are initiated by ice particles, emphasizing the crucial relevance of ice formation in clouds. In this case, initially warm clouds become supercooled and subsequently glaciated (e.g. Ansmann et al., 2008). In this terms, glaciation means the transformation of supercooled cloud droplets to ice particles. Once ice particles are present, they rapidly grow due to the Wegener- Bergeron- Findeisen (WBF) process. The WBF process describes the deposition growth of ice particles caused by the evaporation of cloud droplets in mixed- phase clouds. This process is driven by the difference in the saturation water vapor pressure over ice and supercooled water. However, the temperature and humidity conditions in mixed- phase clouds require so- called *ice nucleating particles* (INPs), which initiate the phase transformation from liquid water to ice.
In contrast to mixed- phase clouds the nucleation process is different in pure ice clouds. In this case the water vapor directly deposits on the INP's surface. While pure ice clouds generally do not form precipitating particles, these clouds are of interest because of their diverse radiative effect (Kärcher and Spichtinger, 2009).
In general, not all aerosol particles in the atmosphere serve as INPs. Airborne condensates suspended in the air are called aerosol, whereas aerosol particles refer to the solid particles. Solid aerosol particles are insoluble naturally or anthropogenically emitted particles like dust, soot or pollen, or crystalline organics. Liquid particles, however,

are mixtures of condensed trace gases. In this context, INPs are defined as the subset of the solid aerosol particles which act as an ice nucleation initiating particle. Ice nucleation initiated by such an INP is called *heterogeneous ice nucleation*. Thereby, heterogeneous ice nucleation is distinguished by freezing of supercooled droplets e.g. with immersed INP (*immersion freezing*) and by deposition of water vapor on the INP's surface (*deposition nucleation*). Recent studies e.g. Marcolli (2014); Vali et al. (2015); Wagner et al. (2016) suggested deposition nucleation near water saturation to be more likely the freezing of confined water in pores and cavities (*pore condensation and freezing* (PCF) mechanism). The atmospheric relevance in so- called pre- activations was recently shown by Wagner et al. (2016). The study showed the enhancement of the ice nucleation ability e.g. of clay minerals due to the ice or liquid kept in the pores. In contrast to heterogeneous ice nucleation, homogeneous ice nucleation refers to the ice formation by the freezing of supercooled solution droplets or pure water droplets at temperatures below about 235 K.

Field measurements show a broad spectrum of INP types e.g. minerals, sea salts, soot or biological particles (Cziczo et al., 2013; DeMott et al., 2003). However, this spectrum is not only influenced by the abundance of the different aerosol types, but rather by the efficiency of the INPs in initiating ice nucleation. In laboratory studies the differences in ice nucleation efficiencies of multiple aerosol types and different nucleation modes have been shown (see e.g. Hoose and Möhler, 2012). Naturally-occurring dust was found to be an efficient INP almost over the entire atmospherically relevant temperature and humidity range (Hoose and Möhler, 2012). This finding is supported by in- situ ice residual particle (IRP) measurements which indicate that the ice particles were predominantly formed on naturally-occurring dust (Cziczo et al., 2013; Kamphus et al., 2010; Pratt et al., 2009). However, these studies found that soot in form of EC/ BC was only less or even not present as IRP. In laboratory measurements, the role of soot as an INP is very controversial. BC particles seem to be a good INP (DeMott, 1990), whereas soot from biomass combustion is less or not ice active (DeMott et al., 2009; Petters et al., 2009). Depending on the geographic region and season, signatures from biomass burning particles, sea salt aerosols as well as biological particles were also part of the ice residuals. Anyhow, especially for these particles laboratory measurements are very scarce.

Since heterogeneous ice formation is a very complex process depending on the meteorological situation and the aerosol types and concentration, the ice nucleation ability of aerosol has to be parametrized for use e.g. in models. Commonly, there are two ways

to describe the process of ice nucleation: (1) the Classical Nucleation Theory (CNT) (e.g. Hoose et al., 2010; Chen et al., 2008; Barahona et al., 2010) and (2) deterministic approaches. The first approach assumes ice nucleation to be purely stochastic which is to say that the number of nucleated ice particles increases with time. In case of homogeneous freezing, CNT based parametrizations are in good agreement with experimental results, but in case of heterogeneous ice nucleation observed ice formation can not be reproduced (Barahona et al., 2010; Hoose and Möhler, 2012). Therefore, some efforts were made to develop semi- deterministic or hybrid approaches. These approaches use e.g. contact angle distributions obtained from fits to laboratory measurements (Chen et al., 2008; Niedermeier et al., 2011).

The deterministic approaches result in parametrizations purely based on empirical findings of laboratory and/ or field measurements. Early parametrizations e.g. Meyers et al. (1992) only depend on the thermodynamic conditions. That means, these parametrizations predict heterogeneous ice nucleation independent of the aerosol concentration and the aerosol type. Later on, parametrizations were improved by taking into account the aerosol concentration and/ or the aerosol type in order to prescribe ice nucleation more physically. DeMott et al. (2010) proposed a correlation between the number concentration of INP and the aerosol number concentration of particles larger than 5 μm in diameter. However, in- situ observation of IRP suggest a significant number of INPs with diameters smaller than 5 μm (Cziczo et al., 2013; Kamphus et al., 2010). Furthermore, the field experiments used to develop the parametrization were mostly conducted at water supersaturated conditions referring to cloud droplet freezing only. Other studies e.g. Connolly et al. (2009); Niemand et al. (2012); Atkinson et al. (2013) parametrized the ice nucleation efficiency in terms of the INAS [1] density obtained from laboratory measurements on multiple aerosol particles types. Phillips et al. (2008), on the other hand, developed a parametrization framework based on laboratory and field measurements. The framework was developed for the most important INPs in the atmosphere and is applicable for cloud droplet freezing and deposition nucleation. However, this framework depends on a reference INP spectrum determined from CFDC measurements at only one location and only at water saturation. This reference spectrum might not be representative for other locations or for extraordinary condition like dust plumes or wildfires. Furthermore, Hoose and Möhler (2012) revealed the discrepancy between laboratory measurements and this framework especially below water saturation. Therefore, a parametrization framework based on a statistically relevant data base is needed. This data base has to contain experiments for all atmospherically relevant INPs conducted at well- known conditions. Additionally, the framework should

[1] Ice Nucleation Active Site

preferably cover the atmospherically relevant temperature and humidity range, because extrapolations across the limits of the parametrization might cause unphysical behavior (Curry and Khvorostyanov, 2012). In order to remedy the flaws revealed by Hoose and Möhler (2012) this work will introduce a new parametrization framework respecting the demands mentioned above.

In this work the framework is applied to two atmospherically relevant INP types - dust and soot - which are also treated in common model microphysic schemes. In order to get a representative spectrum of these dusts this work will use desert dust samples to parametrize the ice nucleation efficiency of dust. Since modelling studies showed that even low soot INP concentration influence cirrus formation (Kärcher et al., 2007; Barahona et al., 2010), this work also will try to clarify the contribution of soot aerosol to ice formation. The used experimental data base of heterogeneous ice nucleation on desert dust and soot is provided by several years of experiments at the Aerosol Interaction and Dynamics in the Atmosphere (AIDA) cloud chamber at KIT. First, Chapter 2 will address the theory of aerosol and cloud microphysic. Chapter 3.1 will describe the AIDA cloud chamber and its operation for ice nucleation experiments, the source and nature of the aerosol used for these experiments, as well as the evaluation of the experimental data. In this work, the ice nucleation ability of the aerosol is quantified by the INAS density. The resulting INAS density parametrizations for desert dust and soot will be discussed in Chapter 3.2. As argued above, soot might contribute to ice formation only on a local scale and predominantly at high altitudes. Therefore, to prove the parametrization framework a case study of a synoptically driven cirrus cloud was set up (Ch. 4.3) using the regional model COSMO- ART. The COSMO- ART model will be described in Chapter 4.1. To demonstrate the improvement, model simulations using the newly developed framework and the default scheme will be evaluated. Therefore, the modelling results will be compared to airborne measurements (Ch. 4.2).

2. From Aerosols to Clouds

2.1. Aerosol Physics

Aerosol is defined as a disperse system of solid and/ or liquid particles within air. In atmospheric science aerosol particles are typically classified according to their origin, mixing state/ chemical composition, source or size range in dependence of the scientific question. The size classification sorts the aerosol particles into three modes depending on their diameter (Whitby, 1978): The *Aitken mode* includes particles with diameters between 0.01 μm and 0.1 μm, the *Accumulation mode* particles with diameters of 0.1 μm to 1.0 μm and the *Coarse mode* particles with diameters between 1.0 μm and 10 μm. Sometimes a fourth mode called *Nucleation mode* is used for particles freshly nucleated from the vapor phase. However, this mode is often neglected because these particles grow very fast by condensation resulting into a particle diameter belonging to the *Aitken* or *Accumulation mode*. Each mode of the aerosol spectrum can be represented by an individual lognormal size distribution. The total number size distribution is then given by the sum over all individual size distributions

$$f_N(\ln d_p) = \sum_{l=1}^{k} \frac{n_{p,l}}{\sqrt{2\,\pi}\,\ln \sigma_{g,l}} \exp\left(-\frac{\left(\ln d_p - \ln \overline{d}_{p,l}\right)^2}{2\,\ln^2 \sigma_{g,l}}\right) . \tag{2.1}$$

Where $n_{p,l}$ is the aerosol particle number concentration of mode l, d_p the aerosol particle diameter, $\overline{d}_{p,l}$ the median diameter and $\sigma_{g,l}$ the geometric standard deviation of mode l. The integral of this size distribution over the whole size range gives the total aerosol particle number concentration n_p:

$$n_p = \int_{-\infty}^{\infty} f_N(\ln d_p) \mathrm{d} \ln d_p \, . \tag{2.2}$$

Based on this, surface area and volume concentration size distributions can be derived via the Hatch and Choate conversion (Heintzenberg, 1994; Seinfeld and Pandis, 1998).

$$\begin{aligned} f_{S,l}(\ln d_p) &= \pi d_p^2 f_{N,l}(\ln d_p), \\ s_{p,l} &= \pi\, n_{p,l}\, \exp\left(2\, \ln \overline{d}_{p,l} + 2 \ln^2 \sigma_{g,l}\right) \\ f_{V,l}(\ln d_p) &= \frac{\pi}{6} d_p^3 f_{N,l}(\ln d_p), \\ v_{p,l} &= \frac{\pi}{6}\, n_{p,l}\, \exp\left(3\, \ln \overline{d}_{p,l} + \frac{9}{2} \ln^2 \sigma_{g,l}\right) \end{aligned} \tag{2.3}$$

Thereby, the number concentration $n_{p,l}$, surface area concentration $s_{p,l}$ and volume concentration $v_{p,l}$ can be identified with the zeroth, second and third moment, resp., of the lognormal size distribution. Note that the geometric standard deviation is the same for all moments. In general, the k-th moment of the aerosol size distribution of mode l is defined by

$$\mu_k^l = \int_{-\infty}^{\infty} d_p^k\, f_{N,l}(\ln d_p)\, \mathrm{d} \ln d_p\ . \tag{2.4}$$

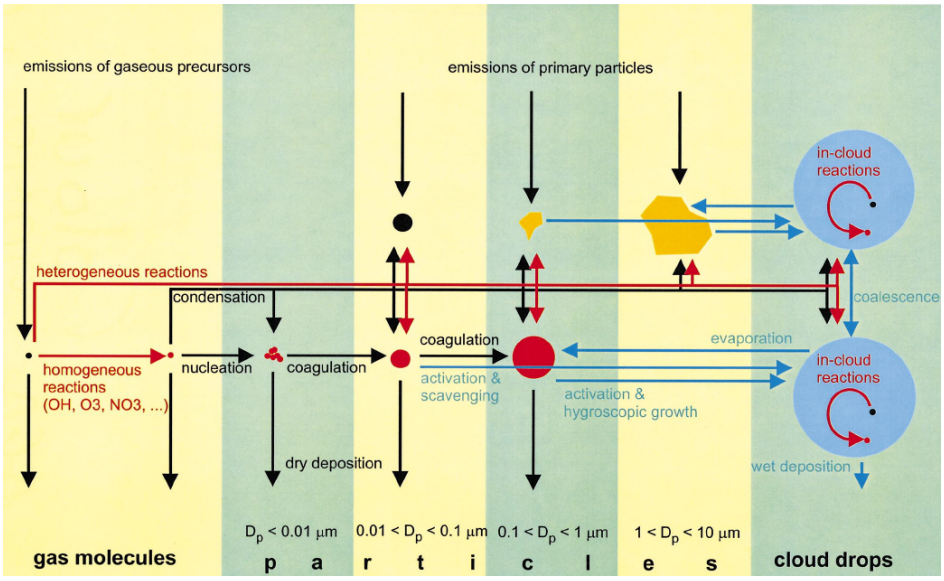

Figure 2.1.: Overview of the size depended formation, evolution and removal of aerosol in the atmosphere. (From Raes et al., 2000)

The classification of the aerosol according to its origin distinguishes between natural and anthropogenic sources. Natural aerosol particles originate from wind dispersion (e.g. minerals, dust, pollen), sea spray, volcanic eruption (ash, sulphate) or wildfire (soot) and their diameters cover mainly the *Coarse mode* size range. Anthropogenic aerosol particles emitted from industry, traffic or slash-and-burn agriculture are smaller than natural aerosol particles.

Aerosol particles can also be classified according to their formation process. Here, primary and secondary particles are distinguished (see Fig. 2.1). Primary particles are directly emitted particles like dust, ash, pollen as well as natural and anthropogenic soot. Secondary particles are particles formed from the gas phase by nucleation (so called gas-to-particle conversion). These particles are mostly mixtures of condensed semivolatile species. Examples for this category are sulphates from volcanic eruptions or VOCs[1] and PAHs[2] from traffic fumes.

The amount of aerosol particles in the atmosphere is determined by their nucleation rate or emission flux, resp., as well as their lifetime. Global emission models show that minerals/ dust is one of the most abundant aerosol in the troposphere (Andreae et al., 2009; Stier et al., 2005). However, the emissions from anthropogenic dust due to e.g. road traffic or land use are less well quantified compared to the natural dust emissions (Boucher et al., 2013). Sea salt particles show higher global emission rates than dust (Andreae et al., 2009; Stier et al., 2005), but are limited to the sea and coastal areas. Black Carbon (BC) particles are less abundant in the troposphere. However, BC aerosol particles are emitted across the whole globe (Stier et al., 2005) and have a broad range of emission sources. The main sources are natural and anthropogenic wildfires. The emission rates of BC from traffic or industry depend strongly on the region and may be underestimated in the commonly used emission inventories (Bond et al., 2013).

During their lifetime in the atmosphere the aerosol particles undergo processes changing their physical or chemical properties. Prominent processes are condensation or coagulation. Because the rate at which vapor condenses on a particle is inversely proportional to the particle diameter, smaller particles will grow faster than larger particles and the size distribution will become narrower (Seinfeld and Pandis, 1998). Coagulation means the collision and coalescence of a particle with another particle. The efficiency of the coagulation depends on the size of the colliding particles and external conditions e.g. turbulence. This process rapidly removes small aerosol particles. Aerosols which are undergone any such process are called *aged aerosol*. The detailed basis of these processes is beyond the scope of this work. These physical and chemical changes of the aerosol population will change its lifetime and its radiative effect.

In the last stage of its lifetime the aerosol particles are removed from the atmosphere by two processes: wet and dry scavenging (Fig. 2.1). The term “dry scavenging” summarizes aerosol losses due to gravitational settling and impaction onto obstacles on the Earths surface. For wet scavenging two mechanisms are distinguished (Lohmann et al., 2016). Nucleation scavenging refers to the removal of aerosol particles due to

[1]Volatile Organic Compounds
[2]Polycyclic Aromatic Hydrocarbons

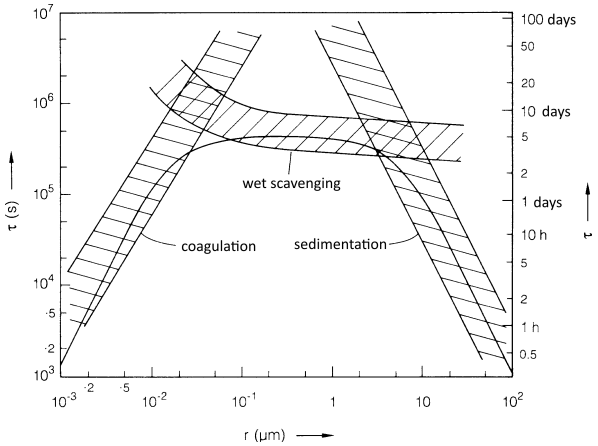

Figure 2.2.: Mean aerosol lifetime of tropospheric aerosol particles as a function of particle radius. (From Roedel and Wagner, 2011).

CCN/ INP activation in clouds. Impaction scavenging, however, means the removal of aerosol particles by coagulation with a cloud particle (e.g. raindrop or ice crystals). The lifetime of aerosol particles is mainly determined by their size as shown in Figure 2.2. *Nucleation mode* and small *Aitken mode* particles are mainly removed by coagulation. For *Accumulation mode* and small *Coarse mode* particles like BC particles wet scavenging dominates, whereas large *Coarse mode* particles (dust, sea salt) are predominantly removed by dry scavenging (Textor et al., 2007). Wet scavenging removes about 30 % of the total aerosol mass averaged over one year (Textor et al., 2007). However, because the number of CCN is much higher than the number of INP, the contribution of INP activation to wet scavenging would be much less than 30 %. Nevertheless, the number concentration of ice particles in a cloud influences its optical and physical properties e.g. rate of precipitation. Therefore, it is even more important to understand how and how much ice particles are formed in dependence of aerosol particle type, size, chemical composition and concentration in the atmosphere.

2.2. Ice Microphysics

In the atmosphere ice can form either from vapor or liquid phase. In Figure 2.3 the main formation mechanisms of ice in the atmosphere are summarized. Basically two formation mechanisms are distinguished: homogeneous and heterogeneous ice nucleation. In principle, homogeneous ice nucleation is the phase transition without a surfactant, solid aerosol particle. However, another two pathways of homogeneous freezing are distinguished. In atmosphere pure water droplets can exist below 273 K down to a specific threshold of about 235 K. At this temperature the supercooled water droplets will freeze immediately. Solution droplets, on the other hand, form already below water

saturation, take up water and freeze at a threshold ice saturation ratio S_i (dashed line) depending on their water activity (Koop et al., 2000). Homogeneous ice nucleation directly from the vapor phase is not taking place in the real atmosphere.

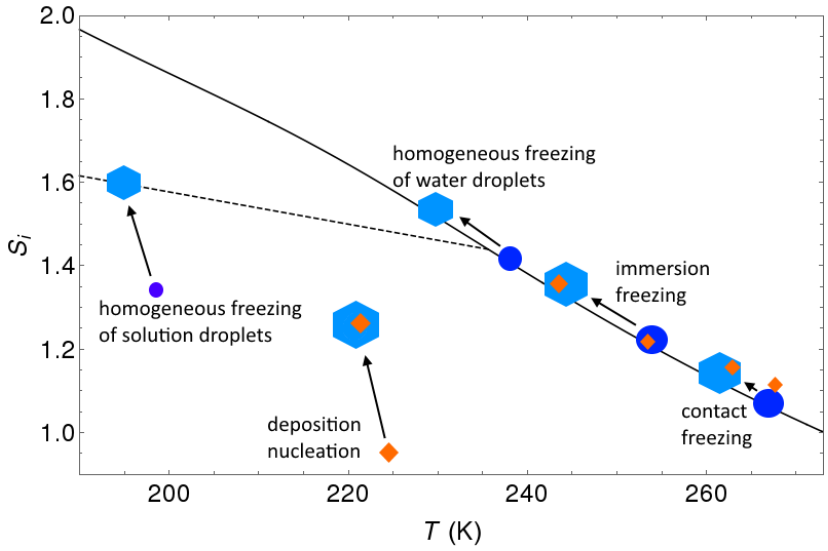

Figure 2.3.: Schematic of the ice nucleation mechanism in dependence of the temperature T and the ice saturation ratio S_i. The black solid line shows the ice saturation ratio at water saturation and the dashed line the threshold S_i for homogeneous nucleation of solution droplets.

Heterogeneous ice nucleation denotes the ice formation initiated by a solid aerosol particle. In Figure 2.3 three pathways of this mechanism are shown. Below water saturation (solid line) *deposition nucleation* takes place when supersaturated water vapor directly deposits on the INP surface. Above water saturation previously formed supercooled water droplets freeze either initiated by an immersed aerosol particle (*immersion freezing*) or by collision with an aerosol particle (*contact freezing*). Sometimes a fourth heterogeneous ice nucleation pathway - *condensation nucleation* - is described (not shown in Fig. 2.3). For this pathway, water condensates on the INP surface but does not form a droplet as in the case of immersion freezing. Then, for a specific temperature the liquid on the aerosol surface freezes. However, the existence of this pathway is controversial (Vali et al., 2015).
Marcolli (2014) suggests that deposition nucleation near water saturation should be viewed as freezing of confined water in pores and cavities. Because of the Kelvin effect water vapor condenses in pores and cavities even below water saturation. By cooling of particles with confined water, the particle will freeze either homogeneously or by immersion freezing and will further grow by water vapor deposition (see Eqn. 2.15). This process was denoted as pore condensation and freezing (PCF) mechanism. However, whether this process takes place depends on the pore structure (geometrical

form or diameter). Assuming cylindrical pores, the pore diameter has to be greater than the critical diameter of the ice embryo which has to form previously in order to initiate the freezing (see next Chapter) of the pore water. Furthermore, the pore diameter directly determines the critical supersaturation wrt ice at which water vapor starts to condense in pores and cavities (Kelvin equation) (Marcolli, 2014). Thereby, the larger the pore diameter is the larger would be the required supersaturation (see Marcolli, 2014, , Fig. 1).

2.2.1. Classical Nucleation Theory

For homogeneous as well as heterogeneous ice nucleation the system consisting of liquid (L) or vapor (V) undergoes a phase transition into a system consisting of ice (I) and the parent phase ($X = V, L$). The energy required for the phase transition is quantified by the difference of the Gibbs free energy after and before the phase transition.

$$\Delta G = G_I - G_X \tag{2.5}$$

In theory the phase transition is assumed to be started by clustering of molecules until the cluster reaches a critical size and transforms immediately into the new phase (I). During the growth, the cluster increases its surface area and volume. Therefore, the change in the Gibbs free energy is given by the superposition of both increases.

$$\Delta G = -\frac{4\,\pi\,r_c^3\,R_v\,T}{3\,\alpha_i}\,\ln\left(\frac{e_{s,X}}{e_{s,I}}\right) + 4\,\pi\,r_c^2\,\sigma \tag{2.6}$$

Where r_c is the cluster radius, R_v the Gas constant of water vapor, T the temperature, e_s the saturation vapor pressure, α_i the specific volume of ice and σ the interfacial tension between both phases. Figure 2.4 illustrates Equation 2.6 (solid line). Before the cluster reached a critical size r_c^*, energy is required to create a larger cluster. At this critical size the energy required for phase transition reaches its maximum ΔG^*. By passing this energy barrier, the growth of the ice embryo becomes more favorable than the evaporation and the ice embryo rapidly grows to an ice particle by vapor deposition. As also shown in the figure, the energy barrier is reduced for heterogeneous ice nucleation assuming that fewer vapor molecules are required to form a cluster of critical size (Lohmann et al., 2016). This reduction is taken into account by multiplying the homogeneous energy barrier by a factor f. Assuming a spherical ice cap on the planar aerosol surface, f describes the level of contact between ice and aerosol in terms of the contact angle θ. In the case of $\theta = 180°$, f becomes 1 and heterogeneous nucleation is no longer favorable (Seinfeld and Pandis, 1998).

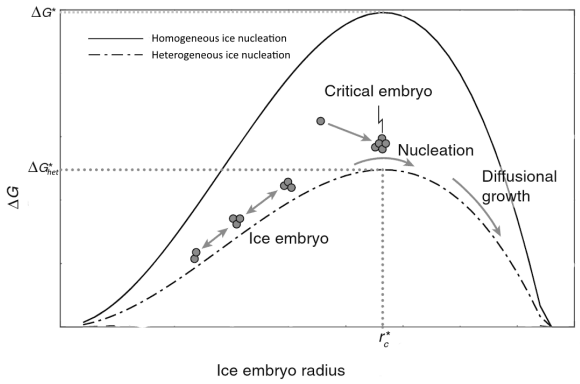

Figure 2.4.: Schematic of the change in Gibbs free energy for homogeneous ice nucleation (solid line) and heterogeneous ice nucleation (dashed line). (Adapted from Lohmann et al., 2016).

The rate at which the cluster overcome this barrier at a given time interval is called nucleation rate j. In addition to the thermodynamic conditions derived above, the nucleation rate also considers the kinetic conditions of the phase transition (e.g. vapor diffusion). In the case of liquid to ice transition, the water molecules have to break the hydrogen bond linkages first before they can be incorporated into the ice lattice. This second energy barrier is denoted by Δg_{act}. Therefore, the final nucleation rate depends on the ice nucleation pathway taking place. For homogeneous ice nucleation the nucleation rate gives

$$j_{hom} = A_{hom} \exp\left(-\frac{\Delta g_{act}}{k_B\,T} - \frac{\Delta G^*}{k_B\,T}\right) \tag{2.7}$$

and for immersion freezing and deposition nucleation, resp.

$$\begin{aligned} j_{frz} &= A_{frz} \exp\left(-\frac{\Delta g_{act}}{k_B\,T} - \frac{\Delta G^*\,f}{k_B\,T}\right) \\ j_{dep} &= A_{dep} \exp\left(-\frac{\Delta G^*\,f}{k_B\,T}\right) \ . \end{aligned} \tag{2.8}$$

A denotes the kinetic prefactor (see e.g. Zobrist et al., 2007; Barahona, 2012). One of the major flaw of this theory is the inevitable extrapolation of the macroscopic description of surface tension, density or chemical potential to a molecular level. Second, many parameters in this theory can not be adequately measured. Therefore, in various studies these values were parametrized. As a results, the values for e.g. Δg_{act} or the surface tension σ used in the literature vary over several orders of magnitude (e.g. Hoose and Möhler, 2012; Ickes et al., 2015). Furthermore, the CNT prescribes that the surface of the aerosol particles is uniform and that the surface of the particles is described

with only one parameter $f(\theta)$. However, in nature aerosol particle are much more complex in morphology and chemical composition than assumed in CNT. Models such as the soccer- ball model (Niedermeier et al., 2011) tried to overcome this limitation by assuming a number of sites at the particle surface whose ice nucleation probability can be described by the CNT. A second approach for describing heterogeneous ice nucleation assumes time- independent ice nucleation at specific sites on the particle surface. This so- called *active surface site* approach is introduced in the following chapter.

2.2.2. Active Surface Site Approach

Whereas the CNT is determined by the random clustering of molecules and therewith the time dependence of the ice nucleation probability, the *singular approach* assumes that the time dependence is only of second order. Furthermore, this approach states that the aerosol surface consists of so- called ice active sites which have their individual nucleation temperature and probability. If the thermodynamic conditions trigger one of these sites, the ice nucleation on the aerosol particle is initiated. Therefore, the heterogeneous ice nucleation can be described by one temperature dependent function. This approach was first developed for immersion freezing. The starting point is a population of droplets each containing an aerosol particle characterized by its specific freezing temperature T_f. The number concentration of frozen droplets n_f at a temperature $T < T_0 = 273.15\,\mathrm{K}$ is then given by the initial number concentration of droplets n_0 minus the number concentration of still unfrozen droplets n_d. Still unfrozen droplets may freeze by further reduction of the temperature $T' = T - \mathrm{d}T$. Therewith, the fraction of droplets frozen in the temperature interval dT is given by (Vali, 1971)

$$\frac{\mathrm{d}n_f(T)}{n_d(T)} = k(T)\, S_{ae}\, \mathrm{d}T \;, \tag{2.9}$$

where S_{ae} is the aerosol surface area immersed in the droplets and $k(T)$ is the number of activated INP per unit aerosol surface and unit temperature interval (e.g. $\mathrm{m}^{-2}\,\mathrm{K}^{-1}$). The integration of $k(T)$ between T_0 and T yields the cumulative number of activated INP per unit aerosol surface, called Ice Nucleating Active surface Site (INAS) density (n_S)

$$-\int_{T_0}^{T} k(\vartheta)\mathrm{d}\vartheta := n_S(T) \;. \tag{2.10}$$

The approach assumes that the most active site at the particle surface initiates freezing of the whole droplet. However, this holds only for a monodispers aerosol population.

In the case of a polydispers population with size categories $l = 1, \ldots, j$, the number concentration of ice particles nucleated from aerosols in size category l is given by

$$\left.\frac{\mathrm{d}n_i(T)}{\mathrm{d}T}\right|_l = n_{ae}\, S_{ae}|_l\; k(T)\;, \tag{2.11}$$

where n_{ae} is the aerosol number concentration available for ice nucleation. Assuming that the change in $n_{i,l}$ is proportional to the change in $n_{ae,l}$, the integration of this equation gives

$$\ln\left(1 - \frac{n_{i,l}}{n_{ae,l}}\right) = -S_{ae,l}\, n_S(T)\;. \tag{2.12}$$

For ice- activated fractions $f_{i,l} := \frac{n_{i,l}}{n_{ae,l}}$ less than 1, this equation simplifies to

$$f_{i,l} \approx S_{ae,l}\, n_S(T)\;. \tag{2.13}$$

Assuming that the INAS density is constant throughout the aerosol particle size range, the INAS density for the total aerosol population is given by

$$n_S(T) \approx \frac{\sum_l n_{i,l}(T)}{\sum_l s_{ae,l}} \tag{2.14}$$

where $s_{ae,l} := n_{ae,l}\, S_{ae,l}$ is the aerosol surface area concentration. Recent studies (Steinke et al., 2015; Hiranuma et al., 2014b) extended this approach to deposition nucleation. There, the INAS density is a function of both temperature and ice saturation ratio S_i.

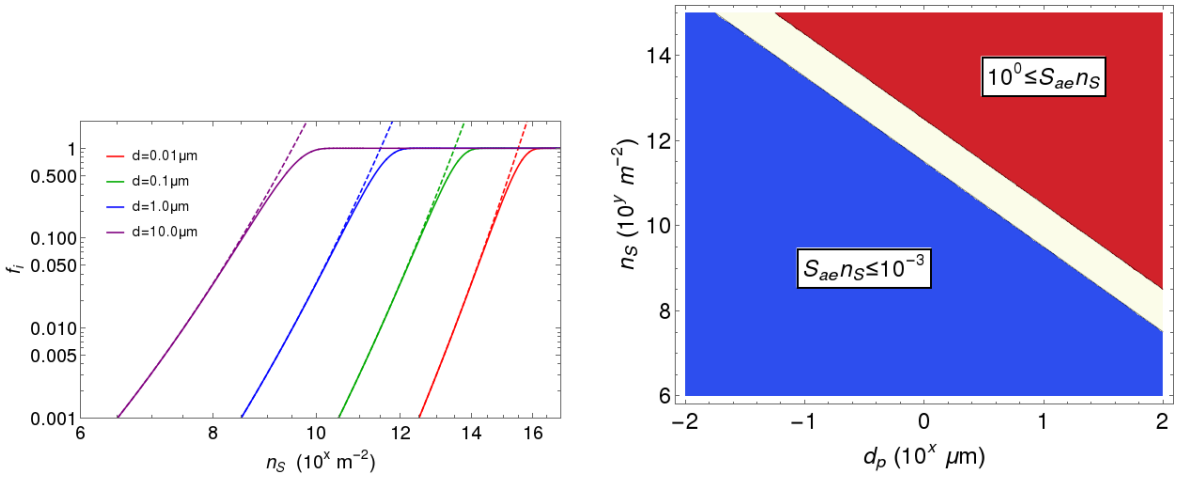

(a) (b)

Figure 2.5.: Regular and approximated ice active fraction as a function of INAS density and aerosol diameter (a) and range of $S_{ae}n_S$ for a proper approximation of Eqn.(2.12) (b).

Figure 2.5(a) shows the ice active fraction as a function of INAS density and aerosol particle diameter calculated via Equation (2.12) (solid lines) and Equation (2.13) (dashed lines). The aerosol surface area was approximated by $\pi\, d_p^2$. Across the range of probable aerosol particle diameters and for all INAS densities, above an ice active fraction of 0.1 the approximated f_i starts to deviate significantly from the non-approximated calculation. Hence, for all combinations of n_S and d_p lying in the blue-shaded area in Figure 2.5(b), the approximation of Equation (2.12) is valid. In Chapter 3.2 this approximation will be cross-checked for typical particle diameters and INAS densities derived from the AIDA laboratory measurements.

2.3. Cloud Ice Microphysics

Once formed, the ice particles undergo a life cycle similar to the aerosol particles. The already discussed formation processes as well as the processes discussed in the following are summarized in Figure 2.6. In pure ice clouds like cirrus ($T < 235\,\mathrm{K}$), the ice particles grow mainly by deposition of water vapor (Lohmann et al., 2016; Lamb and Verlinde, 2011) following

$$\frac{\mathrm{d}m_i}{\mathrm{d}t} = \alpha_m\, 4\,\pi\, C\, s_i\, G \tag{2.15}$$

where α is the accomodation coefficient taking into account the limitation of molecules which can be incorporated into the ice lattice. C is the so-called capacitance and takes into account the non-sphericity of the ice particles. This asphericity mainly determines the flux of water vapor molecules and therewith the formation of different ice crystal habits. s_i is the saturation wrt. ice and G summarizes the thermodynamic (release of latent heat) and kinetic (diffusion of the vapor molecules) limitations of the particle growth.

In mixed phase clouds, the primary ice particles grow by deposition while supercooled droplets evaporate (Bergeron-Wegener-Findeisen process) due to the differences in saturation vapor pressure over liquid and ice surfaces. Larger ice particles might also grow by accretion. Accretion means the collision of ice particles with other cloud particles and the formation of larger ice particles like snowflakes or graupel. In particular, snow flakes are formed by the collision and stick of two ice particles, called aggregation. This process is most efficient for temperatures near the melting temperature, because for this temperatures the quasi-liquid-layer at the ice particle surface is thicker and therewith the sticking efficiency is higher. The collision of ice particles with supercooled cloud droplets (riming) will form graupel. Hail, on the other hand, arises from a freezing-melting cycle of ice particles. However, growth by accretion is determined

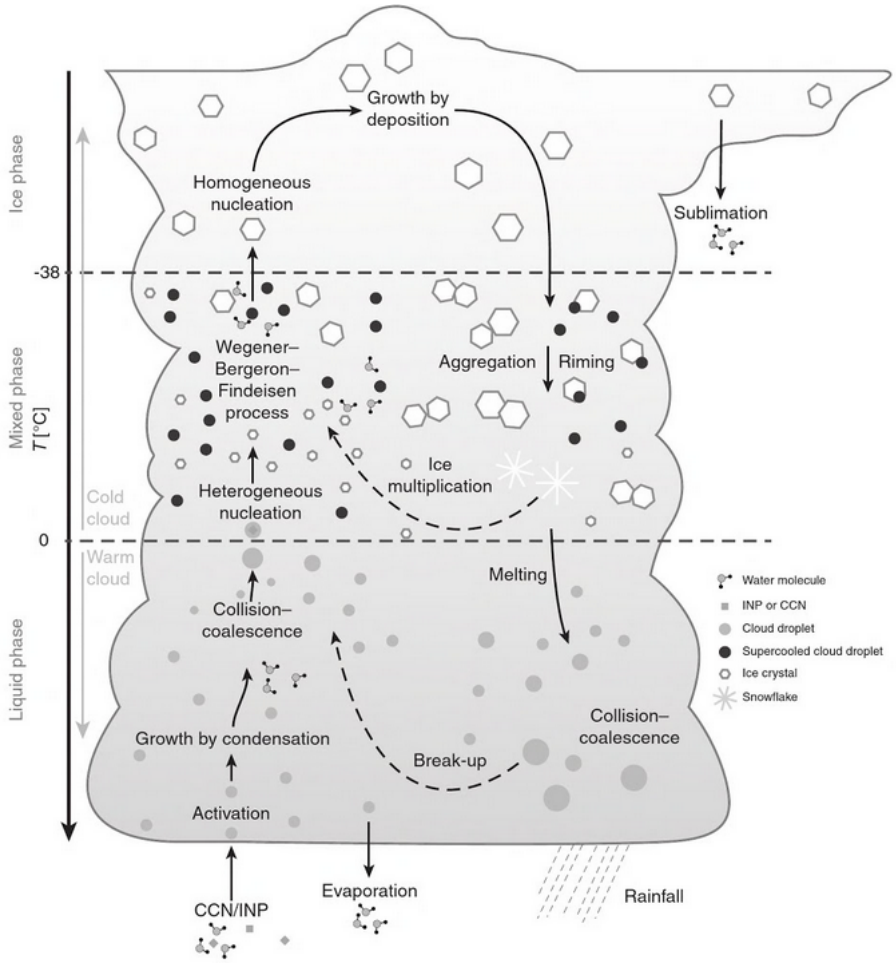

Figure 2.6.: Summary of microphysical processes in clouds. (From Lohmann et al., 2016)

by the different fall velocities of the cloud particles and turbulence (Lohmann et al., 2016)

$$\frac{\mathrm{d}m_i}{\mathrm{d}t} = \overline{E}\, q\, \pi\, R^2\, \left(v_T(R) - v_T(r)\right)\ . \tag{2.16}$$

Where $\overline{E}$ is the mean collection efficiency of the larger particle and q is the liquid or ice water content of the cloud. v_T denotes the fall velocities of the collector with radius R and the collected particle with radius r.

Therewith, accretion removes smaller particles and shifts the size distribution to larger diameters. However, smaller ice particles are also removed by melting or sublimation, whereas larger ice particles are removed either by sedimentation below the cloud (precipitation) or by so- called ice multiplication. Ice multiplication means the splintering of snowflakes or graupel due to collisions. Therewith, more smaller ice particles appear in the size distribution.

Analogous to the aerosols, the different cloud particles span a large size range from a

few μm to a few cm. Commonly, the size distribution of the cloud particles is described by generalized Gamma distributions (Khain et al., 2015)

$$f_N(d_p) = \sum_l A_l(n_{p,l})\, d_{p,l}^{\nu}\, \exp\left(-\lambda(n_{p,l}, m_{p,l})\, d_{p,l}^{\mu}\right) \tag{2.17}$$

where $n_{p,l}$ is the number concentration and $m_{p,l}$ the mass concentration of the cloud particle class l. μ and ν are the so- called shape factors and are assumed to be constant for each cloud particle class (see e.g. Seifert and Beheng, 2001).

3. From Experiments to the Parametrization Framework

[1]According to the ice formation process described above a sheer theoretical description of heterogeneous ice formation is not possible. Laboratory experiments provide the possibility to investigate the ice nucleating behaviour of well- characterized aerosol particles. The AIDA cloud chamber is one of the most established laboratories investigating heterogeneous ice nucleation and can simulate the ascent of an aerosol loaded, moist air parcel up to the level of cloud formation at atmospherically relevant conditions.
The cloud chamber itself as well as the measurement techniques used for the ice nucleation experiments will be explained in Chapter 3.1.
In order to quantify the INAS density as a function of the thermodynamic conditions and for different aerosol types, previously performed AIDA experiments were re- evaluated. This re- evaluation provided a broad and comprehensive data base for the parametrization of the INAS density. The experimental data base for desert dust and soot, and the development of the parametrization framework will be shown in Chapter 3.2.

[1]A slightly modified version of this chapter is currently under review at the Journal of Atmospheric Science:
Romy Ullrich, Corinna Hoose, Ottmar Möhler, Monika Niemand, Robert Wagner, Kristina Höhler, Naruki Hiranuma, Harald Saathoff and Thomas Leisner (2016): A new ice nucleation active site parametrization for desert dust and soot

3.1. AIDA cloud chamber experiments

3.1.1. Experimental Setup

Figure 3.1 shows a schematic of the AIDA cloud chamber with the relevant instrumentation. The core is a 84 m^3 sized aluminium vessel which is located in a thermally insulated housing.

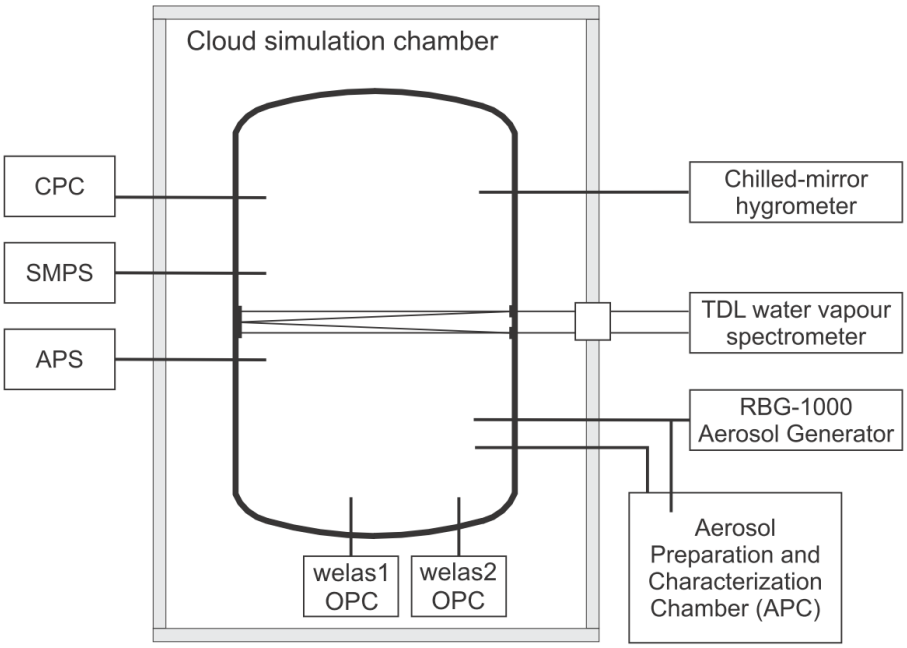

Figure 3.1.: Schematic of the AIDA cloud chamber with the instrumentation relevant for this work, including a tunable diode laser (TDL) absorption spectrometer to measure the water vapor pressure, a chilled- mirror hygrometer to measure total water content, two optical particle counters (OPC) welas1 and welas2 to measure large aerosol particles, cloud droplets and ice crystals, a condensation particle counter (CPC, type 3010) as well as a scanning mobility particle sizer (SMPS) and an aerodynamic particle sizer (APS) to measure aerosol size distributions.

The ascent of an air parcel in the atmosphere can be simulated by evacuating the chamber with one or two vacuum pumps. The related gas expansion causes a distinct temperature decrease because of the adiabatic[2] change of the system. After some time of evacuation, the moist air inside the vessel becomes saturated wrt. to ice and/ or water and forms a cloud. Thereby, the aerosol particles in the chamber air might act as CCN or INP as explained in Chapter 2.2. According to this, the cloud in the chamber is either a pure ice cloud or a supercooled liquid cloud or a mixed- phase cloud.
A mixing fan at the bottom of the vessel ensures the homogeneous spatial distribution

[2]An adiabatic process is a thermodynamic change of a system without exchange of heat.

of temperature, humidity and aerosol. The temperature of the air inside the vessel is measured by four thermocouples vertically aligned across the height of the vessel. The spatial variability in the temperature during an experiments is of about ± 0.3 K (Möhler et al., 2005a). A tunable diode laser (TDL) absorption spectrometer (APicT) measures the water vapor concentration inside the vessel with an accuracy of ± 5 % (Fahey et al., 2014). A second device, a chilled- mirror frost point hygrometer (MBW Calibration Ltd.) sampling via a heated tube measures the total water content. From both instruments, the relative humidity wrt. ice and water within the cloud chamber can be determined.

In preparation of the ice formation experiments, the vessel is first cleaned from aerosols of the preceding experiment by evacuation to a pressure below 1 hPa, flushing with particle free synthetic air, adding pure water vapour to the evacuated vessel forming a partial ice coverage to its inner walls, and filling to atmospheric pressure with particle free synthetic air. After filling and temperature equilibration, the wall ice layers maintain almost ice saturated conditions of the vessel air. The aerosol can be added directly or via the smaller Aerosol Preparation and Characterization (APC) chamber. The latter one is used for e.g. soot aerosol in order to get only a subset of the sampled concentration or to generate larger particles by coagulation. The direct injection is mostly used for the dispersion of powdery particle samples like desert dust. In this case, the sample is first dry- dispersed with a Rotating Brush Generator (RBG) and passes afterwards an aerosol dispersion nozzle and an impactor stage. The nozzle de- agglomerates the particles and the impactor stage removes larger particles from the sample (Möhler et al., 2006).

Before the evacuation starts, the size distribution of the aerosol sample is determined. For this purpose, two instruments are used (Fig.3.1): a Scanning Mobility Particle Sizer (SMPS, TSI) measuring particles with an mobility diameter between 0.014 μm and 0.82 μm and an Aerodynamic Particle Sizer (APS, TSI) measuring particles with an aerodynamic diameter between 0.523 μm and 19.81 μm (Wagner and Möhler, 2013). In order to cover the full relevant size range of the aerosol sample, the data from both instruments needs to be combined. Therefore, the mobility diameter (d_m) and the aerodynamic diameter (d_a) are converted into a volume- equivalent diameter[3] (d_{ve}) (DeCarlo et al., 2004):

$$d_{ve} = \frac{d_m}{\chi} \qquad d_{ve} = \sqrt{\frac{\chi\,\rho_0}{\rho_p}}\,d_a\ . \tag{3.1}$$

χ is the dynamic shapefactor taking into account the discrepancy between the drag force of the non- spherical particle and the drag force of the spherical particle (DeCarlo et al.,

[3]The volume equivalent diameter is the diameter of a sphere having the same volume as the particle under consideration.

2004). $\rho_0 = 1000\,\mathrm{kg\,m^{-3}}$ is the reference particle density and ρ_p the actual particle density. In the next chapter, the values for the particle density and dynamic shapefactor of the aerosol under investigation are discussed. Therewith, a sample-specific lognormal size distribution (see Eqn.(2.1)) is determined. Following Equation (2.3), the according surface area concentration and mass concentration size distributions are calculated.
During the experiment, a Condensation Particle Counter (CPC, type 2010, TSI) measures the total number concentration of aerosol particles larger than 0.01 μm. Additionally, two Optical Particle Counters (OPC, Palas GmbH) welas1 and welas2 measure the optical size and number concentration of aerosol particles as well as cloud particles (droplets, ice crystals). The OPCs welas1 and welas2 cover the full size range of the droplets and ice crystals inside the AIDA cloud chamber. The detection range of welas1 is 0.7 μm to 46 μm and of welas2 5.0 μm to 240 μm (Wagner and Möhler (2013)).
Figure 3.2 shows typical time series for an immersion freezing (a) and a deposition nu-

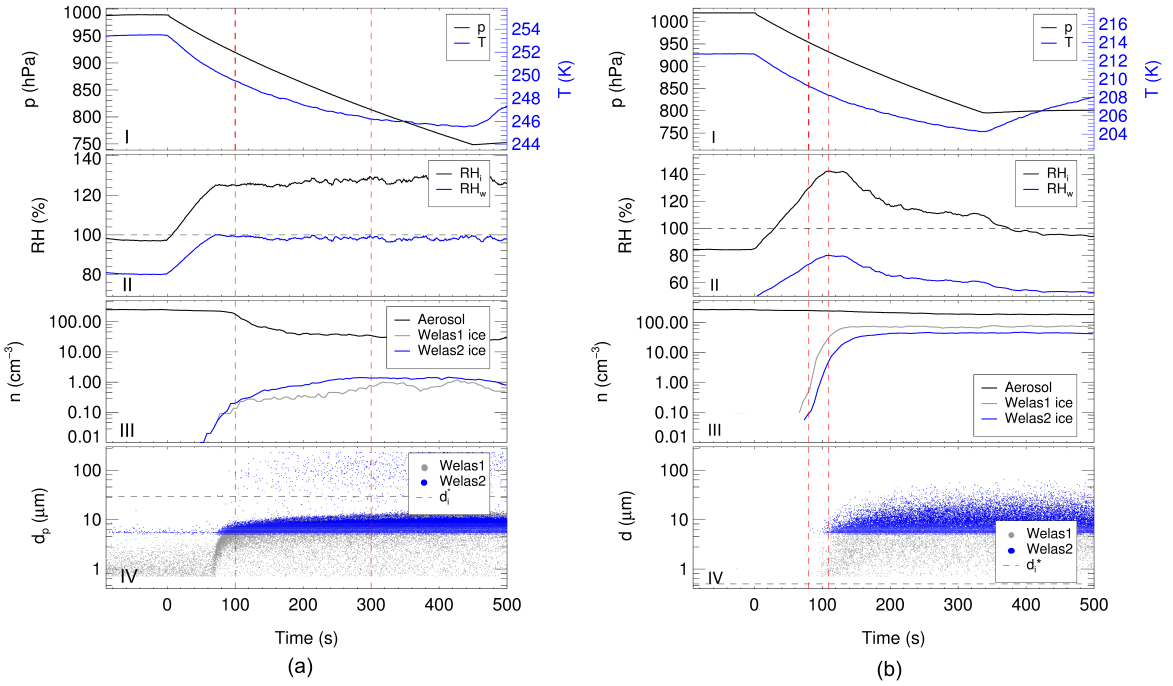

Figure 3.2.: Typical time series of an immersion freezing (left) and a deposition nucleation (right) experiment. Panel I shows the pressure (hPa) and gas temperature (K), panel II the relative humidity wrt. water (blue) and ice (black), panel III shows the total aerosol number concentration from CPC measurements (black) and the ice number concentration from welas1 (gray) and welas2 (blue) measurement. Panel IV shows the optical particle diameter from welas1 (gray) and welas2 (blue). The black line in the lowest panel indicates the diameter threshold to distinguish ice from droplets and aerosol particles. The red dashed, vertical lines indicate the ice nucleation interval.

cleation (b) experiment. After preparations as described above, the chamber evacuation starts at $t = 0\,\mathrm{s}$. Therefore, pressure and temperature decrease (panel I), whereas the

relative humidity increases (panel II). In the case of an immersion freezing experiment (Fig.3.2(a)), water saturation is reached at about 70 s. This results in the start of cloud droplet formation indicated by the densification of the optical diameter point cloud and an increase in optical diameter (panel IV) and also indicated by the decrease of the aerosol concentration (panel III). After another 30 s the freezing of the droplets starts (first red dashed line). This can be seen either in the strong increase in optical diameter (panel IV) and in the increase in ice number concentration (panel III). Ice particles have larger optical diameters compared to cloud droplets and aerosol particles. Therefore, in panel IV a separation of ice particles and droplets/ aerosol can be observed and is indicated by a threshold diameter d_i^* (gray dashed line in panel IV). After about 280 s, the temperature inside the cloud chamber does not further decrease resulting in a leveling off of the ice number concentration. The evacuation stops at $t = 450$ s. The temperature increases again due to the heat flux from the warmer chamber walls. Therefore, chamber pressure increases and humidity decreases again. The ice number concentration decreases because the ice particles sediment and later on evaporate. The fluctuations in ice number concentration from welas1 are due to the small detected concentrations.
In the case of deposition nucleation ice particles form before water saturation is reached (Fig. 3.2(b)). However, at 30 s after start of evacuation saturation wrt. ice is reached. By further cooling, the ice particle formation directly from the vapor phase starts at about 80 s. Because the shown deposition nucleation experiment is an experiment with soot particles, the welas instruments (panel IV) do not detect any aerosol particles. At $t = 110$ s, the relative humidity has its maximum and ice nucleation stops. Analogous to the immersion freezing experiment a threshold diameter d_i^* is set which now discriminates the ice particles from the aerosol. For deposition nucleation experiments this diameter would be generally smaller than for immersion freezing experiments, because the observed ice particles are smaller.

3.1.2. Origin, Preparation and Characterization of the Aerosol Samples

For this work two of the major aerosol types in the atmosphere - desert dust and soot - were used. Table 3.1 summarizes all desert dust samples used in this study and briefly describes the origin of the sample. The samples originate from 7 different locations and were collected from the ground. The sample SD1 was collected as sediment particles 50 km north of Cairo City during a sand storm event on the 18 February 2003 (Megahed, 2007, labeled as CD1 therein). With a backtrajectory analysis, Megahed (2007) showed that the origin of the sample SD1 is the Sahara desert. SD4 was collected at the same

Table 3.1.: Abbreviation and origin of the desert dust samples.

AIDA label	Sample Description
AD1, AD2	Asian Desert Dust; collected from the ground in the easterly parts of the Takla Makan desert in China, east of the Dalimu Basin between Kuerle and Ruoquiang Möhler et al. (2006)
CID1	Canary Island Dust; collected as soil sample from the ground near the town Mala/ Lanzarote (Kanji et al., 2011)
ID1	Israel Desert Dust; collected as sediment particles after a dust storm in Israel/Tel Aviv (Kanji et al., 2011)
	Saharan Desert Dust
SD1, SD4	collected 50 km north of Cairo City/ Egypt as sediment particle after sand storm event (Megahed, 2007; Kanji et al., 2011)
SD2	collected from a hole of 1.5 m depth about 70 km north of Cairo City/Egypt
SD6	collected in Morocco
SD19	collected as soil sample in southern Tunisia near Tozeur 33°58′53.93″N, 8°0′6.72″E (Dr. Emre Toprak, personal communication)

collection location as sample SD1 (Kanji et al., 2011; Niemand et al., 2012). In contrast, SD2 was sampled 1.5 m below ground. All samples were sieved to remove particles larger than 75 μm. Before injecting the aerosol into the AIDA cloud chamber, most of the samples passed a cyclone impactor with a cutoff value between 1 and 5 μm to further remove larger particles.

Elemental analysis of the sieved samples SD1, SD2, SD4, AD1 and AD2 showed strong signals of silicon dioxide indicating that the samples contain quartz (Megahed, 2007; Möhler et al., 2006). For SD2, Linke et al. (2006) (therein labeled as Cairo2) have not been able to detect iron oxides by using X-ray diffractometry (XRD). By ion-chromatographic analysis of aqueous extracts of SD1, SD2, SD4, AD1 and AD2 Megahed (2007) found that the samples contain less than 0.6 wt% of ionic species indicating that the samples may contain a very low amount of anthropogenic pollutants. The samples ID1 and CID1 were collected after Saharan dust storm events (Kanji et al., 2011; Koehler et al., 2010). Koehler et al. (2010) suggested that the CID1 sample might contain beach sand and small amounts of ancient coral. All samples were considered to provide a representative spectrum of natural desert dust.

As described in the previous chapter, the dust samples were dispersed using the RBG. Before addition to the vessel, the sample passes a cyclone impactor stage with 50 % cutoff between 1 μm and 5 μm to remove larger particles. In order to investigate the size effect on ice nucleation, the cyclone impactor stage was not used for some experiments. These experiments show broader size distributions with larger median diameters. As

described in the previous chapter, the mobility diameter and aerodynamic diameter from SMPS and APS, resp., have to be converted into the volume-equivalent diameter. Hence, particle density and dynamic shapefactor are needed. For desert dust a bulk density of $2.6\,\mathrm{g\,cm^{-3}}$ and a dynamic shapefactor of 1.2 were chosen. Those values are in the range for density and dynamic shapefactor given by Kaaden et al. (2009).

Soot is composed of small, almost spherical primary particles formed at the early state of soot production. With time, these primary particles coagulate and build a agglomerate giving the soot aerosol particle its typical fractal-like structure. The size as well as the number of primary particles of an agglomerate determine its fractal dimension and therewith, the optical and aerodynamic behaviour (Wentzel et al., 2003). The soot used for this study is characterized by its Organic Carbon (OC) content using the thermographic carbon analysis according to the German VDI-guideline 2465, part 2 (VDI, 1999). The OC mass content refers to the fraction of carbon which thermally desorbs at 650 °C in a pure helium atmosphere (Schnaiter et al., 2006).
The soot samples used for this study were generated with four devices right before the experiments. A Combustion Aerosol STandard (CAST) burner (Jing Technologies) was used to generated soot in a co-flow diffusion of the fuel gas propane and synthetic air. The ratio of propane to air can be controlled and determines the carbon to oxygen (C/O) ratio of the exhaust. Thereby, the OC mass content of the generated combustion soot increases with increasing C/O ratio (Schnaiter et al., 2006; Crawford et al., 2011). Outside the flame, the freshly generated soot particles passing a dilution and quenching region which directly determines the growth of the primary soot particles to larger agglomerates (Möhler et al., 2005a). Before injecting into the cloud chamber, the soot particles passing through a diffusion dryer in order to reduce the relative humidity of the sample to less than 10 % (Möhler et al., 2005a). This is done to make sure that the particles do not directly act as CCN/ INP when injected into the cold AIDA chamber. A modified version of the CAST burner, the so-called mini CAST burner (mCAST) operates in a similar way, but generated soot with a somewhat higher OC/EC ratio for the same fuel C/O ratio.
The soot of the Graphite Spark Generator (GSG1000, Palas GmbH) is generated by the evaporation of graphite in a spark between two graphite electrodes. The evaporated graphite is transported out off the spark within an argon flow which also prevents oxidation of carbon. By further transport of the sample, the graphite condenses again and forms small carbon particles. These particles start to coagulate and form chains, known as the typical agglomerates. For some experiments nitrogen instead of argon was used as carrier gas.

The fourth sample is a diesel soot generated with a diesel engine test bench (Laborde et al., 2012). This test bench was operated at 2000 revolutions per minute and a torque of 81 Nm. For one experiment no particle filter (pf) was used in order to generate larger soot particles. Before injecting, the exhaust passes a series of denuders reducing the concentration of water, VOCs and nitrogen oxides (Saathoff et al., 2003).
Table 3.2 summarizes all soot samples with their typical OC mass content. As mentioned above, by varying the C/O ratio of the CAST/ mCAST burner the OC mass content of the soot is controlled. Therewith, nearly the total OC mass fraction range can be covered. The CAST soot is often used as a model for Diesel soot, that covers a large

Table 3.2.: Abbreviation and OC mass content of the soot samples.
* from Crawford et al. (2011), † from Henning et al. (2012), ‡ from Blatt (2002).

AIDA label	OC mass content (wt %)
CAST_minOC	5 for C/O ratio=0.28*
CAST_medOC	30 for C/O ratio=0.4*
CAST_maxOC	60 for C/O ratio=0.54*
mCAST_minOC	30 for C/O ratio=0.28*
mCAST_medOC	70 for C/O ratio=0.4*
mCAST_maxOC	90 for C/O ratio=0.54*
GSG-Ar, GSG-N2	12†
Diesel	19‡

range of OC/ EC ratios depending on engines, fuels and after treatment methods. The GSG soot is a sample representing black carbon soot with a low OC mass content. Because of the very different soot samples, bulk densities between 1.8 and 2.4, and shape factors between 1.1 and 1.4 are assumed for the conversion to the volume- equivalent diameter.

3.1.3. Data Processing

The ice nucleation efficiency of desert dust and soot is quantified with the INAS density n_S introduced in Chapter 2.2.2. From Equation (2.14) therein, the total INAS density is given by

$$n_S(T, S_i) = \frac{n_i(T, S_i)}{s_{ae}} \,. \tag{3.2}$$

In order to calculate the INAS density, the ice number concentration n_i and the aerosol surface area concentration s_{ae} have to be determined first. The ice number concentration is calculated from the welas1 and welas2 measurement, resp.
As mentioned in Chapter 3.1, the welas1/ 2 is an optical particle counter based on light scattering.

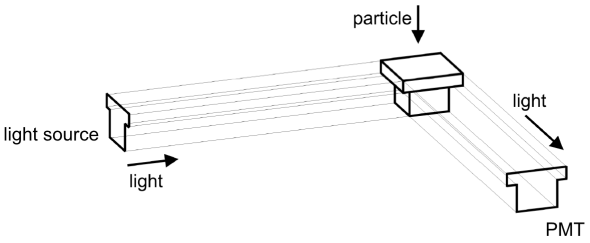

Figure 3.3.: Schematic of the welas detection volume located inside the welas sensor. (From Schiebel, 2014)

A white light source illuminates a detection volume shaped like a 3D T (see Fig.3.3). From above particles enter the detection volume and scatter the incoming light following the Mie- theory. The scattered light is detected at an angle of 90°with a Photomultiplier Tube (PMT). A more detailed description of the functional principle can be found in Benz et al. (2005). In principle, the number of detected PMT pulses correspond to the number of detected particles. The number concentration of detected particles n_p is then given by

$$n_p = \frac{N_p}{\overline{v_p}\,\Delta t\,S_{odv}}\,. \tag{3.3}$$

N_p is the number of particles detected within the time interval Δt. S_{odv} is the cross sectional area of the detection volume. For welas1 this area is $S_{odv} = (280\,\mu\text{m})^2$ and for welas2 $(493\,\mu\text{m})^2$. $\overline{v_p}$ is the mean velocity of the particles through the detection volume and is given by

$$\overline{v_p} = L_{odv}\,\overline{\tau}^{-1}\,. \tag{3.4}$$

L_{odv} is the length of the detection volume. For welas1 L_{odv} is $280\,\mu$m and for welas2 $313\,\mu$m. As long as particles passes the light beam, the PMT measures an current pulse resulting in an time- dependent voltage. $\overline{\tau}$ is the according pulse length averaged for all detected particles. However, Equation (3.3) gives the number of all detected particles (aerosol, cloud droplets and ice). In order to get only the ice number concentration, the ice particles have to be discriminated from the smaller droplets and/or aerosol particles. This is done using the different sizes of ice particles and aerosol particles/ cloud droplets. As shown in Figure 3.2, ice particles have a larger optical diameter than aerosol particles and cloud droplets. Therefore, a diameter threshold as indicated by the dashed line in panel IV of Figure 3.2 is set. Therewith, the ice particle number concentration is calculated for particles larger than this threshold d_i^* following Equation (3.3).

$$n_i = \frac{N_p(d_p \geq d_i^*)}{\overline{v_i}\,\Delta t\,S_{odv}} \tag{3.5}$$

A time interval is set (vertical, red dashed lines in Fig. 3.2) in order to limit the analysis of the ice nucleation to the period of valid and most accurate data. The time at which n_i exceeds its background value of about $0.1\,\mathrm{cm}^{-3}$ is defined as the start of the ice nucleation interval. The end of the interval is that time when no further ice nucleation can be observed. This is detectable by a change in the slope of the ice number concentration. An ongoing increase in n_i is observed for the case of smaller ice particles growing into the detection limit of the welas1/2. This ice nucleation interval Δt is further split into smaller time bins for the analysis. In order to obtain representative statistics, each bin k is required to have a minimum length of 10 s to overcome internal noise and has to include at least 5 ice particle counts. For each bin, the differential ice number concentration $n_{i,k}$ (Eqn. (3.5)) is calculated with a relative error of 0.2 (Wagner and Möhler, 2013). Also the mean temperature T and the mean ice saturation ratio $S_i = \frac{RH_i}{100\,\%}$ are determined time- bin wise. The averaging of the temperature and the ice saturation ratio results in an additional error depending on the length of the time bin k assuming that the ice particles distributed normally within the interval. The total error of the temperature and the ice saturation are then calculated by quadratic error propagation.

For immersion freezing experiments, n_i is calculated from the welas 2 instrument, because of its larger detection volume and therefore higher sensitivity to measure low ice particle concentrations. The welas 1 data is used for deposition nucleation experiments at low temperatures because in this temperature regime ice crystals grow slower, therefore stay smaller in size and can be detected earlier and more sensitively in the smaller size range of welas 1.

The second step for calculating the INAS density is the determination of the aerosol surface area concentration. As described in Chapter 3.1, a number concentration size distribution is determined from SMPS and APS measurement. From this, the surface area concentration size distribution is determined via

$$f_S(\ln d_p) = \pi\, d_p^2\, f_N(\ln d_p) \tag{3.6}$$

assuming spherical particles. Note, both size distributions are fitted each with a lognormal distribution resulting in a different geometric standard deviation. Figure 3.4 shows a typical aerosol size distribution measured at the AIDA cloud chamber. On the left hand side of the figure, the number concentration size distribution $f_N(\ln d_p)$ is shown and on the right hand side the surface area concentration size distribution $f_S(\ln d_p)$. The upper panel shows an experiment with cyclone impactor stage, whereas the lower panel shows an experiment without clearly indicated by the broader distribution and larger median diameter. The black solid line shows the fitted lognormal distribution

function.

The total aerosol number n_{ae} and surface area concentration s_{ae} with the according

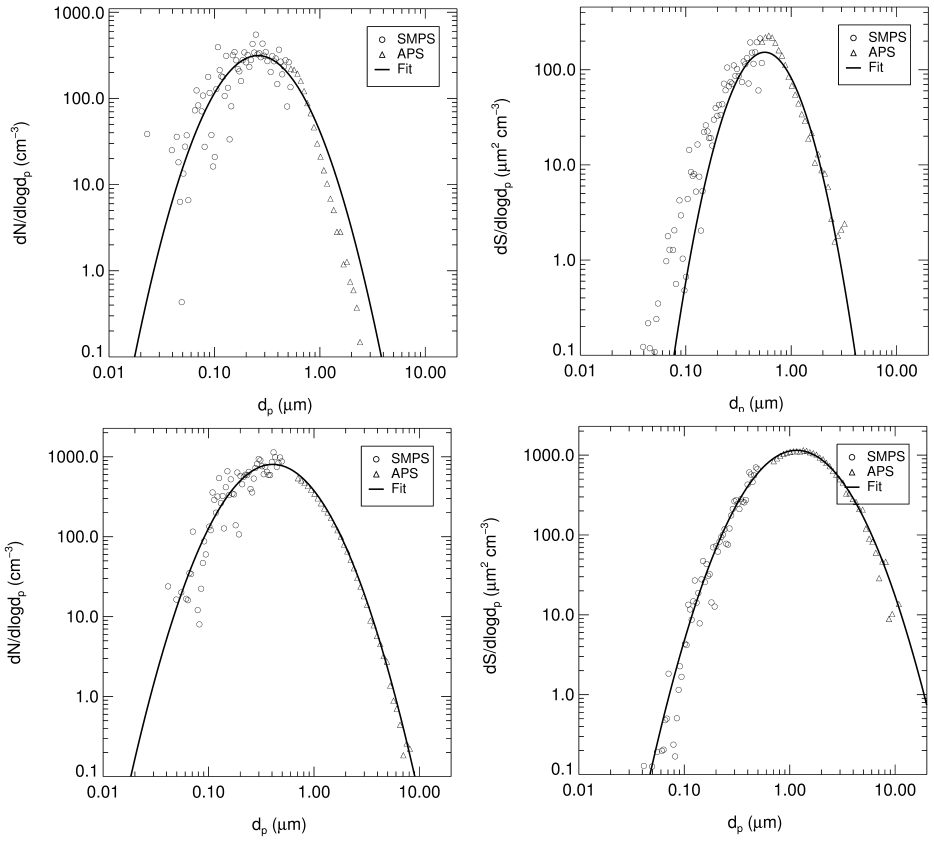

Figure 3.4.: Measured aerosol number concentration size distribution (left) and surface area concentration size distribution (right) with fit for an experiment with cyclone impactor (upper panel) and without (lower panel).

median diameter d_m and the geometric standard deviation σ_g are obtained from the fit. These aerosol size distributions are measured before the evacuation of the AIDA cloud chamber started. However, the aerosol population is reduced during the evacuation. This is corrected by the pressure fraction $p(t_k)/p(t=0)$, where $p(t_k) = p_k$ is the mean pressure in the time bin k and $p(t=0) = p_0$ is the pressure at start of the evacuation. For immersion freezing, only the aerosol activated to droplets will contribute to ice formation. If the CCn activated fraction is less than 50 % the total aerosol surface area concentration is reduced to this fraction (see App C.1), otherwise the correction is negligible and not considered. In each time- bin k a part of the aerosol particles act as INP. The aerosol surface area concentration $s_{ae,k}$ in each time bin k is the fraction of the total aerosol surface area concentration available $s_{ae,0}$ which until this time was activated to ice crystals. This fraction is obtained by integrating the lognormal

probability density function (PDF) from negative infinity to $d_{p,act,k-1}$ (see App C.2) and corrected for the dilution effect

$$s_{ae,k} = s_{ae,0} \frac{p_k}{p_0} \Phi \left(\frac{\ln d_{p,act,k-1} - \ln \overline{d}_s}{\ln \sigma_{g,s}} \right) \tag{3.7}$$

By doing so, it is implied that the largest aerosol particles activate first. This assumption only is a first order correction taking into account that the nucleation probability is proportionate to the squared particle diameter. In Equation (3.7), $\Phi(x)$ is the standard normal distribution function with cutoff value x, $\overline{d}_s$ is the median diameter, and $\sigma_{g,s}$ the geometric standard deviation of the aerosol surface area size distribution function, and $d_{p,act,k-1}$ is the aerosol diameter above which the aerosols were activated in the previous time bin calculated from the ice number concentration.
Following the described algorithm, the INAS density for each time bin k is then calculated by

$$n_{S,k}(T, S_i) = \frac{n_{i,k}(T, S_i)}{s_{ae,k}} \ . \tag{3.8}$$

Note that this approach is different to the cumulative calculation by e.g. Niemand et al. (2012) or Steinke et al. (2011). The error propagation with uncertainties of $\Delta n_{i,k} = 0.2$ (Wagner and Möhler, 2013) and $\Delta s_{ae,k} = 0.34$ yields a relative error for the INAS density of about 40 %.

3.2. Parameterization Framework

Following the algorithm described in Chapter 3.1.3, heterogeneous ice nucleation experiments on desert dust and soot were evaluated. Because in this work no new experiments were performed, but rather were existing experiments re- evaluated. Already published experiments are labeled with the appropriate study in the following overview tables. The results for immersion freezing for desert dust and soot and the developed parametrization lines will be shown in the following chapter. The results and parametrization functions for deposition nucleation for both aerosol types will be shown in Chapter 3.2.2.

3.2.1. Results Immersion Freezing

3.2.1.a. Desert Dust

Table 3.3 lists all AIDA immersion freezing experiments on desert dust performed in the past 11 years with their corresponding initial aerosol number and surface area concentration, the temperature, the ice saturation ratio and the INAS density for the first analyzed time bin. As the evaluation algorithm was improved in this study (see Ch. 3.1.3), also earlier published experiments from Niemand et al. (2012) and Connolly et al. (2009) were reanalyzed. Those experiments are marked in Table 3.3. For the experiments where no ice was detected (Tab. A.1 in Appendix) the temperature at start of droplet formation and at stop of evacuation are listed instead.

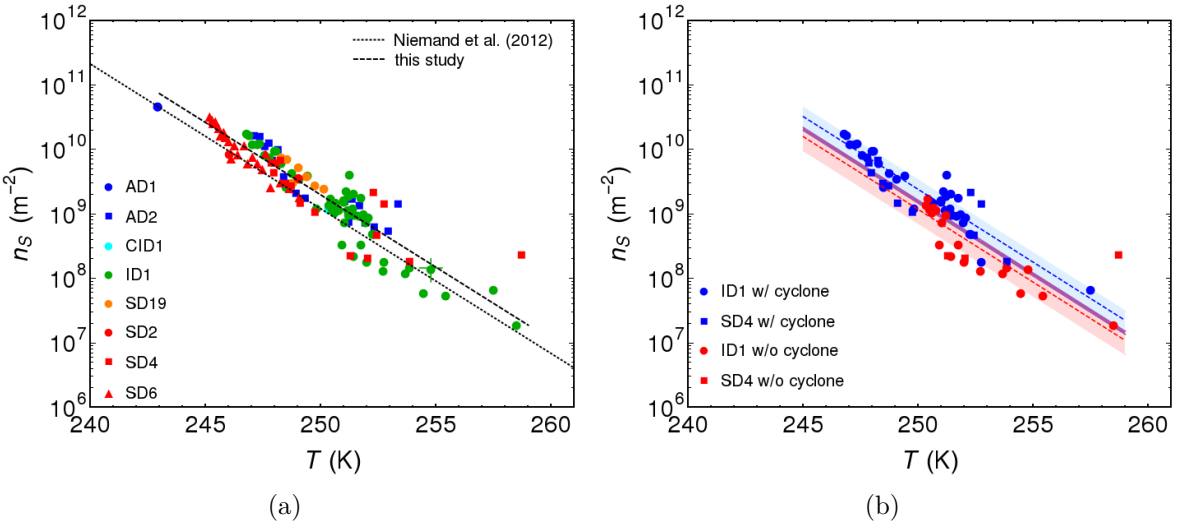

(a) (b)

Figure 3.5.: INAS densities as a function of temperature for (a) all immersion freezing experiments on desert dust listed in Table 3.3 and (b) all experiments with samples ID1 and SD4 showing the influence of the cyclone impactor stage.

Table 3.3.: Conditions for immersion freezing experiments with desert dust. $n_{ae,0}$ is the initial aerosol number concentration measured by the CPC and $s_{ae,0}$ is the initial aerosol surface area concentration. T_{start}, $S_{i,start}$ and $n_{S,start}$ are the temperature, ice saturation ratio and INAS density at start of ice nucleation, resp.
† $s_{ae,0}$ was estimated from $n_{ae,0}$ and for typical $d_{m,n}$ and $\sigma_{g,n}$.
Previously published experiments are labeled with N12 (Niemand et al. (2012)) and C09 (Connolly et al. (2009)).

Campaign	Exp Number	Date	Aerosol	$n_{ae,0}$ (cm^{-3})	$s_{ae,0}$ ($\mu m^2\,cm^{-3}$) 1. mode	2.mode	T_{start} (K)	$S_{i,start}$	$n_{S,start}$ (m^{-2})	published
ACI04	7	30 Sept 2010	SD4	173.88	212.46		253.9	1.19	$1.778 \cdot 10^8$	N12
ACI04	10	30 Sept 2010	SD4	121.79	140.54		249.7	1.27	$1.056 \cdot 10^9$	N12
ACI04	16	01 Oct 2010	AD2	238.25	195.09		253.3	1.19	$1.408 \cdot 10^9$	N12
ACI04	19	04 Oct 2010	AD2	218.24	1.05	186.14	249.3	1.27	$1.719 \cdot 10^9$	N12
ACI04	22	04 Oct 2010	ID1	252.10	163.71		249.8	1.25	$1.256 \cdot 10^9$	N12
ACI04	25	05 Oct 2010	ID1	695.64	385.56	90.54	257.5	1.14	$6.882 \cdot 10^7$	N12
ACI04	28	05 Oct 2010	ID1	655.42	142.29	274.06	252.7	1.20	$1.885 \cdot 10^8$	N12
ACI04	31	06 Oct 2010	ID1	766.53	1438.47		253.8	1.18	$1.509 \cdot 10^8$	N12
ACI04	34	06 Oct 2010	SD4	138.21	142.70	181.34	252.0	1.21	$2.011 \cdot 10^8$	N12
ACI04	37	07 Oct 2010	SD4	114.84	86.19	237.97	258.7	1.15	$2.291 \cdot 10^8$	N12
ACI04	40	07 Oct 2010	ID1	739.47	1201.91		258.5	1.14	$1.926 \cdot 10^7$	N12
ACI04	43	08 Oct 2010	ID1	526.57	868.77		254.8	1.18	$1.446 \cdot 10^8$	N12
ACI04	46	08 Oct 2010	ID1	604.47	805.49		255.4	1.17	$5.646 \cdot 10^7$	-
ICIS07	17	24 Sept 2007	ID1	253.81	96.32		252.3	1.15	$5.083 \cdot 10^8$	N12
ICIS07	20	25 Sept 2007	SD4	396.77	92.80		252.7	1.15	$1.403 \cdot 10^9$	N12
ICIS07	23	26 Sept 2007	CID1	381.81	58.68		250.3	1.18	$1.228 \cdot 10^9$	N12
IN04	6	17 Sept 2003	SD2	171.67	67.88		246.0	1.13	$8.747 \cdot 10^9$	C09
IN04	18	24 Sept 2003	AD1	181.33	72.49†		242.9	1.32	$5.955 \cdot 10^9$	C09
IN04	30	29 Sept 2003	SD2	250.0	127.93		249.0	1.11	$3.736 \cdot 10^9$	C09
IN19	23	16 July 2012	SD19	180.77	99.27		250.1	1.19	$2.530 \cdot 10^9$	-
FIN02	3	14 Mar 2015	SD6	735.45	88.47	25.71	249.1	1.23	$1.880 \cdot 10^9$	-

Figure 3.5(a) shows the temperature dependent INAS densities for desert dust aerosol from all experiments listed in Table 3.3. Note that because of the time bin-wise evaluation, one or more data points per experiment can be obtained. A typical error bar for the temperature and the INAS density is shown for only one data point.
Freezing of supercooled droplets was detected between 243 K and 259 K. The calculated INAS densities range from about $4.0 \times 10^{10}\,\mathrm{m}^{-2}$ to $1.0 \cdot 10^{7}\,\mathrm{m}^{-2}$, increasing for decreasing temperature. Following Niemand et al. (2012), the INAS density values derived from the measurements for immersion freezing on desert dust can be approximated by an exponential function (see Fig.3.5(a), dashed line).

$$n_S(T, \text{desert dust}) = \exp\left(150.577 - 0.517\,T\right)\,\mathrm{m}^{-2}, \qquad T \in [243, 259]\,\mathrm{K} \tag{3.9}$$

This function yields n_S values ranging from $7.4 \cdot 10^{10}\,\mathrm{m}^{-2}$ to $1.9 \cdot 10^{7}\,\mathrm{m}^{-2}$ in the temperature range from 243 K to 259 K. Comparing the different desert dust samples concerning their ice nucleation ability no large discrepancies were observed, as also reported by Niemand et al. (2012). Note that this also holds for the samples that have been transported through the atmosphere, indicating that the INAS density fit line may be representative for immersion freezing of both freshly emitted and transported dust. The comparison of the new parametrization (Eqn. (3.9)) with the one from Niemand et al. (2012) (Fig.3.5(a)) yields a mean shift by a factor of 1.64 to higher n_S values. This could be explained by the correction of the aerosol surface area available for immersion freezing in a certain time bin for the amount of aerosols that already induced ice formation in previous time bins. In the current analysis, this procedure reduces the aerosol surface area and therefore, increases the resulting INAS density compared to not corrected data.
For the experiments ACI04_31, 34, 37, 40, 43 and 46, no cyclone impactor stage was used during the injection into the AIDA cloud chamber. These experiments have a larger median diameter (factor ~ 2) and a larger aerosol surface area concentration (factor ~ 2.5) than the experiments with cyclone impactor sage (Fig. 3.4). Figure 3.5(b) shows the INAS densities for experiments with ID1 and SD4 with and without cyclone impactor stage. Fitting both data sets with the same slope as the common parametrization line (Eqn. (3.9)) yields to somewhat lower INAS density values for the data sets without a cyclone impactor stage. The shift in the offset compared to the offset in Equation (3.9) is of about 0.3 % for the experiments without cyclone impactor stage and 0.2 % for the experiments with cyclone impactor stage. However, the difference between with and without cyclone impactor stage is within the uncertainty range as indicated with the shaded area.

3.2.1.b. Soot

In Table 3.4 all immersion freezing experiments on soot aerosol performed so far in the AIDA cloud chamber are summarized. For each experiment the initial aerosol number concentration and surface area concentration, the temperature at start of droplet formation, and the INAS density and appropriate temperature are listed.
Heterogeneous ice formation was only observed in two experiments with CAST_minOC soot (ACI03_5 and IN09_6) and an experiment with GSG soot (IN09_3) (Tab. 3.4), but overall only 5 or less ice particles were counted. During five experiments with GSG soot (see Tab. 3.4) supercooled droplets formed at about 240 K, but only homogeneous freezing was observed upon further cooling at about 238 K. For the experiment HALO06_2, supercooled droplets existed in the temperature range from 251 K to 248 K, but no freezing was observed.
Based on the welas detection limit, only an upper limit for the INAS density value was determined from these experiments in contrast to the analysis of the previously shown desert dust experiments. These upper limits were calculated by taking a total number of five ice crystals as the welas ice number detection limit in the whole time period with the supercooled droplet cloud present in the AIDA chamber. Accordingly, Figure 3.6 depicts one INAS density upper limit value for each experiment together with literature data. Compared to the data points calculated from DeMott (1990) the n_S values from the AIDA measurements are up to three orders of magnitude lower. However, there is a very good agreement with the very recent study of Schill et al. (2016) using diesel exhaust particles. The AIDA measurements suggest that soot with a low OC content is a poor immersion freezing INP. The deviation between the laboratory results may indicate highly variable ice nucleation activity of different soot types.
In order to estimate a parametrization line for the INAS density of soot, the parametrization given by Murray et al. (2012) (based on data from (DeMott, 1990) and (Diehl and Mitra, 1998)) was scaled to the AIDA data points in Figure 3.6, as done by Schill et al. (2016).

$$\begin{aligned} &n_S(T, \text{soot}) \\ &\quad = 7.463 \exp\left(-0.0101\,(T - 273.15)^2 - 0.8525\,(T - 273.15) + 0.7667\right)\ \mathrm{m}^{-2}, \\ &\quad T \in [239, 255]\,\mathrm{K} \end{aligned} \tag{3.10}$$

This function yields n_S values ranging from $5.4{\cdot}10^8\,\mathrm{m}^{-2}$ to $3.0{\cdot}10^6\,\mathrm{m}^{-2}$ in the temperature range 239 K to 255 K. Note that this function represents the upper limit INAS density values derived from AIDA immersion freezing experiments with soot. Therefore, the

Table 3.4.: Conditions for immersion freezing experiments with soot. $n_{ae,0}$ is the initial aerosol number concentration measured by the CPC and $s_{ae,0}$ is the initial aerosol surface area concentration. $n_{S,max}$ is the upper limiting INAS density, and T_{max} is the corresponding temperature. $T_{droplet}$ is the temperature at start of droplet formation. If labeled with * no upper limiting n_S was determined.

Campaign	Exp Number	Date	Aerosol	$n_{ae,0}$ (cm^{-3})	$s_{ae,0}$ ($\mu\mathrm{m}^2\,\mathrm{cm}^{-3}$)	$T_{droplet}$ (K)	T_{max}	$n_{S,max}$ (m^{-2})
ACI02	34	27 Oct 2008	GSG-Ar	9939.17	745.57	240.5	239.3	$1.302 \cdot 10^8$
ACI02	37	28 Oct 2008	GSG-Ar	11257.27	863.56	241.0	239.2	$1.479 \cdot 10^8$
ACI02	41	29 Oct 2008	GSG-N2	10213.53	1749.29	240.5	239.3	$4.737 \cdot 10^7$
ACI03	5	06 Oct 2009	CAST minOC	29722.40	1422.15	247.5	245.3	$4.408 \cdot 10^8$
HALO02	2*	09 Dec 2008	GSG-Ar	1778.48	n/a	241.0	-	-
HALO06	2*	24 Jan 2011	GSG-Ar	50.00	n/a	251.0	-	-
IN09	3	21 Mar 2006	GSG-Ar	125.72	11.68	241.5	239.4	$2.170 \cdot 10^9$
IN09	6	23 Mar 2006	CAST minOC	165.50	84.38	239.9	238.8	$5.704 \cdot 10^8$
YETI04	35	26 Jan 2015	GSG-Ar	3733.90	1007.20	242.5	239.3	$4.485 \cdot 10^7$

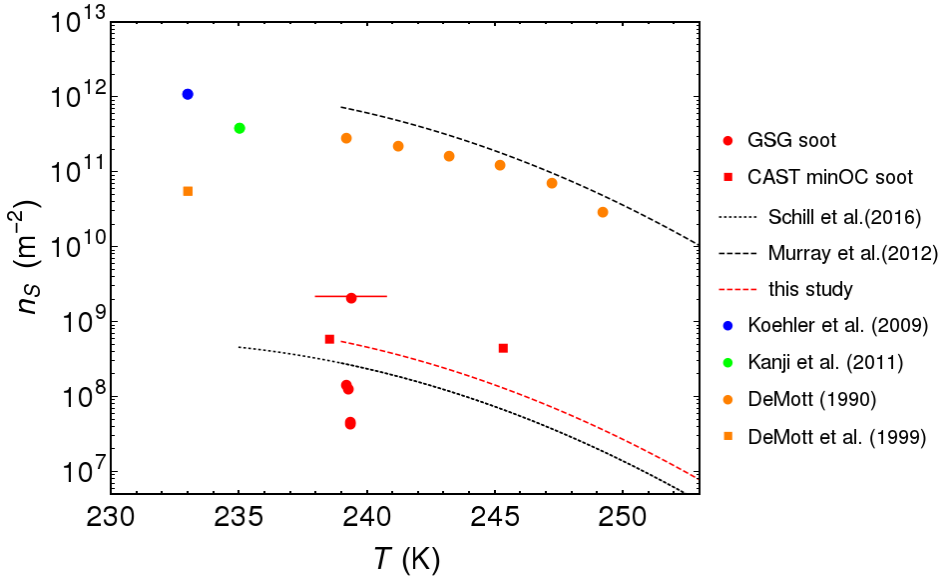

Figure 3.6.: Upper limit INAS densities as a function of temperature for all immersion freezing experiments on soot listed in Table 3.4 (red circles). Additionally, data points from Koehler et al. (2009) for thermal oxidized soot (blue circle), from Kanji et al. (2011) for GSG soot (green circle), from DeMott (1990) for acetylene burner soot (d_m =0.12 μm) (orange circle) and from DeMott et al. (1999) for Degussa lamp black carbon (orange squares) are shown. The dashed black line represents the parametrization line from Murray et al. (2012), the dotted black line the parametrization line from Schill et al. (2016), and the red dashed line the new scaled parametrization. The root mean square error for $\ln n_S$ is 1.94.

parametrization might have to be adapted to even lower INAS density values when more experiments with soot in immersion freezing mode are available for analysis.

3.2.1.c. Comparison to Other Immersion Freezing Parametrizations

Figure 3.7 shows a summary of the parametrization for desert dust and soot together with INAS density parametrizations from the literature. The lines for the dust components Illite NX (Hiranuma et al., 2015), K- feldspar (Atkinson et al., 2013) and kaolinite (Murray et al., 2011) were scaled to their mean mass fraction in natural desert dusts following Atkinson et al. (2013) (Suppl.Table 1 therein). The line for milled hematite (Hiranuma et al., 2014a) was not scaled, because the mass fraction within natural desert dusts is unknown. Furthermore, note that Illite NX, kaolinite and K-feldspar are not pure samples, but include some minor fraction of other minerals. Nevertheless, the scaled parametrization for Illite NX does agree very well with the parametrization for natural desert dust. Therefore, Illite NX seems to be a good proxy for ice nucleation of desert dust. Kaolinite, feldspar and hematite are only minor components of desert dusts and show a much steeper decrease in INAS density with increasing temperature.

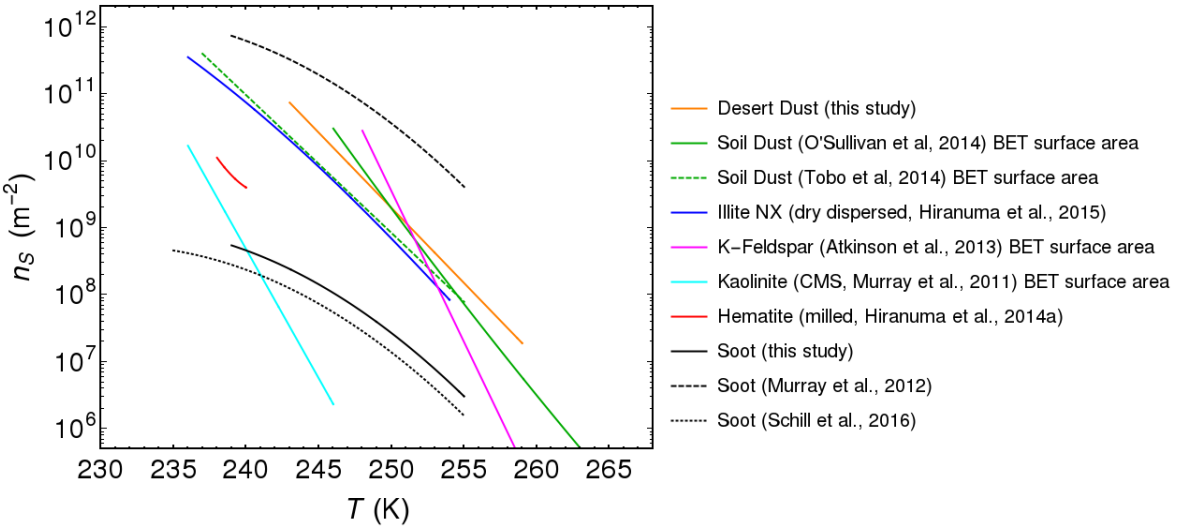

Figure 3.7.: Comparison of INAS density parametrization for immersion freezing experiments with natural dust, soot and dust components. The parametrization of Atkinson et al. (2013), Murray et al. (2011), O'Sullivan et al. (2014) and Tobo et al. (2014) used the BET surface area whereas the other study used the geometric surface area to calculate n_S. The parametrization lines for Illite NX, K-feldspar and kaolinite were scaled according to their mean mass fraction in natural dusts (Atkinson et al., 2013).

The transformation of BET aerosol surface areas to geometric surface areas would shift the INAS densities for soil dust, K- feldspar and kaolinite slightly to higher values.
Compared to desert dust, soil dust shows a higher ice nucleation activity especially for warmer temperatures (Steinke et al., 2016; Hill et al., 2016). Recent studies showed that soil dust samples featured a significant fraction of organic matter and biological active particles, which might influence the ice nucleation at warmer temperatures (Tobo et al., 2014; Hill et al., 2016).
The high uncertainty of the immersion freezing efficiency of soot aerosol is represented in the deviation of the parametrization line of Murray et al. (2012) and the rescaled Murray- parametrization line for the upper limiting n_S values from AIDA measurements. Both lines deviate by three orders of magnitude. However, there is a very good agreement between the derived soot parametrization and the fit line of Schill et al. (2016).

3.2.2. Results Deposition Nucleation

3.2.2.a. Desert Dust

Figure 3.8(a) shows the INAS densities (filled symbols) in the ice saturation ratio-temperature plane for all deposition nucleation experiments on desert dust listed in Table 3.5. The open symbols show results from two previous AIDA deposition nucleation

Table 3.5.: Conditions for deposition nucleation experiments with desert dust. $n_{ae,0}$ is the initial aerosol number concentration measured by the CPC and $s_{ae,0}$ is the initial aerosol surface area concentration. T_{start}, $S_{i,start}$ and $n_{S,start}$ are the temperature, ice saturation ratio and INAS density at start of ice nucleation, resp.

Campaign	Exp Number	Date	Aerosol	$n_{ae,0}$ (cm^{-3})	$s_{ae,0}$ ($\mu m^2\,cm^{-3}$) 1. mode	2.mode	T_{start} (K)	$S_{i,start}$	$n_{S,start}$ (m^{-2})
ACI03	14	12 Oct 2009	AD2	720.00	179.90		230.6	1.37	$1.682 \cdot 10^{10}$
IN04	22	25 Sept 2003	AD1	118.65	67.64		232.2	1.36	$3.457 \cdot 10^{10}$
IN04	26	26 Sept 2003	AD1	100.45	44.41		219.8	1.26	$3.973 \cdot 10^{10}$
IN04	35	30 Sept 2003	SD2	130.60	116.65		235.3	1.40	$8.009 \cdot 10^{10}$
IN04	40	01 Oct 2003	SD2	91.03	56.08		221.2	1.29	$3.535 \cdot 10^{10}$
IN05	5	20 Oct 2004	SD2	104.00	23.93		222.6	1.23	$1.051 \cdot 10^{11}$
IN05	9	21 Oct 2004	SD2	45.00	9.68		207.6	1.13	$1.051 \cdot 10^{11}$
IN15	16	28 Mar 2011	SD2	690.31	429.67		220.3	1.13	$2.045 \cdot 10^{10}$
IN15	24	30 Mar 2011	SD2	552.22	325.43		239.7	1.22	$1.716 \cdot 10^{10}$
IN19	26	17 July 2012	SD19	142.80	89.81		243.6	1.23	$2.567 \cdot 10^{10}$
YETI04	56	03 Feb 2015	ID1	599.96	157.06	5.55	226.3	1.14	$5.171 \cdot 10^{9}$
YETI04	57	04 Feb 2015	CID1	148.52	38.10		227.2	1.09	$7.943 \cdot 10^{11}$

studies (Möhler et al., 2006; Field et al., 2006). These data points were calculated by

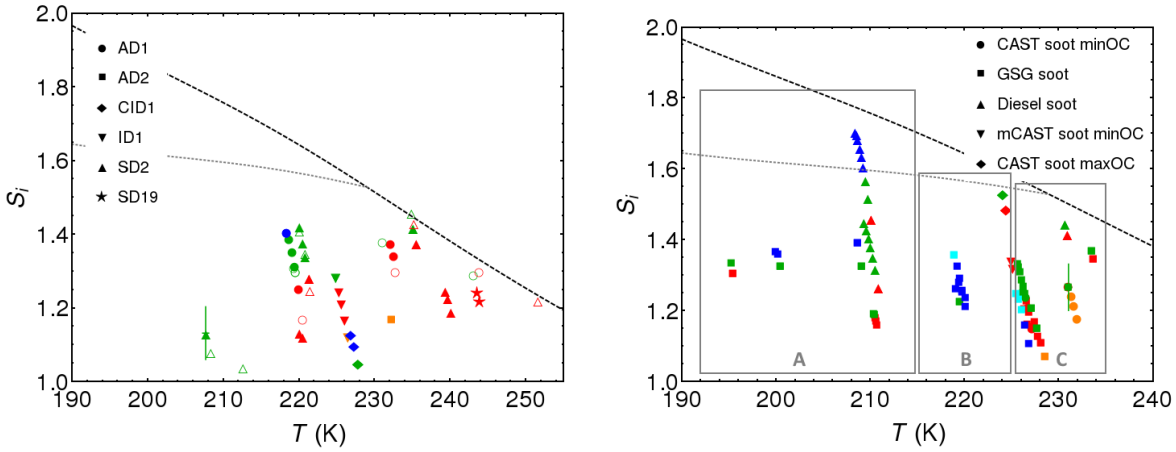

(a) (b)

Figure 3.8.: INAS densities as a function of temperature and ice saturation ratio for all deposition nucleation experiments on (a) desert dust listed in Tab. 3.5 and (b) soot listed in Tab. 3.6. The black dashed line indicates the ice saturation ratio S_i at water saturation and the gray dotted line the homogeneous freezing threshold for solution droplets ($\Delta a_w = 0.34$, Koop et al., 2000). The different symbols indicate the different samples and the different colors the order of magnitude of the INAS density as follows orange: $5 \cdot 10^8 \leq n_S < 5 \cdot 10^9$ m^{-2}, red: $5 \cdot 10^9 \leq n_S < 5 \cdot 10^{10}$ m^{-2}, green: $5 \cdot 10^{10} \leq n_S < 5 \cdot 10^{11}$ m^{-2} and blue: $5 \cdot 10^{11} \leq n_S < 5 \cdot 10^{12}$ m^{-2}. The open symbols in (a) are AIDA deposition nucleation experiments with SD2 and AD1 evaluated by Möhler et al. (2006) and Field et al. (2006), resp.

dividing the published activated fraction by the aerosol surface area calculated from the median diameter and the aerosol number concentration also given in the papers by Möhler et al. (2006) and Field et al. (2006). The range of the INAS density is indicated by the different colors and typical error bars for temperature and ice saturation ratio are indicated for one data point.

Deposition nucleation experiments with desert dust were so far only conducted at temperatures above 206 K. These experiments yield INAS densities from $5 \cdot 10^8$ m^{-2} to $5 \cdot 10^{12}$ m^{-2}. The samples AD1, AD2 and SD2 show a similar ice nucleation behavior over the whole temperature range. The samples CID1 and SD19 have a somewhat higher deposition nucleation activity at lower ice saturation ratios. The INAS density data from ID1 is located between the two other groups.

3.2.2.b. Soot

Figure 3.8(b) shows the INAS densities in the ice saturation ratio- temperature plane for all deposition nucleation experiments with soot listed in Table 3.6. Crawford et al. (2011) already published the onset ice active fractions for the experiments from the

Table 3.6.: Conditions for deposition nucleation experiments with soot. $n_{ae,0}$ is the initial aerosol number concentration measured by the CPC and $s_{ae,0}$ is the initial aerosol surface area concentration. T_{start}, $S_{i,start}$ and $n_{S,start}$ are the temperature, ice saturation ratio and INAS density at start of ice nucleation, resp. If ice nucleation starting conditions are not given no heterogeneous ice nucleation was observed (*).
Previously published experiments are labeled with Cr11 (Crawford et al. (2011)).

Campaign	Exp Number	Date	Aerosol	$n_{ae,0}$ (cm^{-3})	$s_{ae,0}$ ($\mu m^2\,cm^{-3}$) 1. mode	2.mode	T_{start} (K)	$S_{i,start}$	$n_{S,start}$ (m^{-2})	published
ACI02	45	30 Oct 2008	GSG-Ar	10000.00	265.24		227.4	1.17	$6.058 \cdot 10^{10}$	-
ACI02	49	31 Oct 2008	GSG-N2	9984.49	530.64		228.0	1.11	$4.447 \cdot 10^{10}$	-
ACI03	22	14 Oct 2009	CAST minOC	26929.10	1399.29		231.8	1.19	$1.197 \cdot 10^{9}$	-
HALO02	6	10 Dec 2008	GSG-Ar	88.23	1.70		226.7	1.12	$9.367 \cdot 10^{11}$	-
HALO04	18	08 Dec 2009	GSG-Ar	2433.40	131.94		210.6	1.16	$1.278 \cdot 10^{10}$	-
HALO04	26	10 Dec 2009	GSG-Ar	2409.91	96.44		195.3	1.32	$6.213 \cdot 10^{10}$	-
HALO06	27	02 Feb 2011	GSG-Ar	268.69	11.51		208.8	1.36	$9.317 \cdot 10^{11}$	-
HALO06	29	02 Feb 2011	GSG-Ar	970.28	31.81		200.2	1.35	$5.007 \cdot 10^{11}$	-
ICIS07	12	20 Sept 2007	GSG-Ar	442.19	34.37		231.0	1.27	$1.033 \cdot 10^{11}$	-
ICIS07	15	21 Sept 2007	GSG-Ar	425.86	74.64	59.52	233.6	1.36	$1.144 \cdot 10^{11}$	-
IN09	8	24 Mar 2006	CAST minOC	209.45	70.02		227.0	1.16	$1.147 \cdot 10^{10}$	Cr11
IN09	21	30 Mar 2006	CAST maxOC	290.00	4.18	37.32	224.3	1.50	$3.327 \cdot 10^{10}$	Cr11
IN09	25	31 Mar 2006	GSG-Ar	433.24	206.37		226.5	1.17	$5.570 \cdot 10^{9}$	Cr11
IN11	15	20 Nov 2007	GSG-N2	99.31	33.75		227.1	1.16	$2.973 \cdot 10^{10}$	Cr11
IN11	20	22 Nov 2007	mCAST minOC	1111.52	166.96		225.0	1.33	$3.050 \cdot 10^{10}$	Cr11
IN11	26	26 Nov 2007	mCAST maxOC	1173.01	129.68		-	-	-*	Cr11
RICE01	22	27 Nov 2012	GSG-Ar	246.55	16.29		220.1	1.24	$7.311 \cdot 10^{11}$	-
RICE02	8	29 Apr 2013	GSG-Ar	51.75	4.33		219.6	1.26	$9.642 \cdot 10^{11}$	-
RICE02	9	30 Apr 2013	GSG-Ar	94.44	5.61		219.2	1.25	$1.801 \cdot 10^{12}$	-
RICE02	15	02 May 2013	GSG-Ar	48.25	0.89		220.0	1.23	$7.968 \cdot 10^{11}$	-
SOOT11	17	02 Dec 2010	Diesel	4852.92	97.10		230.8	1.43	$7.776 \cdot 10^{10}$	-
SOOT11	21	03 Dec 2010	Diesel	1900.00	39.40		210.74	1.28	$5.542 \cdot 10^{10}$	-
SOOT11	24	03 Dec 2010	Diesel w/o pf	110.00	57.04		210.02	1.47	$2.079 \cdot 10^{10}$	-

campaign IN09 and IN11. However, these experiments were re- evaluated because of the evaluation algorithm. In Figure 3.8(b), the soot samples are listed with increasing OC mass content. Typical error bars for temperature and ice saturation ratio are shown for one data point. Note that the deposition nucleation INAS densities are not just upper limit values as were reported for soot immersion freezing.
Deposition nucleation was observed for temperatures from 195 K to 235 K within INAS densities ranging from $9 \cdot 10^8\,\mathrm{m}^{-2}$ to $8 \cdot 10^{13}\,\mathrm{m}^{-2}$. The INAS density data for a higher OC mass content (≥ 20 wt%; triangles and diamonds) lie at higher ice saturation ratios than the results for a lower OC mass content (circles and squares), clearly showing that the OC material suppresses the deposition nucleation activity of the soot particles. This is in agreement with the findings of Möhler et al. (2005b) who also found a decreasing deposition nucleation activity of CAST soot with increasing OC mass content.

3.2.2.c. Parametrization and Discussion

The measured deposition nucleation data for low OC content soot aerosol with u- shaped INAS density isolines was fitted with the following equation.

$$n_S(T, S_i, \text{aerosol}) = \exp\left\{\alpha\ (S_i - 1)^{1/4}\ \cos\left[\beta\ (T - \gamma)\right]^2\ \operatorname{arccot}\left[\kappa\ (T - \lambda)\right]/\pi\right\}\ \mathrm{m}^{-2} \tag{3.11}$$

$$\operatorname{arccot}(x) := \frac{\pi}{2} - \arctan(x)$$

The five parameters $\alpha, \beta, \gamma, \kappa$ and λ determine the saddle point of the isolines, the steepness of the isolines left and right from the saddle point and the distance between the isolines. In order to get the best fit values, the data points were classified according to their order of magnitude of the INAS density. The classified data set was then fitted for a constant INAS density only as a function of temperature and extrapolated beyond the data points. The parametrization is only valid for ice saturation ratios ranging from 1.0 to the homogeneous freezing threshold and water saturation, resp. The values of the five parameters for soot with an OC mass content of less than or equal 20 wt% are listed in Table 3.7. This parametrization approach is also used for the dust deposition

Table 3.7.: Fit parameter of Eqn.3.11 for desert dust and soot with an organic carbon content of less than or equal 20 wt%.

Aerosol	α	β	γ	κ	λ	valid T range
Desert Dust	285.692	0.017	256.692	0.080	200.745	[206 K,240 K]
Soot (OC $\leq$ 20 wt%)	46.021	0.011	248.560	0.148	237.570	[195 K,235 K]

nucleation data set, although no AIDA ice nucleation measurements with desert dust were performed so far for temperatures lower than 206 K. U-shaped isolines for the ice nucleation efficiency of minerals and ATD were found in laboratory studies (Welti et al., 2009; Hiranuma et al., 2014b; Koehler et al., 2010) guiding the shape of the INAS density isolines for desert dust below 206 K. The fit parameter values for desert dust excluding the sample CID1 are listed in Table 3.7. Figure 3.9 shows the parametrization for (a) soot and (b) desert dust together with an INAS density isoline of $n_S = 10^{11}\,\mathrm{m}^{-2}$ and the data points within $5 \cdot 10^{10}\,\mathrm{m}^{-2}$ and $5 \cdot 10^{11}\,\mathrm{m}^{-2}$.

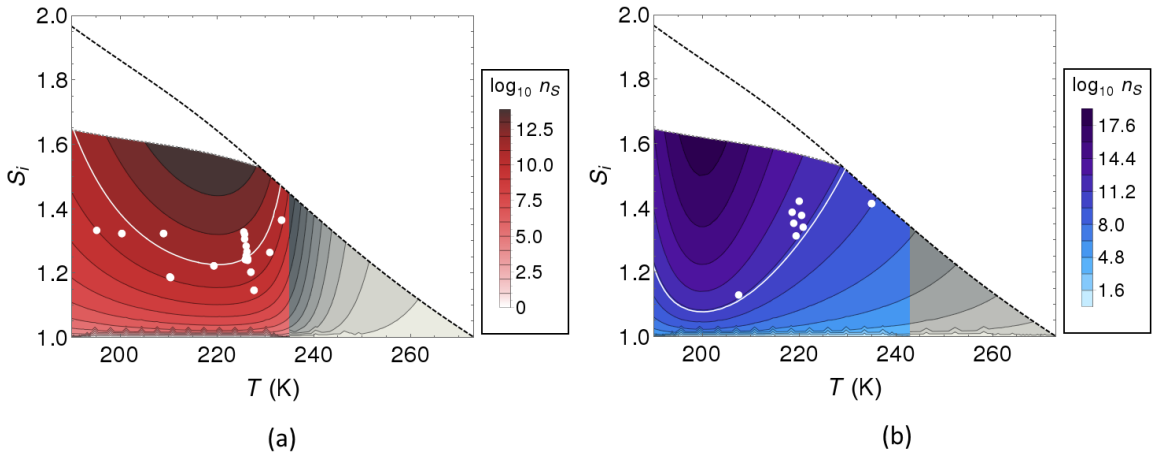

Figure 3.9.: Parametrization of the INAS density n_S as a function of temperature T and ice saturation ratio S_i using Eqn.3.11 and the fit parameters listed in Table 3.7 for (a) soot with OC$\leq$ 20 wt% and (b) desert dust only including data points from samples AD1, AD2, ID1 and SD2. The root mean square error for $\log_{10} n_S$ is for soot 1.08 and for desert dust 1.87. The black dashed line indicates the ice saturation ratio at water saturation and the gray dotted line the homogeneous freezing threshold for solution droplets ($\Delta a_w = 0.34$, Koop et al., 2000). The white solid line shows the isoline for $n_S = 10^{11}\,\mathrm{m}^{-2}$ and the white points are the corresponding data points.

Note that INAS densities above about $3 \cdot 10^{15}\,\mathrm{m}^{-2}$ (assuming spherical particles with diameters less than 0.01 μm) are not relevant for atmospheric ice nucleation. The extrapolation on the temperature scale is discussed in section 3.2.3. The u-shaped form of the INAS density isolines was already suggested by Hoose and Möhler (2012). The authors defined three regimes determining the ice nucleation behavior below water saturation. The three regimes can be identified in the data set of the soot and are shown as gray boxes in Figure 3.8(b). In regime A, the isolines decrease with increasing temperature showing that for the same ice activity a higher ice supersaturation is required. Thomson et al. (2015) explained this behavior from theory with the pressure induced rarification of the water vapor which leads to an increase in ice saturation ratio and therewith to the limitation of ice nucleation. Regime B is a transition regime

between A and C and is defined by nearly horizontal isolines meaning that n_S only depends on the ice saturation ratio alone. In regime C, the isolines increase very steeply towards water saturation indicating a strong temperature dependence. Therefore, it is assumed that ice nucleation in regime C is not dominated by the classical deposition nucleation mechanism, but rather influenced by the pore condensation and freezing (PCF) mechanism as recently suggested by Marcolli (2014). This mechanism was recently demonstrated by Wagner et al. (2016) by AIDA ice nucleation experiments with minerals, desert dust and soot.

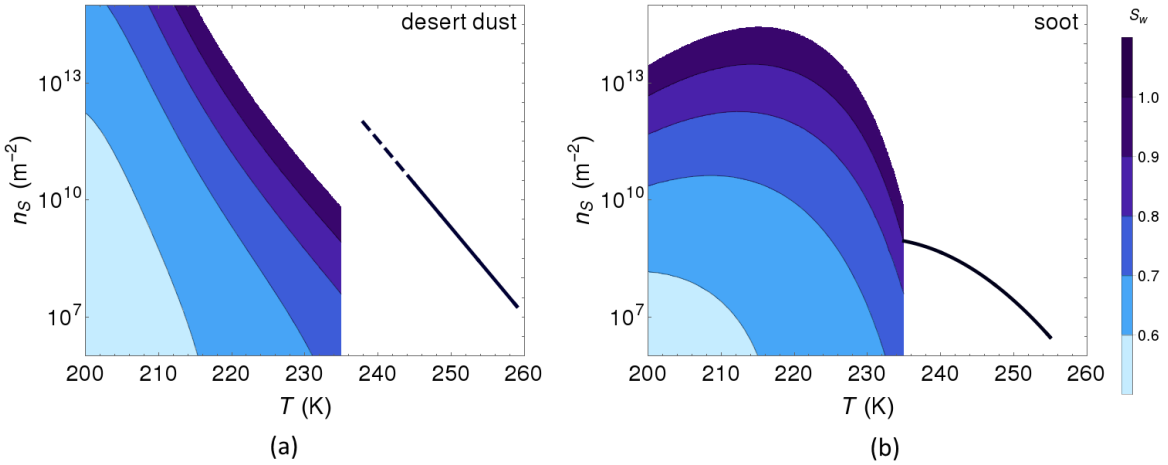

Figure 3.10.: Comparison of the INAS density parametrization for immersion freezing (single dark blue line) and deposition nucleation (blue contours) for different water saturation ratios for (a) desert dust with a linear extrapolation of the immersion freezing line (dashed) and (b) soot.

Figure 3.10 shows a comparison of the immersion freezing parametrization and the deposition nucleation parametrization for desert dust and soot. The linear extrapolation of the parametrization line for immersion freezing on desert dust to temperatures between 238 K and 245 K would result in two orders of magnitude higher INAS densities than the deposition nucleation isoline close to water saturation. For soot, both parametrizations yield similar INAS density values at water saturation and a temperature of about 238 K. However, the n_S parametrization for soot immersion freezing is only an estimate for the upper limit. For soot, the n_S isolines below water saturation are much steeper than the line for immersion freezing, indicating a change in the nucleation mechanism. Because of the steepness of the isolines and this distinct change in the slope at water saturation, the data suggests that as part of the PCF mechanism the confined water in the pores and cavities freezes homogeneously. For desert dust the isolines below water saturation are much flatter and show a similar slope as the immersion freezing parametrization

line. This indicates that the water in pores and cavities of desert dust particles may freeze heterogeneously.

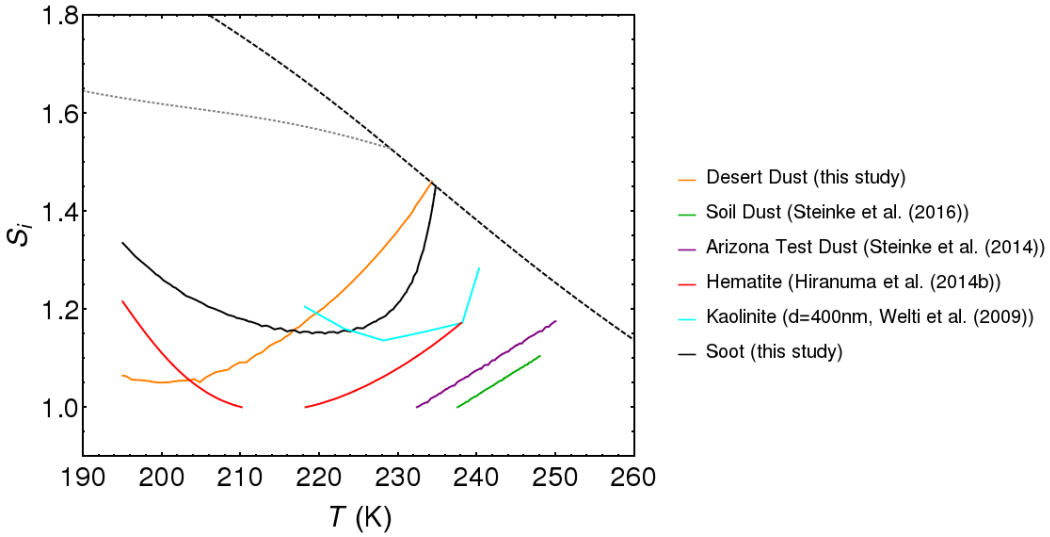

Figure 3.11.: Comparison of the new parametrization for deposition nucleation on desert dust and soot with parametrizations for soil dust, Arizona Test Dust and the dust components hematite and kaolinite. In behalf of clarity only isolines for $n_S = 10^{10}\,\mathrm{m}^{-2}$ are shown. Note that all shown parametrizations are only valid for $S_i \geq 1.0$. The black dashed line indicates the ice saturation ratio S_i at water saturation and the gray dotted line the homogeneous freezing threshold for solution droplets ($\Delta a_w = 0.34$, Koop et al., 2000).

3.2.2.d. Comparison to Other Deposition Nucleation Parametrizations

Figure 3.11 shows a comparison of the new parametrization for desert dust and soot below water saturation with parametrizations from the literature for soil dust (Steinke et al., 2016), ATD (Steinke et al., 2015) and hematite (Hiranuma et al., 2014b) and n_S values derived from measurements with kaolinite (Welti et al., 2009). For clarity, only isolines for INAS densities of $10^{10}\,\mathrm{m}^{-2}$ are shown. Comparing the natural dust and dust components parametrization lines, the desert dust is less ice active below water saturation. The higher ice activity of the soil dust might be explained by some biological or organic materials. Note that the ice nucleation in the temperature range between 230 and 250 K was suggested to be triggered by the PCF mechanism, influenced by the porous structure of the samples. ATD might have more suitable cavities in form of cracks due to the milling during manufacturing. Also the soil dust samples might show a more suitable pore structure than desert dust because of the organic or biological materials on the surface. This may explain the higher ice nucleation activity of the CID1 sample, which was excluded from the parametrization fit.

The soot shows a higher ice nucleation activity than the desert dust in the temperature range between 215 K and 235 K. However, soot is less ice active compared to soil dust, ATD and the dust components hematite and kaolinite.
One striking feature shown in Figure 3.11 is the similar slope of all dust sample isolines, which are much flatter than the soot isoline. This supports the suggestion of the previous section, that the pore water freezes homogeneously for soot and heterogeneously for dusts.

3.2.3. Discussion of Potential Use in Models

Various types of parametrizations for the heterogeneous ice nucleation ability of aerosols have already been published. Parametrizations based on CNT (Hoose et al., 2010; Chen et al., 2008; Barahona, 2012; Savre and Ekman, 2015) depend on parameters which are difficult to determine. Therefore, the free parameters like contact angle or surface tension differ significantly from study to study. Additionally, the results of these parametrizations do not agree with laboratory results over the whole temperature range (Hoose and Möhler, 2012). Especially, the suppression of deposition nucleation for warmer temperatures is not reproduced. Savre and Ekman (2015) recently presented a parametrization based on CNT addressing this issue by introducing a contact angle distribution function and therewith matching better laboratory observations. However, CNT- based parametrizations using contact angle distributions are complex to implement in models and need generally more computing time, in particular if the depletion of the most efficient INP is taken into account.
The second type of parametrizations is empirical. Here, the most commonly used aerosol specific parametrization framework is that of Phillips et al. (2008, 2013). The framework is based on laboratory as well as field studies and includes also the suppression of deposition nucleation for warmer temperatures. Some of the numerous input parameters that define e.g. the aerosol composition are difficult to be derived from atmospheric measurements (DeMott et al., 2010). More simpler descriptions of heterogeneous ice nucleation (e.g. DeMott et al., 2010, 2015) are easier to use in models but, in general, are not applicable to all atmospherically relevant conditions or atmospherically relevant aerosol types. In the case of a Saharan dust layer, DeMott et al. (2015) showed good agreement between their parametrization and the AIDA based parametrization of Niemand et al. (2012).
Until now, there is no parametrization framework available which is based on well-constrained laboratory experiments covering the whole atmospherically relevant temperature and humidity range. The parametrization framework presented here is in principle limited to the detection limits of the AIDA cloud chamber instruments and

the number of evaluated experiments. Therefore, also the AIDA parametrization has to be extrapolated to cover the atmospheric relevant temperature and ice saturation ratio ranges when used in models. In particular in the cirrus regime, ice nucleation data is lacking at high ice supersaturation and temperatures below 200 K which makes the parametrization more uncertain in these regions.
The dashed red lines in the upper panel of Figure 3.12 show the proposed extrapolation of the developed immersion freezing parametrization. The parametrization line is not extrapolated to higher temperatures, because this study as well as previous laboratory studies did not observe ice nucleation of desert dust as well as main dust components above 260 K (Hoose and Möhler, 2012). Below 245 K and the homogeneous freezing temperature, the parametrization is linearly extrapolated, because DeMott et al. (2011) showed no leveling off of the ice active fractions from different measurements with Saharan dust. For soot, the rescaled parametrization line from Murray et al. (2012) is simply extrapolated either to the homogeneous freezing temperature and to the melting temperature. Below water saturation and temperatures above 240 K, the ice activated fraction is much lower than 1 % for a typical aerosol diameter of 1 μm. Therefore, the extrapolation to warmer temperatures is unproblematic (see Fig. 3.9). However, the extrapolation to higher ice saturation ratios has to be limited to INAS densities less than or equal $1.0 \cdot 10^{15}\,\mathrm{m}^{-2}$.
The parametrization framework developed in this study is simple to implement into models. If the dust and soot surface area is provided in size bins, the number of INPs can be calculated via

$$n_{INP}(T, S_i) = \sum_j n_{dust,j}\ \left(1 - \exp\left(-n_S\, S_{dust,j}\right)\right) + \sum_l n_{soot,l}\ \left(1 - \exp\left(-n_S\, S_{soot,l}\right)\right). \tag{3.12}$$

Where j is the index of size bins for dust and l the index of the size bins for soot. n_{ae} is the number concentration and $S_{ae,j}$ the surface area of dust or soot in the size bin. If only the total surface area is available, this equation can be simplified to

$$n_{INP}(T, S_i) = n_{dust}\ \left(1 - \exp\left(-n_S\, S_{dust}\right)\right) + n_{soot}\ \left(1 - \exp\left(-n_S\, S_{soot}\right)\right). \tag{3.13}$$

The aerosol number concentration and surface area are usually either predicted by interactive aerosol modules in regional or global models (Vogel et al., 2009; Stier et al., 2005) or can be prescribed from climatologies (Hande et al., 2015). To calculate the maximum ice saturation ratio S_i reached in models, a algorithm taking into account the competition between homogeneous freezing and heterogeneous ice nucleation (e.g Barahona and Nenes, 2009b; Kärcher et al., 2006) should be used.

Figure 3.12 shows the new parametrizations for desert dust and soot together with

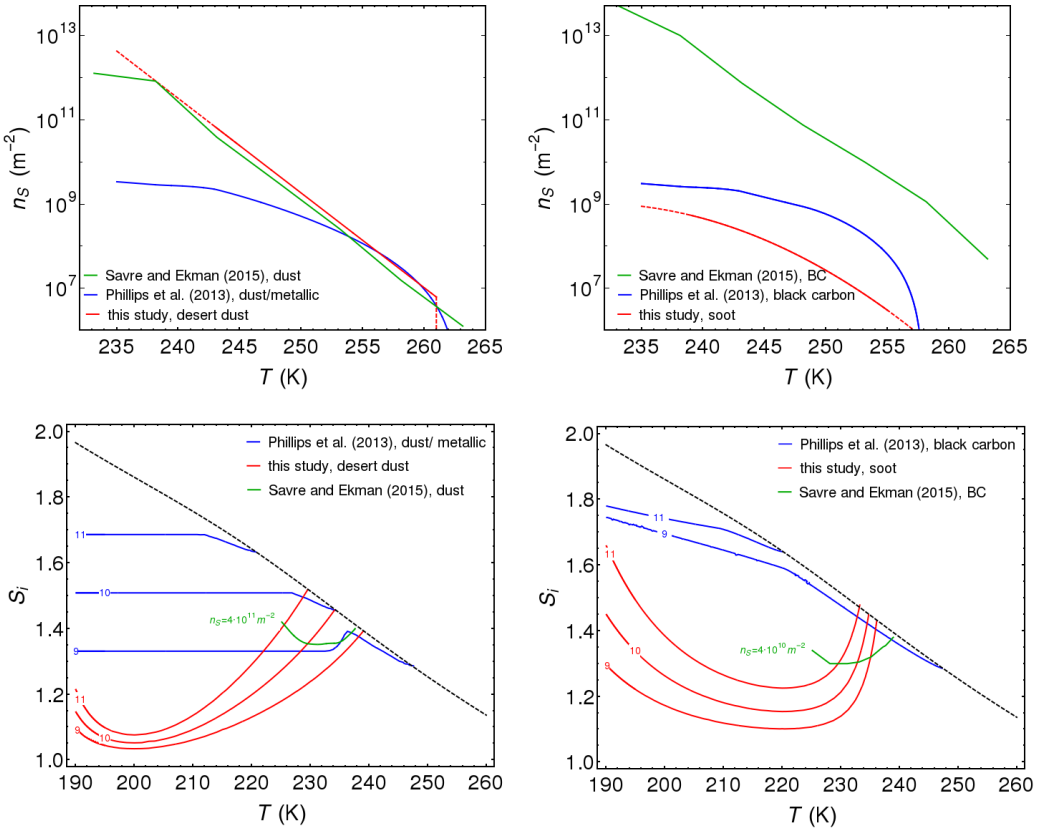

Figure 3.12.: Comparison of the new parametrization framework for desert dust and soot with the equivalent INAS density (Hoose and Möhler, 2012) of Phillips et al. (2013) and of Savre and Ekman (2015) in the immersion freezing (upper panel) and deposition nucleation regime (lower panel). The new parametrization for immersion freezing is extrapolated to $T \in [235, 261]$ K for desert dust and to $T \in [235, 273]$ K for soot. For the black carbon group of the Phillips parametrization $\Xi = 0.1$. The small colored numbers on the isolines in the lower panel indicate the exponent x for $n_S(T, S_i) = 10^x\,\mathrm{m}^{-2}$.

the schemes of Phillips et al. (2013) and Savre and Ekman (2015). For the Phillips parametrization the equivalent INAS density (Hoose and Möhler, 2012) is shown, with the black carbon IN propensity fraction of $\Xi = 0.1$. The equivalent INAS densities for the Savre and Ekman (2015) parametrizations were recalculated from the published ice active fractions and the median diameters (Eqn. (2.13)). As the parametrization for dust immersion freezing from Savre and Ekman (2015) is based on the data of Niemand et al. (2012), the parametrization line shows a quite similar behavior compared to the new line. In contrast, the Phillips et al. (2013) parametrization yields much lower INAS densities for $T \leq 253$ K. The "leveling off" behavior shown in both schemes is not supported by AIDA laboratory data. For soot immersion freezing, the scheme of Phillips et al. (2013) and the new framework show similar INAS densities, whereas Savre and Ekman (2015) yields up to 3 orders of magnitude higher INAS densities over

the whole temperature range. The leveling off for lower temperatures is not shown in the scheme of Savre and Ekman (2015).
For deposition nucleation, the scheme of Savre and Ekman (2015) covers only a small temperature range because of the used data sets (dust: Kanji et al., 2011; soot: Möhler et al., 2005a). Therefore, the application of this scheme is doubtful especially for cold cirrus clouds. However, the order of magnitude of the INAS density is comparable to the values of the new framework. The parametrization of Phillips et al. (2013) does not show the observed u- shaped isolines and shows overall lower INAS density values for a given temperature and ice saturation ratio for both dust and soot. Because of the shape of the isolines, the scheme of Phillips et al. (2013) would give significant INP concentration for soot only near water saturation. Below about 220 K the INAS densities from the Phillips parametrization are very small and for ice saturation ratios above 1.6, homogeneous freezing of solution droplets would be more likely.

4. Application in the COSMO-ART model

The parametrization framework introduced in the previous chapters can be used to predict the primary ice formation in models. In order to investigate the interaction of aerosol with mesoscale cloud systems a limited-area models are suitable.
In this chapter the application of the new parametrization framework in the COSMO-ART model will be shown. For that a case study was set up simulating a synoptically driven cirrus cloud, which was characterized by in-situ measurements in the aircraft campaign MACPEX in April 2011.

4.1. The COSMO-ART model

The COSMO (COnsortium for Small-scale MOdelling) model is the weather forecast model of the German weather service (DWD, Offenbach/ Germany) operating on a regional scale (meso-β and -γ). The ART (Aerosol and Reactive Trace gases) module is an online-coupled extension of the COSMO model treating the explicit interaction between aerosol and trace gases and atmosphere. The online-coupling has the benefit that the ART module can use the same spatial and temporal grid (Vogel et al., 2009). In order to take into account the spherical shape and rotation of the earth, spherical coordinates (λ_g, φ_g, z) are used in the COSMO model. However, the convergence of the meridians and the resulting singularity at the poles would cause numerical problems, which are overcome by transformation of the horizontal coordinates to rotated spherical coordinates (λ, φ, z). Those are derived by simply shifting the equator in a way it runs centered through the model domain. Therewith, for mesoscale model domains the problems of convergence are minimized. Because in most cases the ground of the model domain is not flat and some of the modelled variables depend on the topography, a terrain-following vertical coordinate ζ instead of a geographic coordinate z is used. This vertical coordinate $\zeta = \zeta(\lambda, \varphi, z)$ is set to be time-independent resulting in fixed isolines of ζ (Gal-Chen coordinate, Gal-Chen and Somerville, 1975). The influence of the topography on the vertical coordinate is damped with higher altitudes. Therefore, for

an altitude of $z_F \simeq 11430\,\mathrm{m}$ the terrain- following coordinate changes to a z-coordinate up to the top of the model domain at $z_T = 22700\,\mathrm{m}$.
For the numerical solution of the equation data set, the model domain is discretized using constant grid spacing in the following way.

$$\begin{aligned} \lambda_\imath &= \lambda_0 + (\imath - 1)\Delta\lambda & \imath &\in [1, N_\lambda] \\ \varphi_\jmath &= \varphi_0 + (\jmath - 1)\Delta\varphi & \jmath &\in [1, N_\varphi] \\ \zeta_k &= k & k &\in [1, N_\zeta] \end{aligned} \tag{4.1}$$

Where N_x for $x = \lambda, \varphi, \zeta$ is the number of grid points in x-direction and (λ_0, φ_0) corresponds to the south-west corner of the model domain. The discretized coordinates $(\imath, \jmath, k)$ describe the location in the centre of the grid box. The prognostic differential equations are solved numerically with a finite differences algorithm (3rd order Runge-Kutta scheme) and a two-level time splitting scheme (Wicker and Skamarock, 2002).

Table 4.1.: Hydrometeor classes in the implemented two- moment bulk microphysic scheme. nu and mu are the shape factors of the generalized Gamma distribution (Eqn. 2.17). m_{min} and m_{max} are the minimum and maximum mass of the particle, and $d_{p,min}$ and $d_{p,max}$ the corresponding diameters calculated via $d_p = a_{geo}\, m^{b_{geo}}$ (Seifert and Beheng, 2006).

cloud particle class	cloud droplet	rain	ice crystal	snow	graupel
ν	0	0	0	0	1
μ	1/3	1/3	1/3	0.5	1/3
a_{geo} (m kg$^{-b_{geo}}$)	0.124	0.124	0.835	2.4	0.15
b_{geo}	1/3	1/3	0.39	0.455	0.323
m_{min} (kg)	$4.2 \cdot 10^{-15}$	$2.6 \cdot 10^{-10}$	$1.0 \cdot 10^{-12}$	$1.0 \cdot 10^{-10}$	$1.0 \cdot 10^{-9}$
m_{max} (kg)	$2.6 \cdot 10^{-10}$	$3.0 \cdot 10^{-6}$	$1.0 \cdot 10^{-6}$	$2.0 \cdot 10^{-5}$	$5.0 \cdot 10^{-4}$
$d_{p,min}$ (μm)	2.0	79.1	17.4	67.6	185.6
$d_{p,max}$ (μm)	79.1	$1.8 \cdot 10^{3}$	$3.8 \cdot 10^{3}$	$17.5 \cdot 10^{3}$	$12.9 \cdot 10^{3}$

In the COSMO model the cloud microphysics is described by a two- moment bulk microphysic scheme based on the work of Seifert and Beheng (2006). In this scheme 6 hydrometeor classes (cloud droplets, rain, cloud ice, snow, graupel and hail) are distinguished each represented by a generalized Gamma distribution with constant shape factors (μ, ν) (see Ch. 2). The corresponding zeroth and third moments are used to describe number and mass concentration of the hydrometeors. Table 4.1 summarizes the shape factors as well as the minimum and maximum mass and diameters for each hydrometeor class as set in the COSMO two- moment scheme. With the coupling of the ART module to the cloud microphysics, the formation of cloud droplets and cloud ice

depends on the aerosol. In the ART module the aerosols are categorized with respect to their chemical composition and size, so called modes. These modes are described in the aerosol module $\text{MADE}^{\text{extended}}_{\text{soot}}$ and are represented by lognormal probability density functions (PDF) (see Eqn. (4.2) for the number size distribution).

$$f_{N,l}(d_p) = \frac{n_p, l}{\sqrt{2\,\pi}\,\ln\sigma_{g,l}}\,\exp\left(-\frac{\left(\ln d_p - \ln\overline{d}_{p,l}\right)^2}{2\,\ln^2\sigma_{g,l}}\right) \tag{4.2}$$

Where $n_{p,l}$ is the aerosol particle number concentration, $\sigma_{g,l}$ die geometric standard deviation and $\overline{d}_{p,l}$ the median diameter of the particles in mode l. In the standard version of the ART module 12 overlapping modes are prescribed (see Table 4.2) representing the most abundant aerosol types in the atmosphere. The total aerosol number size PDF is given by the sum of all modes.

$$f_N(d_p) = \sum_l f_{N,l}(d_p) \tag{4.3}$$

Five out of the 12 modes represent sub- micron particles. One of these modes represents pure soot directly emitted from anthropogenic sources. The other four modes represent internally mixed particles with and without soot in two different size ranges. Further, one mode corresponds to directly emitted coarse mode particles excluding soot (PM_{10}) and another 6 modes represent mineral dust and sea salt particles with three modes each. Table 4.2 summarizes all aerosol modes with their corresponding size range, chemical composition, geometric standard deviation and initial mass median diameter. As for the hydrometeors, two moments (see Eqn. (2.4)) of the PSD are used to describe the physical properties of the aerosol population. In particular, the zeroth (number concentration) and the third moment (mass concentration) of the lognormal size distribution are used. For mineral dust and sea salt emission and transport schemes are implemented into the ART module. The emissions are parametrized as a function of atmospheric state and surface properties (Vogel et al., 2006; Lundgren et al., 2013). The precursor substance for sea salt DMS[1] is given by external data sets. Both aerosol types are not allowed to interact with other particles or gases. The formation and interaction of the internally mixed particles is treated in the RADMKA[2] (Vogel et al., 2009) and the SORGAM[3] (Schell et al., 2001) mechanisms. The initial concentration of the precursor gases and soot are given by external data sets from e.g. global chemical models. The recently

[1]DiMethyl Sulfide
[2]Regional Acid Deposition Model version KArlsruhe
[3]Secondary ORGAnic Model

implemented plume rise model (Walter, 2014) treats the emission and transportation of trace gases and aerosol from wildfires.

Table 4.2.: Aerosol classes treated in the ART module with their corresponding size range, chemical composition, geometric standard deviation and initial mass median diameter. (From Bangert, 2012)

size mode	class	chemical composition	σ_g	d_m (μm)
Aitken	secondary mixed particles	SO_4^{2-}, NO_3^-, NH_4^+, H_2O, SOA	1.7	0.01
Aitken	internally mixed soot particles	SO_4^{2-}, NO_3^-, NH_4^+, H_2O, SOA, soot	1.7	0.08
Accum.	secondary mixed particles	SO_4^{2-}, NO_3^-, NH_4^+, H_2O, SOA	2.0	0.07
Accum.	internally mixed soot particles	SO_4^{2-}, NO_3^-, NH_4^+, H_2O, SOA, soot	2.0	0.08
Accum.	soot		1.4	0.08
Coarse	PM_{10}		2.5	1.0
Coarse	mineral dust A		1.5	1.7
Coarse	mineral dust B		1.6	6.7
Coarse	mineral dust C		1.7	14.2
Coarse	sea salt A		1.9	0.2
Coarse	sea salt B		2.0	2.0
Coarse	sea salt C		1.7	12.0

For the activation of aerosol particles a CCN and INP spectrum, resp., is calculated in dependence on the chemical composition and size of the aerosol and the supersaturation during cloud formation. Because the IN spectrum is more relevant for the case study discussed in Chapter 4.3, the CCN activation is not further addressed (see Bangert et al., 2012).

The formation of cloud ice particles in the model depends mainly on the relative humidity and temperature. These conditions determine whether homogeneous or heterogeneous ice nucleation (see Ch. 2.2) or both take place. For temperatures above 235 K or if already a liquid phase cloud exists solely heterogeneous ice nucleation takes place. Then, the ice number concentration is calculated for the grid-scale ice supersaturation and temperature using the parametrization scheme of e.g. Phillips et al. (2008) or using the framework presented in this work. For temperatures below 235 K the competition between homogeneous freezing and heterogeneous nucleation has to be considered. In the ART module, this competition is based on the algorithm given by Barahona and Nenes (2008, 2009a,b). The basis for this algorithm is the temporal evolution of the subgrid-scale ice saturation s_i in a Lagrangian air parcel (see Fig. 4.1). In this sketch the curves show an increase in s_i as expected in a rising air parcel. In the case no

aerosol is present, the increase in s_i (solid line) is less steep after passing the threshold s_i (s_{hom}) because of the deposition of water vapor on the ice particles. Because of the depletion of water vapor the ice saturation reaches at some time its maximum s_{max}. For pure homogeneous nucleation of solution droplets the threshold saturation s_{hom} is

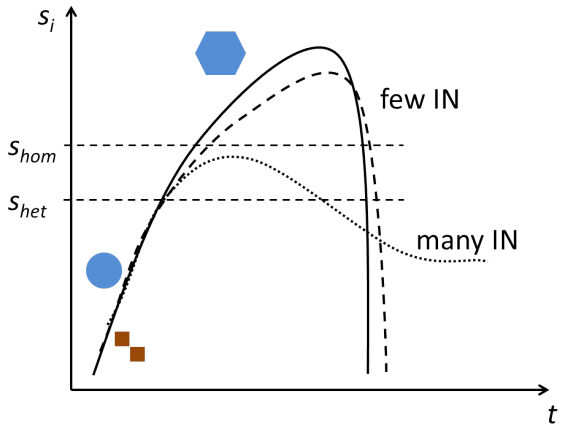

Figure 4.1.: Schematic of the parametrized temporal evolution of the ice saturation s_i for a constant vertical wind velocity. The black solid line shows the evolution for pure homogeneous nucleation of solution droplets above the threshold s_{hom}. The black dashed line shows the evolution for combined homogeneous and heterogeneous nucleation for a small IN concentration and the black dotted line shows the pure heterogeneous nucleation for a larger IN concentration above the threshold s_{het}. (Adapted from Barahona and Nenes, 2008)

smaller or equal the maximum ice saturation s_{max}. The presence of INPs lowers the maximum of s_i compared to the pure homogeneous case, because the heterogeneous ice particles are formed earlier and therefore, water vapor is consumed over a longer time. As long as s_{max} is larger than s_{hom} both nucleation mechanisms are competing with each other. If the number of potential INP is large enough, s_{max} becomes smaller than s_{hom} and homogeneous nucleation is completely inhibited. Equation 4.4 summarizes this competition algorithm.

$$n_{ice} = \begin{cases} n_{hom}(s_{hom}) + n_{het}(s_{hom}), & n_{het}(s_{hom}) < n_{lim} \\ n_{het}(s_{max}), & n_{het}(s_{hom}) \geq n_{lim} \end{cases} \tag{4.4}$$

Where n_{hom} and n_{het} are the ice number concentration formed by homogeneous nucleation and heterogeneous nucleation, resp., and n_{lim} is the threshold IN concentration completely suppressing homogeneous ice nucleation. The implemented threshold ice supersaturation for homogeneous nucleation s_{hom} is adopted from the parametrization

of Ren and MacKenzie (2005). The ice number concentration from homogeneous ice nucleation is calculated using the algorithm of (Barahona et al., 2010)

$$n_{hom}(s_{hom}) = \begin{cases} n_{sd}\, \exp\left(-f_c(s_{hom})\right)\, \left(1 - \exp(-f_c(s_{hom}))\right), & f_c < 0.6 \\ n_{sd}\, \left[1 + \exp\left(\frac{9-2f_c(s_{hom})}{7}\right)\right]^{-1}, & f_c \geq 0.6\ . \end{cases} \tag{4.5}$$

Where n_{sd} is the number concentration of supercooled droplets formed from secondary mixed particles and sea salt particles (see Tab. 4.2), and f_c is the fraction of frozen droplets taking into account the competition between homogeneous and heterogeneous ice nucleation

$$f_c(s_{hom}) = f_{c,hom}\, \left[1 - \left(\frac{n_{het}(s_{hom})}{n_{lim}}\right)^{3/2}\right]^{3/2} . \tag{4.6}$$

Where $f_{c,hom}$ is the fraction of frozen droplets for pure homogeneous ice nucleation (Barahona and Nenes, 2008). In the case of pure heterogeneous ice nucleation the maximum ice saturation s_{max} and the heterogeneous ice number concentration are calculated numerically by the bisection method following the algorithm of Barahona and Nenes (2009b)

$$n_{het}(s_{max}) = n^* \frac{1 + s_{max}}{\sqrt{\Delta s^*_{char}}\, s_{max}}\, \exp\left(\frac{2}{\lambda\, s_{max}}\right) . \tag{4.7}$$

Where n^* and λ summarize some thermodynamic variables (see Barahona and Nenes, 2009b, therein Appendix C), and Δs^*_{char} is the growth integral of the ice particle in dependence of s_{max}. The heterogeneous ice number concentration n_{het} is calculated via the in the model implemented heterogeneous ice nucleation frameworks (e.g. Meyers et al., 1992; Phillips et al., 2008, or the newly developed framework presented in this work).

For the case study presented in Chapter 4.3 the developed framework from AIDA laboratory measurements (see Ch. 3.2) and the framework of Phillips et al. (2008) are used. Therefore, the latter framework is also briefly described. As the framework presented in this work the Phillips framework is also based on the active site approach. The number of IN of aerosol species X (dust/ metallic, black carbon and insoluble organics) is calculated via

$$n_{IN,X} = \int_{\log(0.1\,\mu\mathrm{m}\,)}^{\infty} \left(1 - \exp\left[-\mu_X(D_X, T, S_i)\right]\right)\, \frac{\mathrm{d}n_X}{\mathrm{d}\log D_X}\, \mathrm{d}\log D_X\, , \tag{4.8}$$

where μ_X is the number of aerosol X activated to ice.

$$\mu_X = H_X(S_i, T)\,\xi(T)\,\frac{\alpha_X\, n_{IN,1,*}}{\Omega_{X,1,*}}\,\frac{\mathrm{d}\Omega_X}{\mathrm{d}n_X} \tag{4.9}$$

Where α_X is the fraction of aerosol X contributing to ice nucleation, $\Omega_{X,1,*}$ is the fraction of the total aerosol surface area of species X for particles with sizes of 0.1 μm to 1 μm in the background and ξ suppresses droplet freezing above 271 K. $H_X \in [0, 1]$ considers the scarcity of heterogeneous ice nucleation below water saturation, where $H_X \equiv 1$ at water saturation. Assuming spherical particles the last term is approximated by $\frac{\mathrm{d}\Omega_X}{\mathrm{d}n_X} \approx \pi\, D_X^2$, where D_X is the aerosol particle diameter. The variable $n_{IN,1,*}$ represents the reference aerosol spectrum, partly obtained from CFDC[4] measurements in various field campaigns. However, the measurements were only conducted at temperatures below 233 K. For temperatures above 248 K Phillips et al. (2008) rescaled the parametrization of Meyers et al. (1992) and for temperatures between 248 K and 233 K Phillips et al. (2008) interpolated between this and the parametrization obtained from measurements.
From Equation (4.9), an equivalent INAS density (Hoose and Möhler, 2012) can be extracted.

$$\tilde{n}_{S,X} = \frac{\mu_X}{\pi\, D_X^2} = H_X(S_i, T)\,\xi(T)\,\frac{\alpha_X\, n_{IN,1,*}}{\Omega_{X,1,*}} \tag{4.10}$$

Herewith, a direct comparison with the framework developed in this work is possible. Figure 4.2 shows the comparison of the equivalent INAS density of Phillips et al. (2008) as implemented in the ART model (sPDA08) and the INAS density parametrization from this work (U16) for dust and soot in immersion freezing mode as well as deposition nucleation mode. For immersion freezing the sPDA08 scheme shows a discontinuity at 243 K. This is due to the simplified reference aerosol spectrum from Phillips et al. (2007) implemented for the Phillips scheme in the ART model. Compared to the sPDA08 scheme, the U16 framework predicts higher INAS densities below 243 K for both aerosol types. For BC aerosol the U16 framework yields smaller INAS densities above this temperature, whereas for dust the U16 frameworks shows higher values between 243 K and about 255 K and smaller values above 255 K. In general, the sPDA08 scheme shows a much flatter slope meaning a weaker temperature dependency compared to the U16 framework.
In deposition nucleation mode the differences between both frameworks are even more obvious. Within the atmospherically relevant temperature range, the sPDA08 scheme shows much lower INAS densities compared to the U16 framework. Furthermore, the sPDA08 scheme does not show u-shaped isolines as predicted by U16. Because of the shape of the isolines, the sPDA08 scheme yields significant INP concentration for soot

[4]Continuous Flow Diffusion Chamber

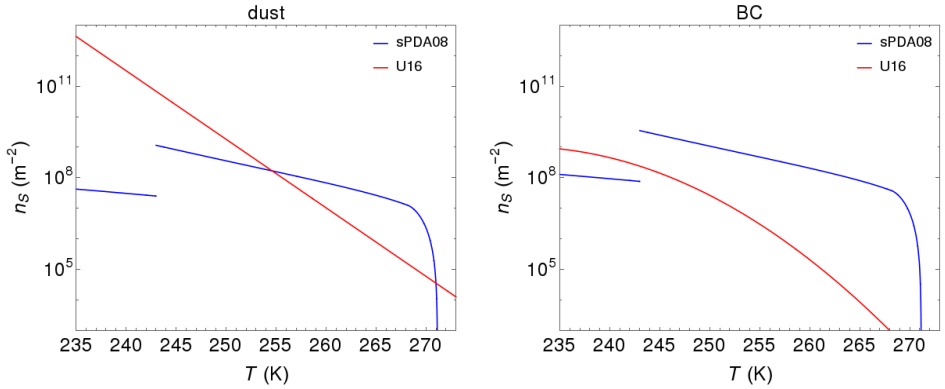

(a) immersion freezing

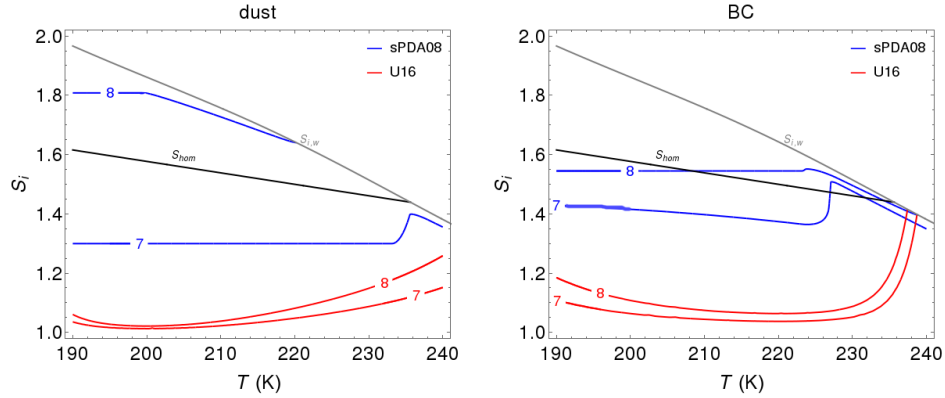

(b) deposition nucleation

Figure 4.2.: Comparison of the INAS density parametrization developed in this study (U16) and the equivalent INAS density parametrization of Phillips et al. (2008) as implemented in the COSMO- ART model (sPDA08). The upper panel shows the comparison for immersion freezing, the lower panel for deposition nucleation. For deposition nucleation isolines of n_S are shown, where the small colored numbers indicate the exponent x of $n_S = 10^x\,\mathrm{m}^{-2}$.

only near water saturation. However, because of the small INAS densities obtained from the sPDA08 scheme below $T \approx 220\,K$ and above $S_i \approx 1.6$, homogeneous nucleation of solution droplets would be more likely.

Based on the INAS density framework developed in Chapter 3.2 and summarized in Figure 4.2, the INP number concentration can be easily calculated - if the dust and soot surface area is provided in size bins - via

$$n_{INP}(T, S_i) = \sum_j n_{dust,j}(1 - \exp\left(n_S\, S_{dust,j}\right)) + \sum_l n_{soot,l}(1 - \exp\left(n_S\, S_{soot,l}\right)) \,. \tag{4.11}$$

Where j is the index of the dust mode and l the index of the soot mode. n_X is the number concentration and S_X is the surface area for dust or soot. In case of the COSMO- ART model the dust aerosol has three modes (see Tab. 4.2). For soot the modes for pure soot and the secondary mixed particles containing soot (see Tab. 4.2) are summed up to one mode with median diameter and geometric standard deviation from the pure soot mode. The surface area concentration s is calculated from the aerosol number size distribution (Eqn. (4.2)) via the Hatch- Choate conversion (Heintzenberg, 1994)

$$s_j = \pi\, n_j\, \exp\left(2\, \ln \overline{d_{n,j}} + 2\, \ln^2 \sigma_{g,j}\right)\ . \tag{4.12}$$

Where $\overline{d}_{n,j}$ is the median diameter of the number size distribution and $\sigma_{g,j}$ is the geometric standard deviation of mode j. s_j and n_j are the surface area concentration and number concentration, resp.

4.2. Field Campaign MACPEX

4.2.1. Scientific Goal and Instrumentation

The NASA Mid- latitude Airborne Cirrus Properties EXperiment (MACPEX) campaign was dedicated to determine the microphysical properties of ice crystals in mid-latitude cirrus clouds. Especially, the occurrence and influence of small ice crystals and the contribution of aerosol particles as INP in cirrus clouds was addressed. During the campaign in March and April 2011 the NASA science aircraft WB-57F started from Ellington Field/ Texas, U.S. on 14 science flights in synoptic and anvil cirrus clouds over south central U.S.

In order to accomplish the scientific goals of the campaign, the WB-57F was equipped among others with instruments measuring ice particle size, habit and residuals, aerosol concentration and composition, and water vapor concentration. These instruments used for the following comparison are briefly described.

The meteorological situation in terms of pressure, temperature and wind was measured with the Meteorological Measurement System (MMS) (Scott et al., 1990). For the determination of the water vapor content several instruments were flown, but the Harvard Water Vapor (HWV) is used in this study because it provided the most continuous data. The HWV instrument is a combination of a Lyman-α photofragment fluorescence instrument and a tunable diode laser direct absorption instrument. It is designed to determine the water vapor volume mixing ratio (VMR) (Weinstock et al., 2009). The aerosol size distribution and total aerosol concentration were measured by two instruments: the Focused Cavity Aerosol Spectrometer (FCAS) II and the Nuclei-Mode Aerosol Size Spectrometer (NMASS). The FCAS II instrument measures the size of particle in the range from about 100 nm to about 2000 nm passing a laser beam in an optical cavity (Jonsson et al., 1995). The NMASS instrument consists of 5 parallel Condensation Nuclei Counters (CNC) and measures the size-resolved aerosol concentration for particles ranging between 4 nm and 60 nm (NASA, 2012a). Especially for the BC/ soot aerosol, a Single Particle Soot Photometer (SP2) was equipped. The SP2 instrument delivers the BC mass concentration of either pure BC as well as internally mixed BC particles in the size range of 90 nm to 600 nm volume- equivalent diameter (Schwarz et al., 2006). A laser beam inside the SP2 heats up passing particles and evaporates non-refractory coatings. Further laser heating lets the BC cores emit thermal radiation which is correlated to the BC mass. The Particle Analysis by Laser Mass Spectrometry (PALMS) instrument measures the chemical composition of particles. The sampled particles can be either aerosol particles or residuals of ice particles. The particles of $0.2\,\mu\text{m} \leq d_p \leq 3\,\mu\text{m}$ are desorbed and ionized with a laser and characterized

with a time-of-flight mass spectrometer (Thomson et al., 2000; Cziczo et al., 2006). Also the ice particle size distribution and ice particle concentration are measured by several instruments. The Video Ice Particle Sampler (VIPS) and the Small Ice Detector (SID) 3 detect ice crystals up to a diameter of 200 μm. The VIPS collects continuously particles on a loop belt coated with silicon oil and images these particles, whereas the SID3 detects the scattering intensity of a particle passing a laser beam. Larger ice crystals and snow particles are detected with the High Volume Precipitation Spectrometer (HVPS) and the 2D-S Stereo Probe. The 2D-S uses two orthogonal laser beams to image the two- dimensional shadow of the particles passing a cross section of the two laser beams (Lawson et al., 2006b). From the shadows particle size and habit are determined. The HVPS uses the same mechanism but a larger detection volume. Therefore, combined measurements of 2D-S and HVPS can probe particles with diameters from 10 μm up to about 2 cm (NASA, 2012a). Because of the detection method of the VIPS and the 2D-S/ HVPS the given diameter is an area- equivalent geometric diameter. However, SID3 measures an optical diameter (Vochezer et al., 2016).

4.2.2. Main Scientific Findings

Apart from the numerous publication about instrument improvements and measurement data from the MACPEX campaign (e.g. Cziczo and Froyd, 2014; Schmitt et al., 2016), modelling studies are much scarcer. Studies by e.g. Krämer et al. (2016); Kienast-Sjögren et al. (2015) used the in- situ data from the MACPEX field campaign to validate their modelling results. Jensen et al. (2013), however, used the data sets to initialize a model simulation. The objective of this work was to determine the influence of heterogeneous ice nucleation on the physical properties of cirrus clouds. Therefore, Jensen et al. (2013) analyzed the measured ice number concentration for the synoptically driven cirrus cloud cases and found a good agreement between VIPS and 2D-S instrument. In the case of synoptic cirrus clouds probed during the MACPEX campaign, ice number concentrations of less than 1000 L^{-1} were observed. Ice number concentration larger than 20 L^{-1} were predominantly found in the upper part of cirrus clouds where homogeneous ice nucleation dominates. Concentration lower than 20 L^{-1}, on the other hand, were observed in the lower part of cirrus clouds and suggest the presence of heterogeneous ice formation. In order to determine the contribution of heterogeneous ice nucleation to the observed ice number concentration, Jensen et al. (2013) simulated with the 1D CARMA[5] model the formation and evolution of cirrus clouds driven by the temperature and vertical velocity profiles from the aircraft measurements. In comparison to the observed ice number concentration, pure homogeneous ice nucleation

[5]Community Aerosol and Radiation Model for Atmospheres

underestimated the ice number concentration at temperatures between 225 K and 235 K. Below this temperature, the modelled and measured ice number concentrations were in good agreement. The authors included subsequently heterogeneous ice nucleation assuming INP concentrations of $20\,L^{-1}$ and $100\,L^{-1}$. In both cases, heterogeneous ice nucleation contributed most at temperatures above 225 K referring to the lower part of the cirrus cloud. However, homogeneous ice nucleation was not suppressed even for the high INP contribution.

These findings are in agreement with mass spectrometric analysis of residuals of ice particles sampled in cirrus clouds. Using the PALMS instrument aerosol particles sampled near-cloud and ice residuals sampled inside the cloud were analyzed. By comparing both measurements, Cziczo et al. (2013) found that 94 % of all cirrus clouds probed during 4 aircraft field campaigns (incl. MACPEX campaign) were formed by heterogeneous ice nucleation. The predominant particle class observed as IRP were mineral dust particles without a significant coating (Cziczo et al., 2013). Soot/ BC/ EC particles as well as biological particles were not found neither as background aerosol nor as IRP. The lack of soot/ BC/ EC particles is in contrast to other aircraft measurement campaigns (e.g. Twohy and Poellot, 2005; Pratt et al., 2009) or in- situ measurements at mountain top (e.g. Kamphus et al., 2010).

Nevertheless, the dominance of heterogeneous ice nucleation is also supported by the measured RH_i from the HWV instrument. The (normalized) frequency of RH_i exceeding 120 % is less than 5 % (Cziczo et al., 2013). Finally, Cziczo et al. (2013) suggested that the low ice number concentrations (less than $100\,L^{-1}$) also indicates the dominance of heterogeneous ice nucleation.

In the following chapter, one day of the MACPEX campaign is chosen where heterogeneous ice nucleation was found to be the predominant nucleation mechanism. The measurement data of this day will be compared to modelling results of this day.

4.3. Case Study

As recapitulated in the previous chapter, Jensen et al. (2013) used a 1D model in order to investigate the contribution of heterogeneously formed ice to the total ice concentration measured in synoptic cirrus clouds during the MACPEX campaign. Here, the newly developed parametrization framework is used to investigate this in the 3D mesoscale model COSMO- ART (see Ch. 4.1). In a case study the model results and aircraft measurements from one flight during the MACPEX campaign will be compared. For the presented case study a synoptically driven cirrus cloud on the 13th April 2011 over western Texas, U.S. and northern Mexico was selected. This cloud system was chosen, because a robust data base for IRP is available and suggests the dominance of heterogeneous ice formation (Cziczo et al., 2013).
The aircraft took off at 17.05 UTC north-westward up to an height of about 14.6 km. At 18 UTC the aircraft reached the tail of the cirrus system and descended into cirrus tops at about 10.5 km altitude. At 20 UTC the aircraft ascended again and returned to Ellington Field (see Fig. 4.3).

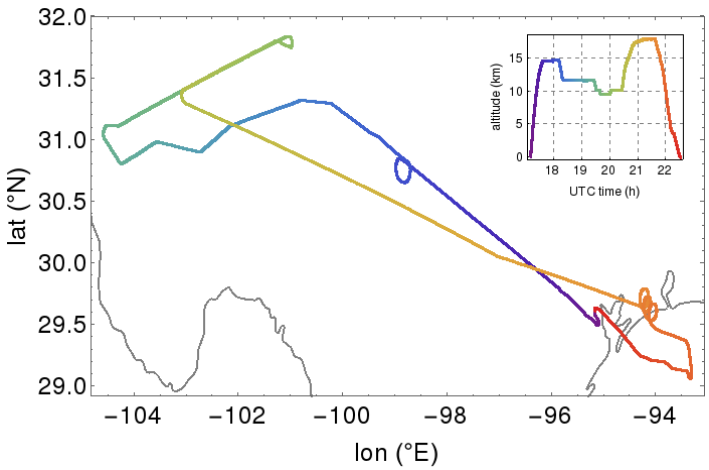

Figure 4.3.: Flight path of the research aircraft on 13th April 2011 (from NASA, 2012b). The color indicates the time-dependent altitude of the aircraft shown in the little picture in the upper right corner.

4.3.1. Meteorological Situation

On the 13th April 2011 a strong low pressure system south of the Alaskan- peninsula and a high pressure system over central north Mexico lead to a south- west flow from the Pacific Ocean over the Rocky Mountains (see Fig. 4.4(a)). On the leeward side a cirrus cloud started to form in the afternoon UTC (local time: UTC -6) (see Fig. 4.4(b)). As typical for this weather situation, no precipitation was observed.
Figure 4.5 shows vertical profiles of the temperature and relative humidity wrt. water

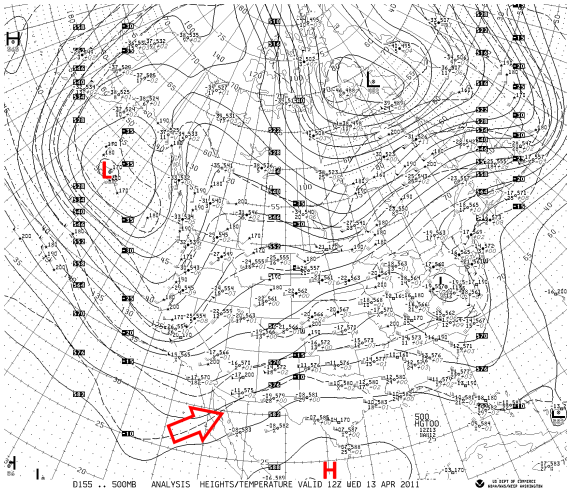

(a) Reanalyis map at 500 hPa pressure level at 12 UTC.

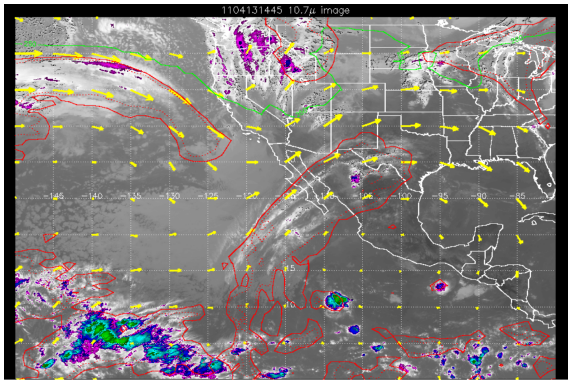

(b) Analyzed satellite image at 14.45 UTC.

Figure 4.4.: Maps of the meteorological situation on the 13th April 2011 over North America. (a) reanalysis map at 500 hPa pressure level (Colorado State University, 2011) with marked low and high pressure system causing south- west flow into south- central U.S. (b) satellite image (figure courtesy of Karl Froyd, NOAA, Boulder/ U.S.; personal communication) showing the start of the cloud formation. The yellow arrows show the wind direction and velocity and the red framed contours show the relative humidity.

from radio soundings started at three different locations in the measurement region (see Fig. 4.5(a)). The radio sounding at Ellington Field (green line) started at 20.05 UTC, whereas at Midland (reddish lines) and at Del Rio (blueish lines) the radiosondes started at 00 UTC on 12th April and 12 UTC on 13th April. From the temperature profile all soundings show an approximate height of the tropopause at about 15 km. The RH_i profile shows an increase in relative humidity over daytime and late evening. Furthermore, the profiles from the daytime and late evening show a sharp increase in RH_i at about 10 km which is likely due to the formation of the cirrus cloud.
Southern U.S. and especially Texas was afflicted by a drought which started in fall 2010 (Nielsen-Gammon, 2011). This unprecedented drought boosted the frequency of wildfires in the spring wildfire season leading to more than 3200 counted wildfires only in Texas and only in April 2011 (Jones et al., 2011).

4.3.2. Model Setup

For the case study the model was set to have a horizontal resolution of 0.0625° (≈ 7 km), 40 vertical layers reaching a height of 22700 m and a time step of one hour. The model domain (Fig. 4.6) covers an area between -104°E to -93°E and 20°N to 36°N, resulting in 176 × 112 gridpoints (see Eqn. (4.1)). The simulation started at 00 UTC on 12th

(a) Map of the location of the radio soundings shown in (b) and (c).

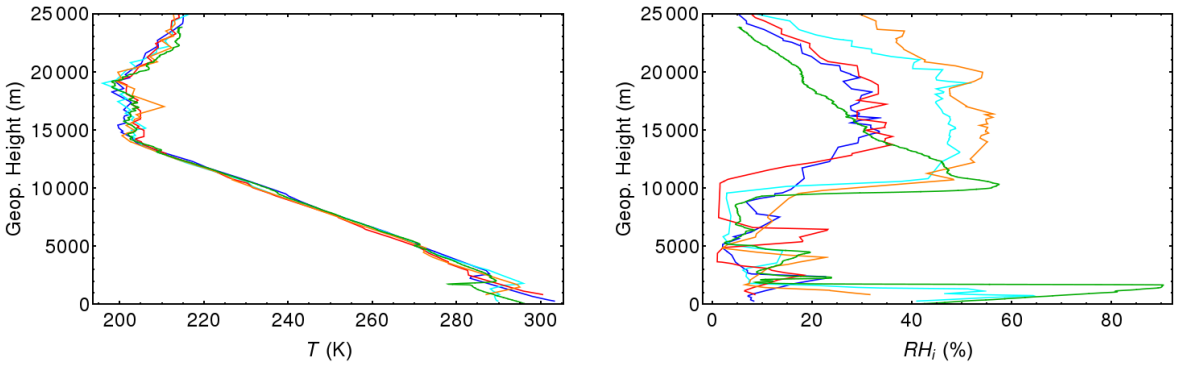

(b) (c)

Figure 4.5.: Map and vertical profiles of radio soundings at Ellington Field (green) started at 20.05 UTC (data obtained from NASA, 2012b), Midland (red: 12th April 00 UTC, orange: 13th April 12 UTC) and Del Rio (blue: 12th April 00 UTC, cyan: 13th April 12 UTC) (data obtained from University of Wyoming, 2011).

April 2011 and ended at 00 UTC on 14th April 2011 in order to cover the time of formation until start of depletion of the cloud system.

The simulation was driven by data from the GME global model of the German weather service. The initial and boundary data for the ART module was provided by MOZART[6]-4 data (Emmons et al., 2010). MOZART is a global chemical transport model for the troposphere and provides 85 gas phase species and 12 bulk aerosol compounds. For the present study only the gas phase species were used and pre-processed to match the name conventions of ART (see Tab.7 in Emmons et al., 2010). The anthropogenic emissions were given by the EDGAR[7] HTAP version 1 data set (Janssens-Maenhout et al., 2012). This harmonized global, gridded, air pollution emission data set is based on national emission inventories and reports the emissions for the years 2000 to 2005. The data set includes ozone precursor gases (CH_4, NMVOC, CO and NOx), acidifying gases (SO_2 and NH_3) as well as particular matter (PM_{10}, $PM_{2.5}$, BC and OC). Same as

[6]Model for OZone And Related chemical Tracers
[7]http://edgar.jrc.ec.europa.eu/

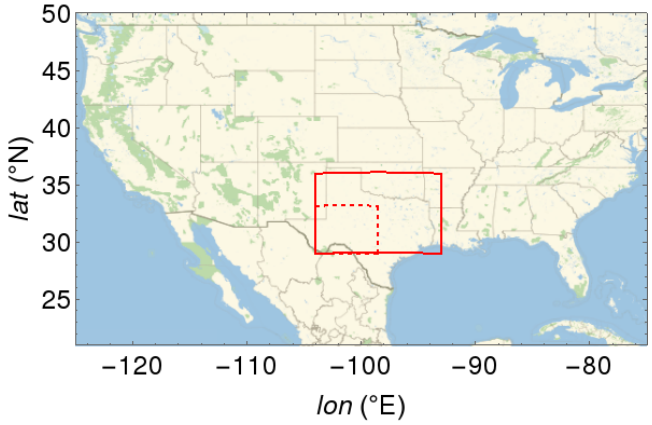

Figure 4.6.: Map of the model domain for the case study. The domain covers the area from -104.0 °E to -93.0°E and from 29.0°N to 36°N with a spatial resolution of 0.0625°. The area included in the red dashed box is a sub- domain picked for data evaluation.

for the MOZART data set, the data set had to be pre- processed in order to rename the species and distribute the NMVOC class to gas phase species used in the ART module (Dominik Brunner, EMPA, Dübendorf/ Switzerland; personal communication). Furthermore, the given NOx emissions were first classified by traffic and non- traffic emissions according to their UNFCCC[8] category. Afterwards, the NOx emissions from traffic were apportioned to 90 % NO and 10 % NO_2 (Knote, 2012), whereas the non-traffic NOx emissions were apportioned to 83 % NO and 17 % NO_2 (Grice et al., 2009). Biogenic emissions were evaluated from land cover classifications given by the GLOBAL Land Cover (GLC) data set for the year 2000 and the Fraction of Vegetation COVER (FCover). For local dust emissions the Harmonized World Soil Database (HWSD) was used. Non- regional dust emissions were taken into account using a global ICON-ART (Rieger et al., 2015) simulation started on the 1st April 2011 and ran until the 15th April 2011 with a resolution of about 40 km. This simulation showed a significant dust transport over the northern Pacific Ocean into the westerly part of the U.S. (see Fig. 4.7).

In spring 2011 a lot of wildfires in and around the model domain were detected and increased the aerosol load (Daniel J. Cziczo, MIT, Cambridge/ U.S.; personal communication). HYSPLIT[9] forward trajectories started on 12th April 2011 at 12 UTC show that also air from wildfire regions in north and north-west Mexico reach the model domain (see App. B). However, in the model only local biomass burning emissions can be treated using the Global Fire Assimilation System (GFAS) Version 1 data set provided by the ECMWF. The data set includes emissions of trace gases as well as particular matter from the smoke. Analogous to the EDGAR HTAP v1 data set, the

[8]United Nations Framework Convention on Climate Change
[9]http://ready.arl.noaa.gov/hypub-bin/trajtype.pl?runtype=archive

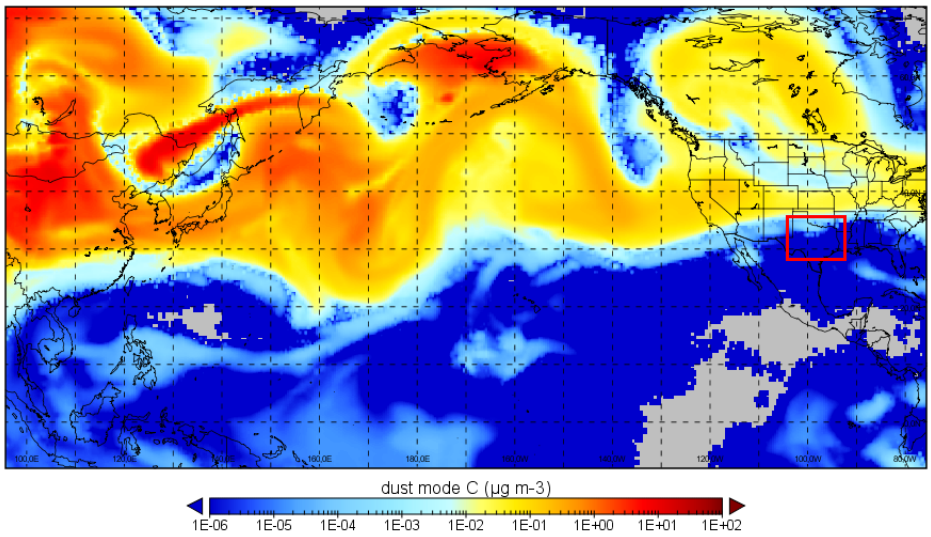

Figure 4.7.: Coarse mode dust at 8 km height on 13th April 2011 at 12 UTC simulated with ICON-ART. The other dust modes are shown in Appendix B. The red rectangle indicates the model domain.

NOx emissions from biomass burning were apportioned to 90 % NO and 10 % NO_2. Furthermore, the OC and PM2.5 emissions were apportioned to 90 % Accumulation mode and 10 % Aitken mode (Carolin Walter, KIT, Karlsruhe/ Germany; personal communication).
Table 4.3 summarizes all input data sets used for setting up the model. In order to compare the model results with the in-situ measurements in a good way a sub- domain lying in the upper left corner of the model domain is used for the model data averaging (see Fig. 4.6). Furthermore, unless otherwise stated the model data is averaged over four hours from 18 UTC until 22 UTC.

4.3.3. Comparison to Default Parametrization Framework

First the new parametrization framework (U16) (Ch. 3.2) was tested against the implemented COSMO- ART default framework based on Phillips et al. (2008) (sPDA08). Therefore, the model setup as described above was run once with the U16 framework and once with the sPDA08 scheme.
The cloud occurrence and cloud structure are almost the same in both cases. This is due to the fact that the cloud ice formation is dominated by homogeneous ice nucleation as shown in Figure 4.8. Note that these profiles show the ice number concentration freshly formed in one time step and not the total ice number concentration. The contribution of homogeneous ice nucleation is reduced for the U16 framework only a little in the upper part of the cloud. However, heterogeneously formed ice concentration is much

Table 4.3.: Data sets used to set up the COSMO-ART model for the case study.

input	data set	reference
initial and boundary conditions of trace gas species	MOZART-4	http://www.acom.ucar.edu/wrf-chem/mozart.shtml
anthr. emissions	EDGAR HTAP v 1	http://edgar.jrc.ec.europa.eu/overview.php?v=htap_v1
surface properties	GLC2000 FCOVER HWSD	Konrad Deetz, KIT Karlsruhe/ Germany
dust concentration	ICON- ART	Daniel Rieger, KIT Karlsruhe/ Germany
wildfire emissions	MACC GFAS v 1.1	http://www.gmes-atmosphere.eu/about/project_structure/input_data/d_fire/
meteorological initial and boundary conditions	DWD GME	Heike Vogel, KIT Karlsruhe/ Germany

more increased for the U16 framework across the whole cloud height. This was already expected from the comparison of the INAS density in Chapter 4.1. Figure 4.9 shows for both dust and soot a distinct increase in activated INP when sPDA08 scheme is replaced by the U16 framework. Note that these profiles show the instantaneous INP concentration for one time step, whereas in Figure 4.8 the total concentration is shown. For the U16 framework the activated dust INP concentration is almost 3 orders of magnitude higher than the concentration for the sPDA08 scheme. The activated soot INP concentration is even 4 orders of magnitude higher.
However, homogeneous ice nucleation dominates the ice formation in both model simulations. The sensitivity of homogeneous ice nucleation to aerosol load is discussed and its robustness is tested in sensitivity studies (see Ch. 4.3.5).

4.3.4. Comparison to in-situ Measurements of Clouds and Aerosols

For the following comparison of the measurements and model results, the measurement data sets are averaged between about 18 UTC and 22 UTC excluding take off and landing.
The cirrus cloud started to form in the early afternoon on the 13th April 2011. Figure 4.10 shows the Ice Water Path (IWP) from the model (left) and from GEOS-E

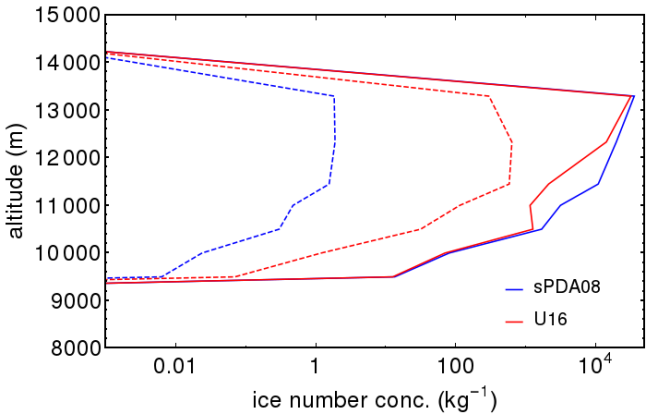

Figure 4.8.: Vertical profile of homogeneous (solid lines) and heterogeneous (dashed lines) ice number concentration freshly formed in one time step. The blue line shows the model results using the sPDA08 framework and the red line the model results using the U16 framework.

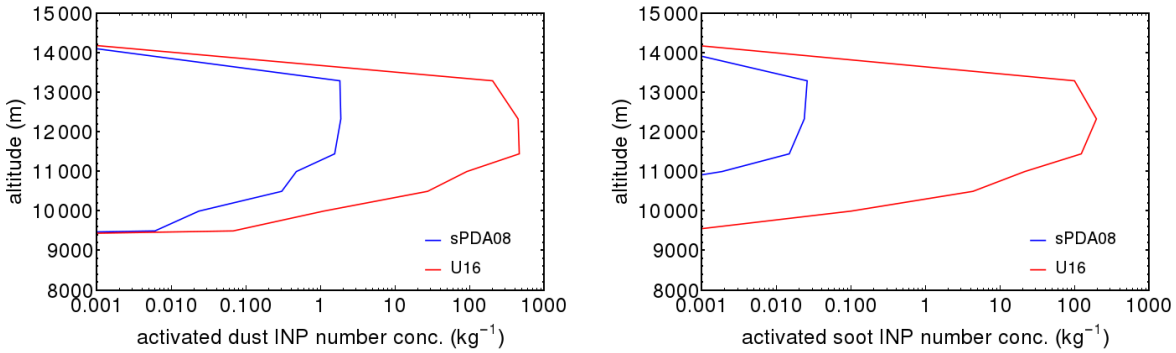

Figure 4.9.: Vertical profiles of heterogeneous ice number concentration (left), dust INP (middle) and soot INP (right). The blue line shows the model results using the sPDA08 framework and the red line shows the model results using the new framework.

observation (right) at about 14 UTC. The cloud patterns especially in and right above the northern edge of Mexico are in good agreement with the observed patterns in the satellite image. However, the value of the IWP from the model is about one order of magnitude smaller than the satellite-derived IWP values.

Therefore, the ice particle size distribution from the model (red line) is compared to the measured ones from VIPS, SID3, 2DS and HVPS (see Fig. 4.11). The measured size distributions are in good agreement with each other. The SID3 instrument showing the highest concentrations may overestimate the concentration of the smaller particles because of shattering effects (Martin Schnaiter, KIT, Karlsruhe/ Germany; personal communication). Also the VIPS instrument may overestimate the size and the concentration due to scratches and impurities on the loop belt collecting the ice particles (Carl Schmitt, NCAR, Boulder/ U.S.; personal communication). Further-

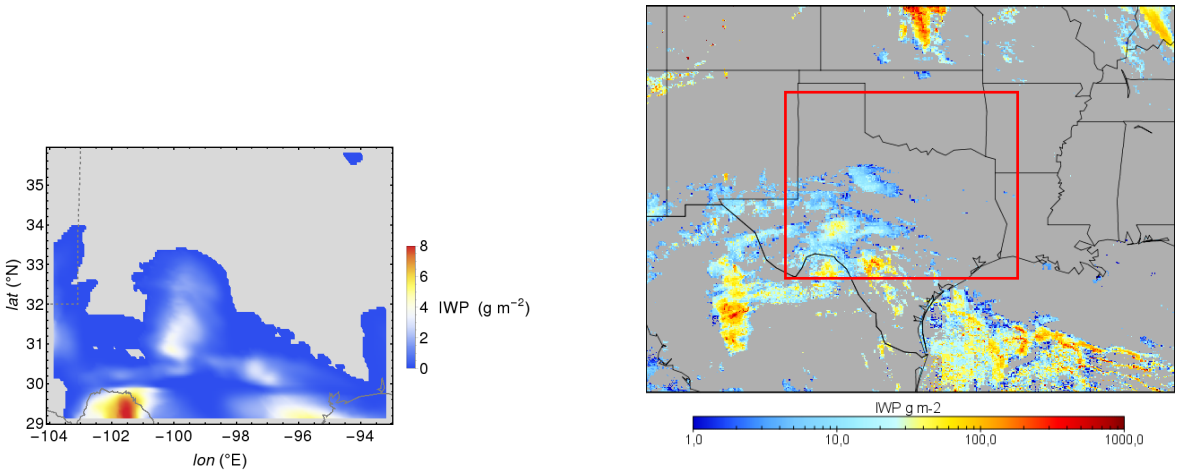

(a) (b)

Figure 4.10.: Ice Water Path (IWP) from the COSMO- ART model at 14 UTC (left) and from GEOS-E satellite observation (data obtained from NASA, 2011) at 13.45 UTC on the 13th April 2011. The red rectangle in the right figure shows the model domain.

more, Jensen et al. (2013) found that the VIPS instruments may overestimates the ice particle concentration for smaller particles in comparison to the 2DS instrument. As suggested by Jensen et al. (2013), the first size bin of the 2DS measurement was omitted. The larger particles detected by the 2DS and HVPS are predominantly bullet rosettes typical for a synoptic cirrus (Lawson et al., 2006a). Note that the measured diameters are not volume- equivalent diameters as given by the model. However, for small ice particles (≤ 100 μm) model and measurements are in reasonable agreement. For the larger ice particles model and measurements disagree. These observed, large ice particles might be formed by heterogeneous ice formation Jensen et al. (2013). If heterogeneous and homogeneous ice formation take place, ice particles will be formed first heterogeneously. These particles will also grow to the largest particles. Therefore, the shown disagreement of the model and the measurement at larger particles sizes can have two possible explanations: (1) the growth of the ice particles in the model is not that efficient as suggested by the observations or (2) the ice particles in the model are formed mainly by homogeneous ice nucleation. The latter reason would be the more probable and is supported by the findings discussed the previous Chapter (see Fig. 4.8) that homogeneous ice nucleation dominates the total ice number concentration.
However, IRP measurements suggest the dominance of heterogeneous ice nucleation (Cziczo et al., 2013). Particles analyzed with the PALMS instrument were sampled with a CVI[10] inlet (Cziczo and Froyd, 2014) enabling the measurement of ice crystals with diameters up to 70 μm. Therewith, PALMS probes particles in the lower range

[10]Counterflow Virtual Impactor

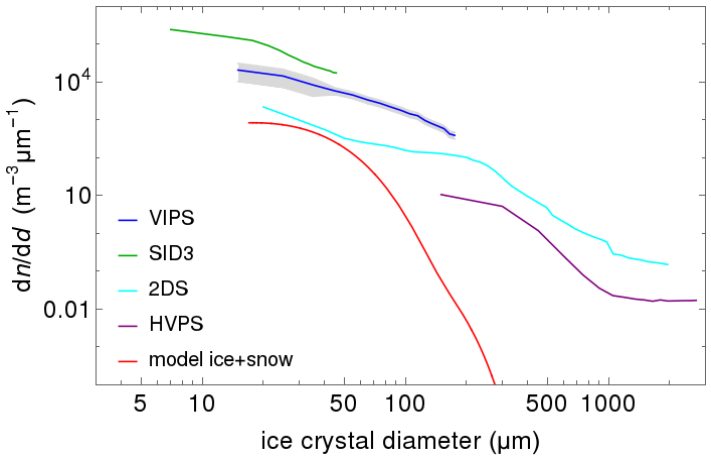

Figure 4.11.: Cloud ice and snow number concentration size distribution from model (red) and aircraft measurements (blue: VIPS, light blue: 2DS, purple: HVPS (data obtained from NASA, 2012b) and green: SID3 (data obtained from Martin Schnaiter, KIT, Karlsruhe/ Germany; personal communication)). The gray shaded area is the given uncertainty for the VIPS particle concentration.

of ice particle sizes. Before the IRP are analyzed with the PALMS instrument, within the CVI inlet interstitial aerosol is rejected and the remaining particles are heated to remove water. The averaged background particle composition (Fig. 4.12(a) right) is compared with the averaged IRP composition (Fig. 4.12(a) left). For overall similar composition and the predominance of sulphate/ organics IRP, the nucleation mechanism is interpreted as homogeneous nucleation, otherwise as heterogeneous nucleation (Cziczo et al., 2013).

On the 13th April 2011 the comparison of both compositions indicated heterogeneous ice nucleation (Daniel Cziczo, MIT, Cambridge/ U.S. and Karl Froyd, NOAA, Boulder/ U.S.; personal communication). The INP concentrations from secondary mixed particles without soot, mineral dust and soot (pure and internally mixed) were averaged between about 8 and 12 km height corresponding to the height range of the aircraft. The secondary mixed particles containing among others sulphate, nitrate and ammonium (see Tab. 4.2) act as homogeneous INP and show the highest contribution to the total ice nucleation. The PALMS measurements found a less distinct contribution of sulphates-organics. Almost half of the probed ice crystals contained mineral dust particles, although mineral dust is not the predominant aerosol particle in the background. The majority of the detected IR mineral dust particles were un- coated (Cziczo et al., 2013). This finding supports the application of the derived parametrization framework for uncoated mineral dust particles in this case study. In the model mineral dust was also the predominant heterogeneous INP (Fig.4.12(a)). The most abundant background aerosol particle class during the measurement campaign was biomass burning presum-

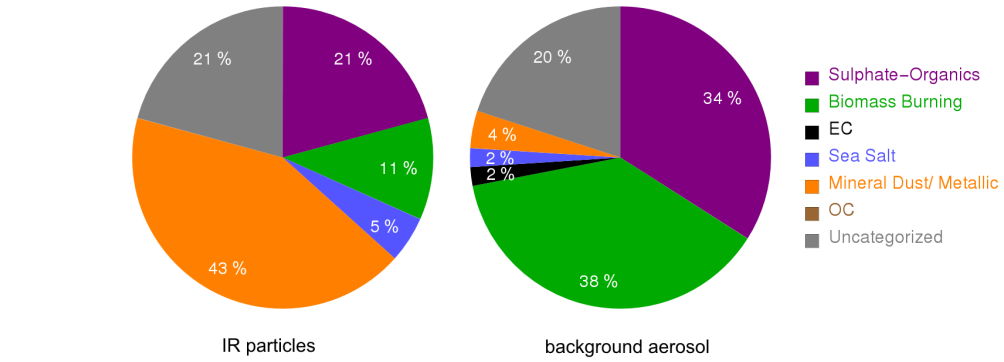

(a)

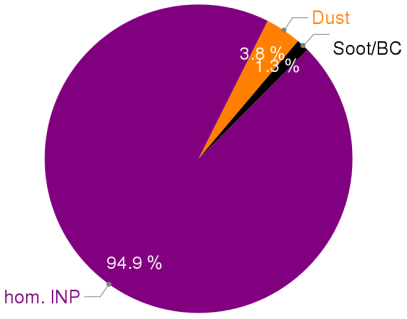

(b)

Figure 4.12.: Composition of the INP from (a) PALMS measurement in-cloud (left) and background (right) (data obtained from Daniel Cziczo, MIT, Cambridge/ U.S. and Karl Froyd, NOAA, Boulder/ U.S.; personal communication) and (b) model.

able from the wildfires in this area. However, only a small fraction of these particles were also present as IRP. In contrast, EC particles were not present as IR particles. In the model a small but significant contribution of soot to ice nucleation was found. The soot in the model includes pure BC as well as internally mixed BC (see Tab. 4.2). Since biomass burning particles are complex mixtures of OC, EC, trace gases and minerals the contribution of soot (especially the internally mixed) to ice nucleation in the model is not unreasonable. Note, mixtures of sulphate and organics, and sea salt may act as INP when present as glasses or anhydrous salts (Cziczo et al., 2013). However, homogeneous ice nucleation of supercooled droplets containing sulphate or sea salts is more likely and therefore, can be interpreted as homogeneous "INP" in the piechart. Furthermore, the class "uncategorized" in the PALMS piecharts includes organic-rich particles or particles of sulphate/ organics/ nitrate mixtures (Cziczo et al., 2013) representing presumably more homogeneous INP than heterogeneous INP.

In summary it can be stated that the observed fraction of homogeneous INP is not negligible compared to the fraction of heterogeneous INP. Nevertheless, the model shows much more homogeneous ice nucleation. The larger amount of homogeneously formed ice in the model compared to the aircraft PALMS measurement has two possible explanations. First, the derived parametrization framework might underestimate the ice nucleation ability of mineral dust and soot particles. However, the desert dust particles

used in the AIDA laboratory experiments represent a realistic mixture of minerals. Therefore, the ability of mineral dust to nucleate ice is assumed to be parametrized realistically. Furthermore, in Chapter 3.2 it was shown that the parametrized OC-poor soot is more ice active than the OC-rich soot. Therewith, the ice nucleation ability of the atmospheric soot is assumed to be rather overestimated than underestimated.

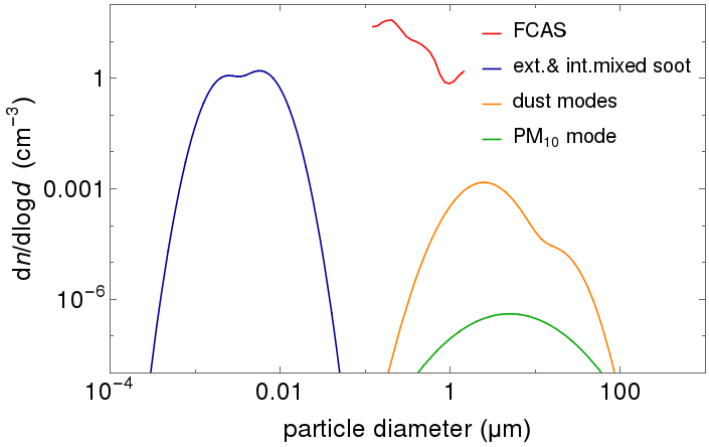

Figure 4.13.: Aerosol number concentration size distribution from FCAS II measurements (red line, data obtained from NASA, 2012b) and model. The black dashed line is the total aerosol size distribution from model, whereas the solid lines indicate the different modes.

The more plausible explanation is that the model may underestimate the aerosol concentration. Figure 4.13 shows the measured (red) and modelled aerosol size distribution. Unfortunately, the NMASS instrument measuring particles with diameters smaller than 0.06 μm was not operated on this day. No instruments were equipped to measure aerosol particles larger than 1 μm. The externally and internally mixed soot modes dominate the total aerosol concentration below 0.05 μm. Above 0.05 μm the dust modes dominate. The concentration of PM_{10} mode appears negligible. Overall an obvious difference between model and in-situ measurement can be observed, although the FCAS measurements cover only a small particle diameter range.
Nevertheless, the total soot number and mass concentration can be validated using the measurements of the SP2 device. Figure 4.14 shows the vertical profile of the soot number concentration and mass mixing ratio (mmr). The number concentration from the model (red lines) is in very good agreement with the SP2 measurement (blue line) assuming an average mass of 2 fg per BC particle (Joshua Schwarz, NOAA, Boulder/ U.S.; personal communication). The modelled mmr (red line) is consistent with the measurement (blue line) up to an altitude of 6 km. Above 6 km the modelled profile shows a sharp decrease up to an height of about 8 km. This reduction is due to the fact that in the simulation, the particles emitted at the ground do not reach this altitudes

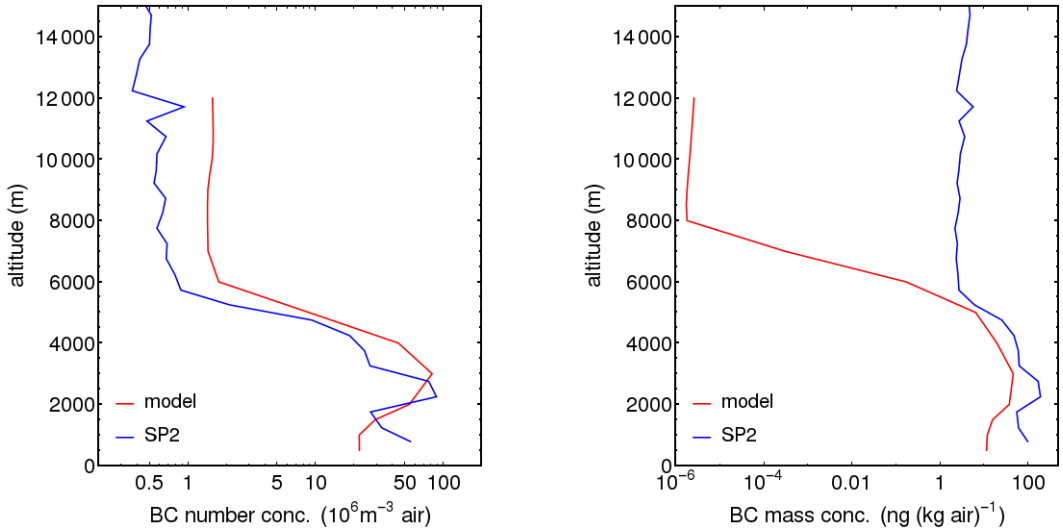

Figure 4.14.: Vertical profile of the soot/ BC (a) number concentration and (b) mass mixing ratio. Blue lines are from SP2 measurement (data obtained from NASA, 2012b). The red lines are from the model simulation and show the externally and internally mixed Accumulation mode soot.

and therefore, the concentrations drop down to their numerical background level, which was set in the model to $0.75 \cdot 10^{-9}\,\mu g\,m^{-3}$. In contrast to the dust, the inflow from long- range transport can not be taken into account for soot, because soot is not yet implemented into ICON- ART. Therefore, no data set of the amount of soot emitted by long- range transport for initializing the model is available. However, the high mmr measured by the SP2 in the upper troposphere is assumed to be due to the wildfires occurring at this time and region of measurement.

Note that the model predicts the total mass of the externally and internally mixed soot particles, whereas the SP2 instrument gives the mass of the BC core for particles of 90 to 600 nm in size. Assuming a coating of the particles, the SP2 instrument detects BC- containing particles in the Accumulation mode size range. Therefore, only the externally mixed soot and the internally mixed soot particles in the Accumulation mode size range are shown in Figure 4.14. However, the model is not able to backtrack the BC core particles in order to determine their original size. Nevertheless, the background soot mass concentration of $0.75 \cdot 10^{-9}\,\mu g\,m^{-3}$ in the model seems to be too small. Observations suggest mass concentration of about minimum 9 orders of magnitude higher (e.g. Petzold et al., 1999; Schaap et al., 2004) than the mass concentration in the ART module. Therefore, in order to obtain a better representation of the soot mass concentration a sensitivity study was set up (see Ch. 4.3.5).

Note that the discrepancy between model and measurements is partly based on the

exceptional weather conditions at the modelled time. The drought and the additional wildfires in the season of the MACPEX campaign caused higher dust and soot/ BC emissions. The long- term inventories of land cover, land use and aerosol/ trace gas emissions driving the model are not necessarily representative for short- term effects during the time of interest.

Figure 4.15 summarizes the modelled mean vertical profiles of aerosol, activated INP and ice number concentration. Note that the shown ice number concentration (turquoise line) as well as the aerosol concentrations are the total concentrations, whereas the INP concentrations and the hom./ het. ice number concentrations showing instantaneous concentrations only from one time step. Homogeneous ice nucleation dominates the

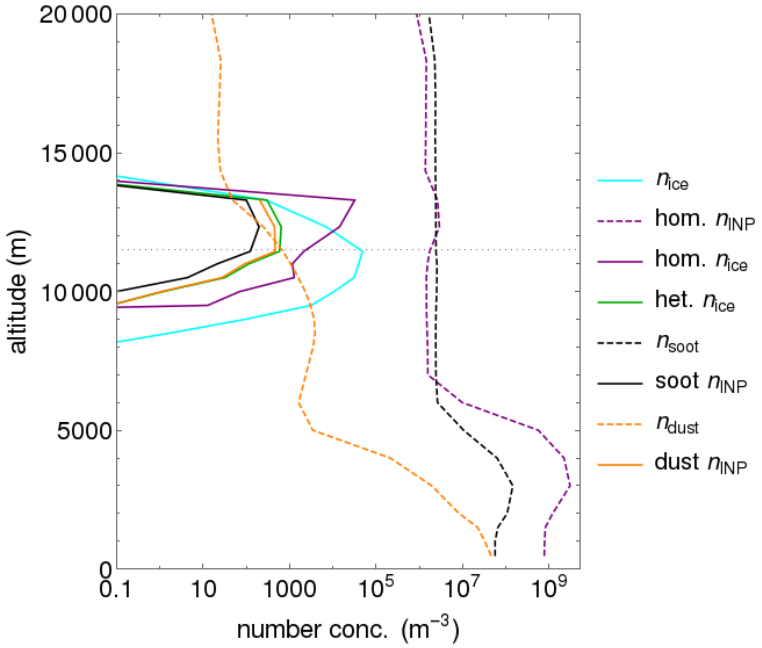

Figure 4.15.: Vertical profiles of aerosol, activated INP and ice number concentration from the model. The turquoise line shows the total ice number concentration, whereas the blue and dashed lines show the concentrations only from one time step.

cloud ice formation. Even though the dust concentration is much smaller than the soot concentration, dust contributes most to heterogeneous ice nucleation. However, the contribution of dust and soot to ice formation is not uniformly distributed neither in the horizontal nor in the vertical (see Fig. 4.16).

Figure 4.16 shows the relative spatial fraction of homogeneously and heterogeneously formed ice calculated via

$$f = \frac{\text{hom. INP} - \text{het. INP}}{\text{hom. INP} + \text{het. INP}} \,. \tag{4.13}$$

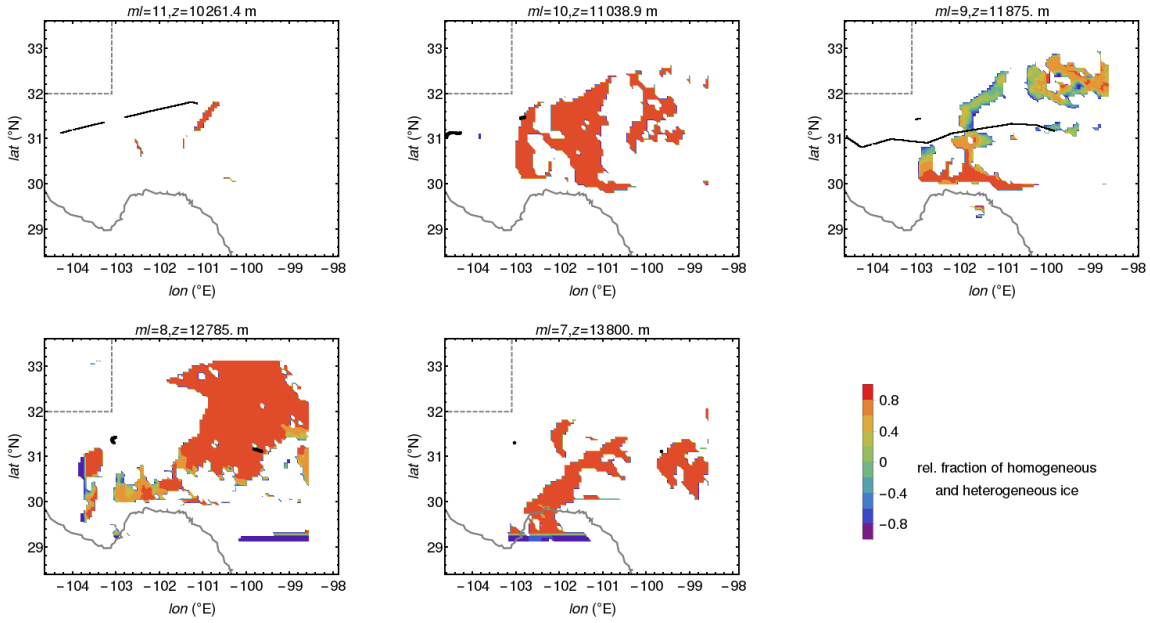

Figure 4.16.: Spatial fraction of homogeneous and heterogeneous ice (Eqn. (4.13)). The black solid line shows the approximated flight path. On the top of the figures, *ml* indicates the model layer number and z the altitude. Note that for model layers 10 and 11 the given altitude is the mean altitude of the domain.

That means, for $f = 1$ (red color) pure homogeneous ice nucleation took place and for $f = -1$ (purple color) pure heterogeneous ice nucleation took place. Only in model layer 9, significant heterogeneous ice nucleation is taking place (see Fig. 4.16). In the layers above the contribution is much smaller and confined to the cloud edges. This finding might be explained by entrainment of dry air and therewith a lower relative humidity wrt. ice which is more favorable to heterogeneous ice nucleation.
Dust INP dominate the simulated heterogeneous ice nucleation across the cloud (see Fig. B.3 in Appendix). However, above about 12 km the soot particles seem to be more contributing to ice nucleation. One simple explanation for this might be the high soot concentration and the decreasing dust concentration in this altitudes in the model (see Fig. 4.15). However, the small dust number concentration compared to the soot number concentration is not in agreement with vertical profiles measured by PALMS/ SP2.
Figure 4.17 summarizes the vertical profiles of the aerosol number concentration. The solid lines show measured profiles from PALMS and SP2, resp., whereas the dashed lines show the modelled profiles. The dashed, purple line shows the profile of the secondary mixed particles without soot contributing to homogeneous ice nucleation. In contrast to the solid line from PALMS measurement, these mixed particles consist of nitrate, ammonium, SOA and primary organics in addition to sulfate (see Tab. 4.2). Assuming that sulfate is the predominant component of this mixture, the profiles are consistent. The concentration of biomass burning particles is comparable to the sulfate.

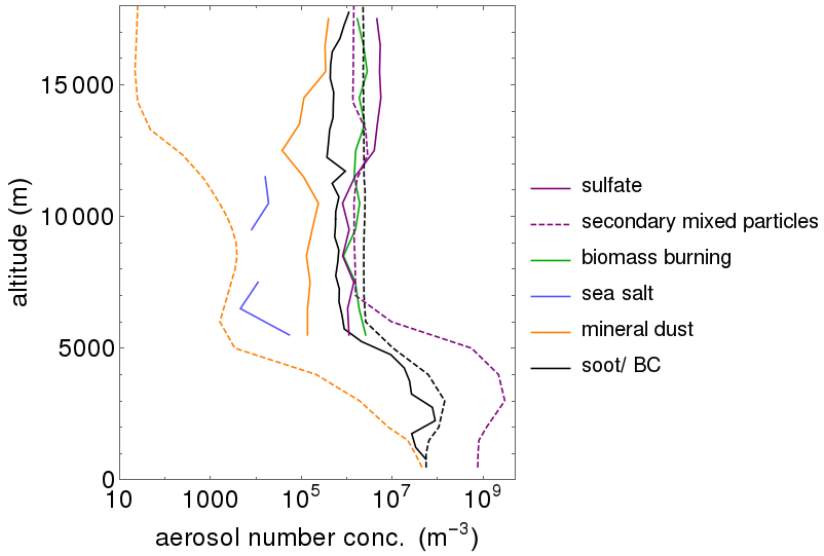

Figure 4.17.: Vertical profile of aerosol from aircraft measurement (solid lines) and model (dashed lines). The profile of BC was evaluated from the SP2 measurement on the 13th April 2011. The other measured profiles were evaluated from the PALMS measurements averaged over the whole campaign (Karl Froyd, NOAA, Boulder/ U.S.; personal communication). The modelled profile of soot contains the externally as well as the internally mixed modes. The dashed purple line indicates the homogeneous INP profile from the model (see Tab. 4.2).

However, in Figure 4.12 it was shown that these particles seem to be not ice active in cirrus altitudes. This is in agreement with laboratory measurements with biomass combustion particle (e.g. DeMott et al., 2009). The worst agreement is found for dust particles. Between 5 km and 12 km height, both dust profiles deviate by a factor of about 100. The profiles of soot number concentration agree very well, whereas the mass mixing ratio is not in agreement, as discussed previously. The last two findings might indicate that the aerosol load in the modelled atmosphere is too small and motivated the sensitivity studies discussed in the following.

4.3.5. Sensitivity Studies

In order to test the sensitivity of the model to more realistic (in this case measured) aerosol concentrations, a number of sensitivity studies were conducted. Table 4.4 gives an overview of the performed sensitivity studies discussed below. The questions to be answered by this studies are: *What is the influence on heterogeneous and homogeneous ice concentration when adjusting the aerosol load to measured vales?* and *Is the resulting INP partitioning in agreement with the measurements?*.

Table 4.4.: Overview of the sensitivity studies.

Number	Adjustment
S1	Increasing the ICON- ART dust mode A number and mass concentration by a factor of 100.
S2	Increasing the pure soot mass concentration background level from $0.75 \cdot 10^{-9}\,\mu g\,m^{-3}$ to $2 \cdot 10^{-3}\,\mu g\,m^{-3}$.
S3	Study combining S1 and S2.
S4	S3, but with reduced INAS density to account for soot with a medium OC content.
S5	S3, but with reduced INAS density to account for soot with a high OC content.

4.3.5.a. Simulation S1

For the first sensitivity study (S1) the smallest dust mode is adjusted in order to match the concentrations given by the PALMS instrument. From Figure 4.17 a deviation between the PALMS measured and the modelled profile by a factor of about 100 was found. The dust concentration is initialized by ICON- ART simulations. Therefore, the number and mass concentrations of the ICON- ART dust mode A are scaled up by a factor of 100 such that the median diameter remains constant. As a first approximation, the data was scaled uniformly over the whole time range, horizontal, and vertical.

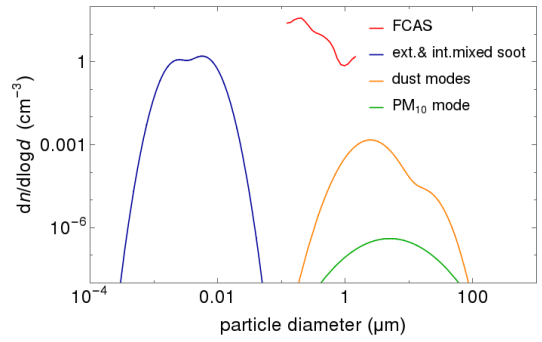

(a) Control Simulation

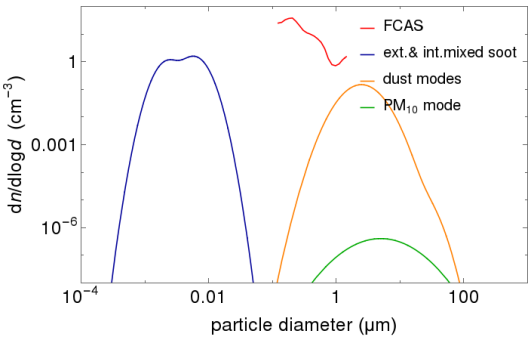

(b) Simulation S1

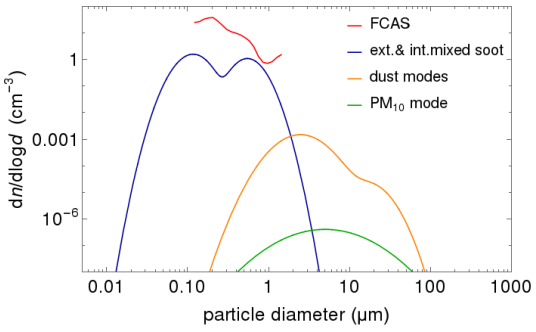

(c) Simulation S2

Figure 4.18.: Aerosol number size distribution (a) from control simulation and (b) with scaling of ICON- ART dust mode A concentration (Simulation S1) and (c) with adjustment of the soot background mass (Simulation S2).

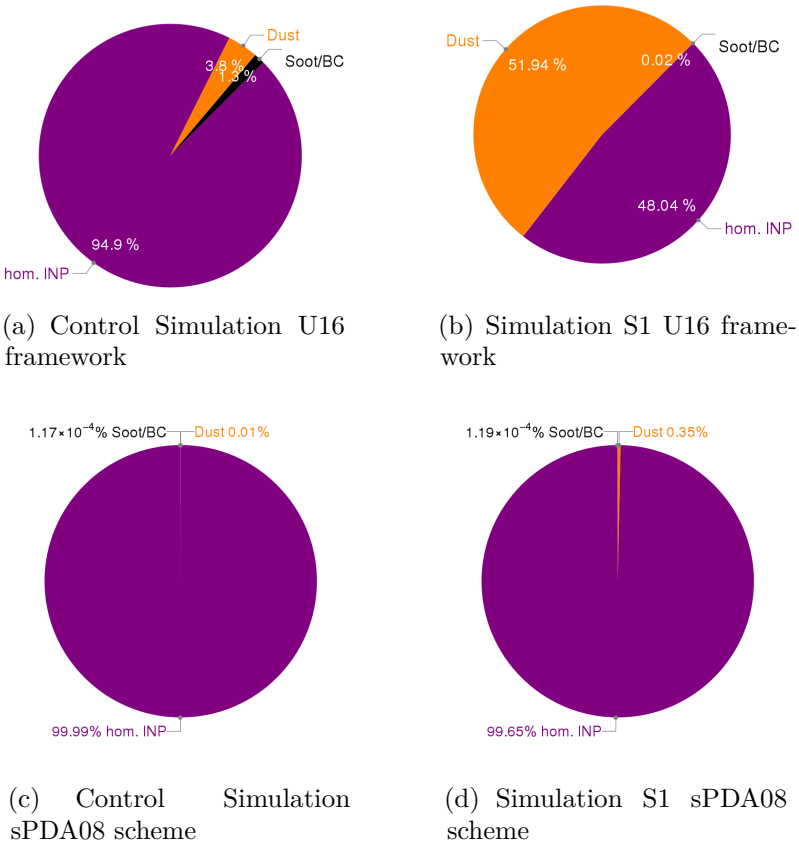

(a) Control Simulation U16 framework

(b) Simulation S1 U16 framework

(c) Control Simulation sPDA08 scheme

(d) Simulation S1 sPDA08 scheme

Figure 4.19.: Contribution of aerosol to ice nucleation using the U16 framework for (a) the control simulation and (b) after scaling of the ICON- ART dust mode A concentration (Simulation S1), and using sPDA08 scheme for (c) control simulation and (d) Simulation S1.

As expected, the scaling of the smallest dust mode by a factor of 100 is also visible in the number size distribution (see Fig. 4.18(b)). Because both number and mass were scaled, the median diameter is kept constant. In comparison to the control simulation the dust modes seem to be in better agreement with the FCAS in-situ measurement. From the increase in dust concentration a higher contribution of dust to ice nucleation is expected.

Figure 4.19(a and b) shows that the activated dust INP number concentration is increased by more than a factor of 10, whereas activated soot INP and homogeneous INP are decreased. This result seems to be in better agreement with the PALMS IR composition shown above. The increase in activated dust INP is even higher for the sPDA08 scheme (Fig. 4.19(c and d)), but the total contribution of dust INP to ice concentration is still insignificant and much less than the contribution shown for the U16 framework. The vertical profiles of the activated INP concentrations (see Fig. B.4(a) in Appendix) indicate that in simulation S1 homogeneous ice nucleation takes place only

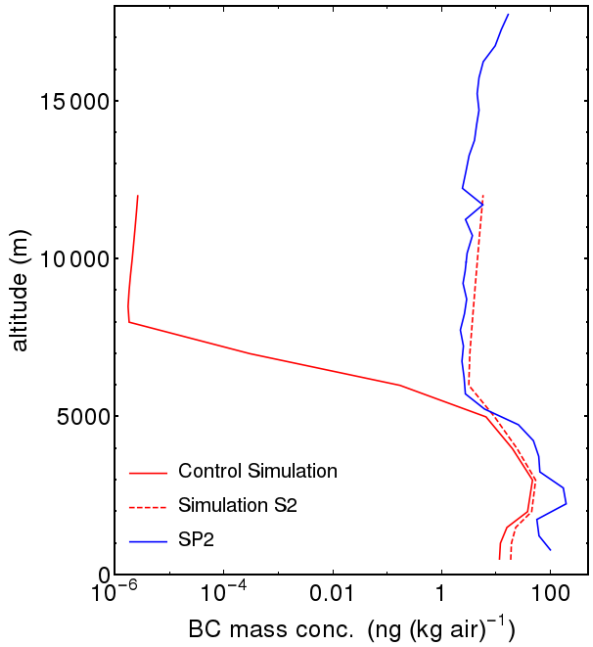

Figure 4.20.: Vertical profile of the accumulation mode soot/ BC mass concentration for control simulation (red line), after adjustment of the soot background mass concentration (red dashed line) and from SP2 measurement (blue line, data obtained from NASA, 2012b).

in the upper part of the cloud. The lower part is clearly formed by heterogeneous ice nucleation on dust particles.

4.3.5.b. Simulation S2

As shown in Figure 4.14, the modelled soot mmr does not agree with SP2 measurements above 6 km. Furthermore, the modelled soot mass concentration seems to decrease down to a background level above 6 km. In the model, the background level of the pure soot mode is set to $10^6\,\mathrm{m}^{-3}$ in number and $0.75 \cdot 10^{-9}\,\mu\mathrm{g\,m}^{-3}$ in mass. This mass concentration background level seems to be too small in this case study. Therefore, in a second sensitivity study (S2), the background soot mass concentration is adjusted to SP2 measurements. Because the modelled number concentration agrees well with the SP2 data, the number concentration background level is not changed but used to adjust the mass concentration background level. Adapting the mean BC core mass of 2 fg from SP2 measurements (Joshua Schwarz, NOAA, Boulder/ U.S.; personal communication), the lower limit of the pure soot mass concentration background level was set to $2 \cdot 10^{-3}\,\mu\mathrm{g\,m}^{-3}$.

The BC mmr after the adjustment agrees much better with the SP2 measurement above 6 km compared to the control simulation (see Fig. 4.20). The increase in soot mass above 6 km also increases the activated soot INP fraction to about 90 % across the whole

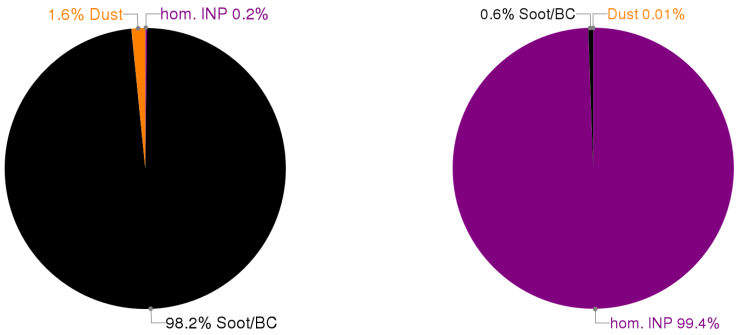

(a) U16 framework (b) sPDA scheme

Figure 4.21.: Contribution of aerosol to ice nucleation after adjusting the soot background mass (Simulation S2) using (a) U16 framework and (b) sPDA08 scheme.

cloud for the U16 framework (Fig. 4.21(a)). As for Simulation S1, homogeneous ice nucleation only takes place in the upper part of the cloud (see Fig. B.4(b) in Appendix) e.g. at higher ice saturation ratio and lower temperature. For the sPDA08 scheme, the increase in activated soot INP is also significant (Fig. 4.21(b)). However, the total contribution of soot to ice nucleation is still low similar to the dust in Simulation S1. This behaviour was already expected from the comparison of the INAS density parametrizations. In Chapter 4.1 the INAS density parametrization for soot particles from the sPDA08 scheme indicated that significant heterogeneous ice nucleation on soot particles takes place for conditions more favorable for homogeneous ice nucleation. Therefore, homogeneous ice nucleation still dominates the ice formation for the sPDA08 scheme, whereas homogeneous ice nucleation is almost inhibited in the case of the U16 framework.

4.3.5.c. Simulation S3

However, the high contribution of soot to ice formation for the U16 framework appears unrealistic. Therefore, a combined simulation (S3) with both adjustments (S1 and S2) was performed.
For the sPDA08 scheme, homogeneous ice nucleation still dominates the ice formation, whereas for the U16 framework homogeneous ice nucleation is almost completely suppressed. Furthermore, homogeneous ice nucleation seems to taking place exclusively in a narrow layer in the middle of the cloud (see Fig. B.4(c) in Appendix). For the U16 framework the contribution of soot to ice formation is damped in comparison to Simulation S2 (Fig. 4.22(a)). However, the contribution of soot to ice formation is still higher than observed. The reason for that could be the higher ice nucleation activity

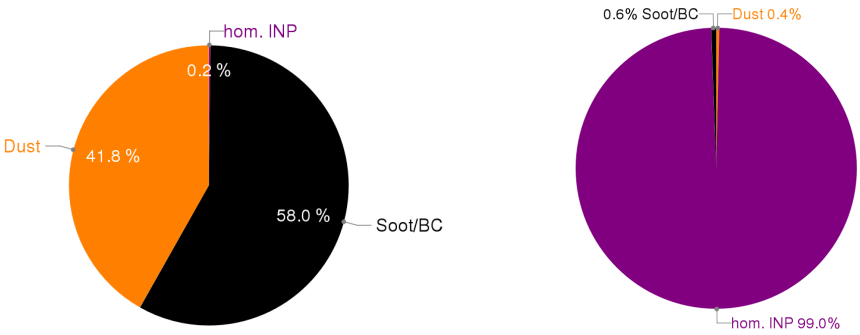

(a) U16 framework (b) sPDA08 framework

Figure 4.22.: Fractions of INP after scaling of the ICON- ART dust mode A and the soot background mass concentration (S3) using the (a) U16 framework and (b) sPDA08 scheme.

of soot in comparison to dust for temperatures above 220 K as discussed in Chapter 3.2.2.c.

The total ice number concentration decreases from about $140\,\mathrm{L}^{-1}$ down to $61\,\mathrm{L}^{-1}$. This lower ice number concentration also indicates the dominance of heterogeneous ice nucleation (Cziczo et al., 2013) and is in better agreement with the measurements of VIPS and 2DS ($67.7\,\mathrm{L}^{-1}$ and $98.7\,\mathrm{L}^{-1}$, resp.)

4.3.5.d. Simulations S4 and S5

From the laboratory studies at the AIDA cloud chamber, a parametrization of the INAS density for soot with a low OC content was found. Soot with a higher OC content showed a weaker activity in comparison. But because of a too small data set for OC-rich soot (see Fig. 3.8(b)) a similar parametrization was not possible. However, from the measurements a scaling factor ξ for the INAS density parametrization function (Eqn. (3.11)) could be estimated:

$$n_S(T, S_i, \text{OC-rich soot}) = \xi\, n_S(T, S_i, \text{soot}) \tag{4.14}$$

$$\text{with } \xi = \begin{cases} 0.2, & \text{medium OC soot} \\ 0.01, & \text{high OC soot} \end{cases}.$$

Therewith, two more simulations were ran with $\xi = 0.2$ (S4) and $\xi = 0.01$ (S5) in order to test the sensitivity of the INP composition to the OC mass content of the soot particles. Hence, more aged and internally mixed soot is simulated. Applying this scaling factor significantly suppresses the contribution of soot INP to primary ice

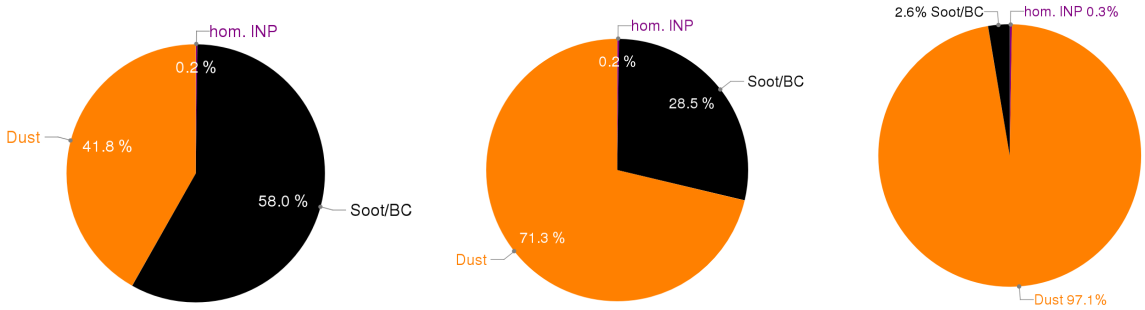

(a) Simulation S3 (b) Simulation S4 $\xi = 0.2$ (c) Simulation S5 $\xi = 0.01$

Figure 4.23.: Fractions of INP for Simulation S3 and for simulations with scaled INAS density functions (S4 and S5).

formation (Fig. 4.23). However, suppressing the ice nucleation activity of the soot does not again increase the fraction of homogeneous INP, but rather the fraction of dust INP. In comparison to Simulation S3, the contribution of soot to heterogeneous ice nucleation for Simulation S5 is in better agreement with observation.

4.3.6. Discussion of the Modelling Results

In previous studies investigating the ice nucleation in cirrus clouds the impact of heterogeneous ice nucleation on cirrus formation was discussed controversial. Some studies proposed the dominance of homogeneous ice nucleation in cirrus altitudes (Gettelman et al., 2010), others found reasonable impact of heterogeneous ice nucleation or even the suppression of homogeneous ice nucleation (e.g. Kärcher et al., 2006; Jensen et al., 2010; Spichtinger and Cziczo, 2010). Studies which found an influence recommended a better representation of the heterogeneous ice nucleation and/ or INP activation spectra (Jensen and Toon, 1997; Spichtinger and Cziczo, 2010). Therefore, the parametrization framework presented in this work was developed in order to investigate the influence of heterogeneous ice nucleation and of different aerosol types.
For the simulations using the U16 framework a depression of homogeneous ice nucleation was observed. In particular, the increase in soot INP yielded to complete suppression of homogeneous ice nucleation. Taking the same amount of soot, but assuming more internally mixed/ aged soot resulted in an INP composition comparable to in-situ measurements. Therefore, the performed sensitivity studies showed that the dominance of homogeneous ice nucleation is mainly due to too low aerosol load in the model and not due to overestimation of homogeneous ice nucleation within the ice nucleation module of the COSMO- ART model (see Ch. 4.1). The strong sensitivity of the nucleation

mechanism on the number of INP was also found in the global model simulations from Barahona et al. (2010). The authors showed that an increase in dust and BC number concentration by a factor of 2 changes the predominant nucleation mechanism from pure homogeneous to pure heterogeneous. Thereby, a BC ice activated fraction of about 1 % is even enough to impact the cirrus formation (Barahona et al., 2010).
In contrast to findings using the U16 framework, the simulations with the default parametrization scheme sPDA08 did not show the suppression of homogeneous ice nucleation, although the sPDA08 was even more sensitive to increased aerosol concentrations compared to the U16 framework. Therefore, this behaviour seems to be not caused by too less INP, but rather by too weak ice nucleation activity of dust and soot aerosol predicted by the sPDA08 scheme. This finding was also noted by Curry and Khvorostyanov (2012).
Because heterogeneous ice nucleation triggers at lower S_i compared to homogeneous ice nucleation, the threshold INP number concentration n_{lim} in the Barahona and Nenes (2009b) scheme depends on the depression of S_i due to heterogeneous ice formation. However, in case of weak heterogeneous ice nucleation (as found for the sPDA08 scheme) the depression of S_i is also very small and hence, the threshold INP concentration n_{lim} would be higher compared to the case with stronger heterogeneous ice nucleation (as found for the U16 framework) (see Barahona and Nenes, 2009b, Eqn. (29)).
Using the Phillips et al. (2008) scheme, Barahona et al. (2010) found that 96 % of the total ice was formed by homogeneous ice nucleation resulting in the highest maximum S_i. These findings are in very good agreement with the results presented in the previous sections. Although the predominant contribution of homogeneous ice nucleation to cirrus ice formation is in agreement with previous modelling studies, the results are in strong disagreement with findings from the measurement campaign MACPEX (Cziczo et al., 2013; Jensen et al., 2013). Furthermore, the high values of s_{max} centered around the homogeneous freezing threshold obtained from the simulation with the sPDA08 scheme (see Fig. B.5 in Appendix) are in strong disagreement with in-situ humidity measurements in cirrus clouds (e.g Cziczo et al., 2013; Krämer et al., 2009).

Barahona et al. (2010) compared the heterogeneous and total ice particle number concentration of different heterogeneous ice nucleation parametrizations. The simulations were performed with a global model using the Barahona and Nenes (2009a,b) microphysics scheme. They found that the Phillips et al. (2008) scheme predicts higher ice particle number concentration compared to the Meyers et al. (1992) scheme and a CNT- based scheme. In contrast to this, the control simulations of the U16 framework and the sPDA08 scheme done in this work predicted similar total ice number concen-

trations ($\approx 140\,\mathrm{L}^{-1}$). This was expected because both simulations were dominated by homogeneous ice nucleation. However, in simulation S3 the total ice number concentration predicted by the U16 framework decreased by nearly one order of magnitude compared to its control simulation. The simulations with sPDA08 scheme did not show this effect. The reduction of the total ice number concentration when heterogeneous ice nucleation is present was also found in previous modelling studies (e.g. Barahona et al., 2010; DeMott et al., 2010).

Modelling studies using multiple types of models and microphysic schemes pointed out the importance of sedimentation (Spichtinger and Cziczo, 2010; Jensen et al., 2013) and updraft velocity (Spice et al., 1999; Barahona and Nenes, 2009a) for the process of heterogeneous ice nucleation. The COSMO- ART model used in this work takes into account both. However, a flaw of the model is that the aerosol concentration is not depleted after INP activation. This might lead to an overestimation of the amount of heterogeneously formed ice (Prenni et al., 2007).

5. Summary

The comprehensive data base from AIDA cloud chamber experiments of the last 11 years was used to develop a parametrization framework for immersion freezing and deposition nucleation. The objective was to parametrize the ice nucleation ability in terms of the Ice Nucleation Active Site (INAS) density for desert dust and soot, and to develop the parametrization in a way extentable to other aerosol types. Also, the INAS density approach developed for immersion freezing was extended to deposition nucleation.

The previous AIDA data evaluation for calculating the INAS densities was improved by two extensions. The first accounts for incomplete CCN activation of the aerosol, which leads to a reduced aerosol surface area active in the immersion freezing mode during the cloud expansion experiment. The second corrects for the reduction of the total aerosol surface area immersed in the droplets due to the ongoing droplet freezing in the course of an experiment. Because of these reductions of the aerosol surface area, the INAS densities slightly increase compared to previously derived INAS densities.

In case of immersion freezing on desert dust samples collected from the ground in desert dust areas, and samples collected from the surface after transport through the atmosphere and deposition on the ground were used. Although the transport might modify the ice nucleation ability by e.g. chemical coating, no significant deviation in the ice nucleation ability of both desert dust samples was observed. Furthermore, an exponential relation of the INAS density and the temperature was found and the derived parametrization line represents immersion freezing of both freshly emitted and transported desert dust. This parametrization is in good agreement with the earlier study of Niemand et al. (2012) which used the same samples as this work.

For immersion freezing on soot, a graphite rich soot and a combustion soot with a low organic carbon content were used. Heterogeneous ice nucleation could only be observed during three out of nine experiments and only close to the detection limit of the optical particle counter. Further cooling caused the supercooled droplets to freeze homogeneously at a temperature of about 238 K. Because of the weak ice nucleation ability, upper limit INAS densities were calculated by assuming the presence of five ice particles during the time period when supercooled droplets were present. The existing

parametrization line derived by Murray et al. (2012) was scaled to the obtained upper limit INAS densities. This parametrization is in good agreement with the recently published parametrization line of Schill et al. (2016), but deviates by 3 orders of magnitude from previous studies.
For deposition nucleation on desert dust the same samples were used as for the immersion freezing experiments. In contrast to the immersion freezing experiments, the desert dusts collected after atmospheric transport showed a somewhat higher deposition ice nucleation activity than the other samples. The reason for this tendency is unclear. For deposition nucleation on soot combustion soot with a higher organic carbon content was used next to the graphite rich and low organic carbon combustion soot. Ice nucleation was observed at higher ice saturation ratios for the samples with a high organic carbon content compared to samples with a low organic carbon content ($<$20 wt %).
In the deposition nucleation mode, u- shaped isolines of INAS density were found for both soot and desert dust. Therewith, ice nucleation below water saturation and temperatures below 240 K can be split into three subregimes. At warmer temperatures, the INAS density isolines show a positive slope with a strong temperature dependency maybe explainable with the pore condensation and freezing mechanism. Thereby, the slope of the soot INAS density isolines is much steeper than for the desert dust. The reason for this is unclear but might be explained by the differences in the pore structure. At colder temperatures, the INAS density isolines show a negative slope as described by the classical deposition nucleation theory. In the transition regime connecting both regimes, ice nucleation is determined by ice saturation ratio alone.

In comparison to other parametrization frameworks based on CNT or empirical studies, the framework presented in this work has the benefit of a small set of input parameters. Therewith, the framework can be implemented into models more easily. The comparison of the new framework with a CNT- based framework and an empirical framework showed large differences in INAS densities especially below water saturation and therewith the number of ice nucleating particles when applied in models.
The developed parametrization framework was implemented into the limited- area model COSMO- ART. Within a case study of a synoptically driven cirrus cloud the model results were compared to aircraft measurements conducted at the time and the location of the case study. At first, the new framework was tested against the default implemented scheme and showed an increase in heterogeneously formed ice. In comparison to the aircraft measurements a strong disagreement to the ice residual particle composition was found, because the modelled aerosol number concentration was found to be several orders of magnitude smaller than the measured concentrations. As a consequence,

the model predicted much more homogeneous ice nucleation than measured by the PALMS instrument. However, the new framework as well as the default parametrization scheme and the PALMS measurement suggested mineral dust to be the predominant heterogeneous ice nucleating particle.

The disagreements between model and in-situ measurement gave rise to perform some sensitivity studies to test the influence of higher aerosol concentration in the model atmosphere. It was found that the increase in soot background mass concentration as well as the increase in dust concentration yielded to a aerosol size distribution better agreeing with the measurements. Furthermore, using the new framework homogeneous ice nucleation was almost suppressed as suggested by the aircraft measurements. In contrast, the default parametrization scheme in the model still predicted the dominance of homogeneous ice nucleation.

6. Outlook

The developed parametrization framework covers the two major atmospheric aerosol types, desert dust and soot, with a potentially high contribution to the abundance of atmospheric ice nucleation particles (INPs) (Cziczo et al., 2013; Stier et al., 2005). Furthermore, the framework is applicable for immersion freezing and deposition nucleation. The developed parametrization framework was successfully tested for high aerosol concentrations and cirrus cloud conditions. In order to validate the applicability of the framework at other conditions further tests in other regions, for other cloud types (e.g. mixed-phase clouds) and different aerosol loadings should be performed and compared to field measurements (aircraft and ground-based). Since the long-range transport of aerosol was not well represented in the shown case study, the model simulations have to be repeated either by using more global model results as done for dust or by nesting e.g. using the new global model ICON-ART. Thereby, the contribution of heterogeneous ice nucleation should be compared to other recent heterogeneous ice nucleation parametrizations (e.g. DeMott et al., 2015; Savre and Ekman, 2015; Phillips et al., 2013) next to Phillips et al. (2008) scheme.
For the use in models the range of validity of the parametrizations has to be maximum. Therefore, experiments on desert dust in immersion freezing mode at temperatures below 245 K down to the homogeneous freezing temperature and above 255 K have to be conducted to corroborate the parametrization. Especially for temperatures above 250 K, experiments with desert dust are needed since the observed differences to soil dust are explained by organic matter (Tobo et al., 2014) being ice active at higher temperatures. Below water saturation, recent AIDA measurements with desert dust samples at cold cirrus temperatures will corroborate the parametrization for deposition nucleation on desert dust.
Since the contribution of soot to ice formation in clouds is still controversial more experiments on soot particles have to be performed. As suggested by Crawford et al. (e.g. 2011); Möhler et al. (e.g. 2005b) and also found in this work, the OC content of the soot strongly influences the ice nucleation efficiency. Therefore, (1) more experiments with OC-rich soot has to be conducted in order to quantify the de-activation and (2) experiments with atmospherically more relevant soot aerosol particles e.g. traffic

and industrial soot or biomass burning exhaust have to be done. The latter is also of interest in models since emission inventories driving the models provide emission data sets especially for these aerosol types.

The developed parametrizations are limited to uncoated aerosol particles, although many aerosols are transported for long distances and therewith possibly coated before contributing to ice formation. Möhler et al. (2005a) found that below water saturation soot coated with sulphuric acid is less ice active than uncoated soot. This was also found for sulphuric acid and SOA coated mineral dusts (Cziczo et al., 2009; Möhler et al., 2008). A quantification of the influence of coating on the ice nucleation efficiency (e.g. in terms of a scaling factor as introduced in this work or an independent parametrization) again would be useful for model applications. Therefore, an ongoing work analyzes the effect of atmospheric coating on the ice nucleation activity of dust samples. This analyses points out the need for more AIDA experiments on coated aerosol particles in both immersion freezing mode and deposition nucleation mode.

One objective of the parametrization framework developed in this work was the possibility to extent this framework to other aerosol types. In the last 11 years, several experiments with other atmospherically relevant aerosols like organics, sea salt or biological materials were done and could be used to extend the parametrization framework. This extension would also be of interest in further modelling studies, since the IRP measurements suggested a contribution of sea salt particles and biological materials to ice formation (Cziczo et al., 2013; Pratt et al., 2009).

A. Additional Tables

Table A.1.: Conditions for immersion freezing experiments with desert dust where no freezing was observed. $n_{ae,0}$ is the initial aerosol number concentration measured by the CPC and $s_{ae,0}$ is the initial aerosol surface area concentration. $T_{droplet}$ is the temperature at start of droplet formation and T_{stop} the temperature the expansion stopped.
Previously published experiments are labeled with N12 (Niemand et al. (2012)) and C09 (Connolly et al. (2009)).

Campaign	Exp Number	Date	Aerosol	$n_{ae,0}$ (cm^{-3})	$s_{ae,0}$ ($\mu m^2\,cm^{-3}$)	$T_{droplet}$ (K)	T_{stop} (K)	published
ACI04	2	28 Sept 2010	SD4	120.00	31.33	262.3	256.4	-
ACI04	4	29 Sept 2010	SD4	127.76	202.03	262.1	256.1	N12
ACI04	13	01 Oct 2010	AD2	173.26	172.84	260.8	258.6	N12
IN04	1	15 Sept 2003	SD2	124.75	n/a	278.3	271.4	C09
IN04	3	16 Sept 2003	SD2	87.33	17.54	275.8	268.3	C09
IN04	15	23 Sept 2003	AD1	249.67	687.41	275.1	267.4	C09
IN04	17	23 Sept 2003	SD1	165.33	n/a	270.3	265.3	-
IN05	40	10 Nov 2004	SD2	120.84	68.17	274.5	267.8	C09
IN05	45	12 Nov 2004	AD1	227.09	158.74	266.9	260.8	C09
IN05	46	12 Nov 2004	AD1	125.98	347.35	266.7	260.5	C09
IN05	47	12 Nov 2004	AD1	421.72	315.67	266.0	260.7	C09
IN05	48	15 Nov 2004	AD1	149.36	67.56	261.1	254.1	C09

B. Additional Figures

HYSPLIT Trajectories

NOAA HYSPLIT model forward trajectories to show the inflow of biomass burning particles from wildfires into the model domain. The approximate position of the shown wildfires (labeled by the star) was taken from NASA FIRMS Fire Mapper based on MODIS measurements (NASA FIRMS (2012)).

Because of the south- western flow, wildfire emissions from northern Mexico were

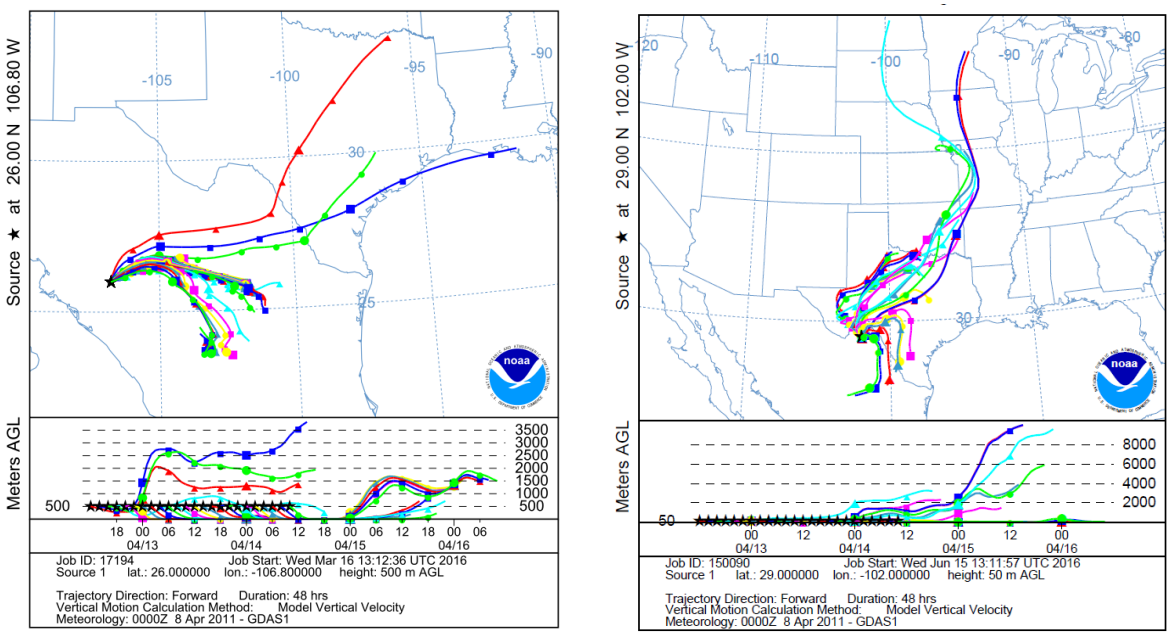

(a) (b)

Figure B.1.: HYSPLIT forward trajectories started on 12th April 2011 12 UTC at (a) 26° N, −106.8° E and 2980 m ASL and (b) 29° N, −102° E and 1364 m ASL.

transported into the model domain. Local wildfire emissions were distributed over the whole model domain and reach altitudes of up to 8 km.

ICON-ART Dust Number Concentrations

In addition to Figure 4.7 showing the dust mode C mass concentration, dust mode A and B mass concentrations are presented here.

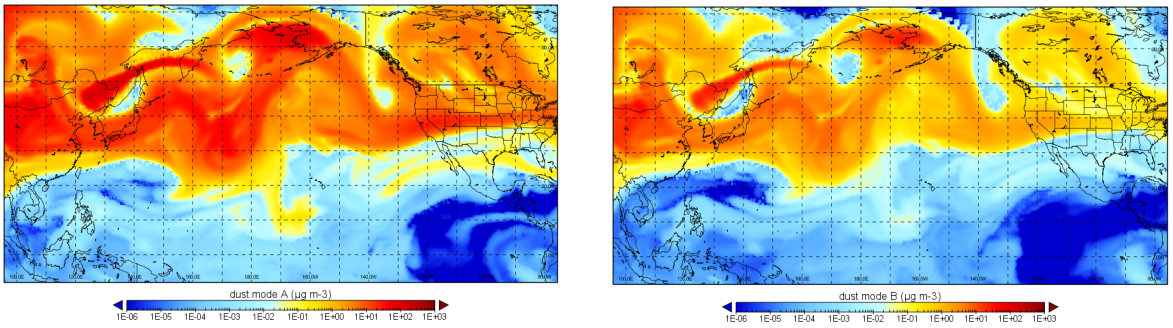

(a) dust mode A (b) dust mode B

Figure B.2.: Dust mode (a) A and (b) B at 8 km height on 13th April 2011 at 12 UTC simulated with ICON-ART.

Spatial Distribution of Soot-to-Dust INP Fraction

In addition to Figure 4.16 showing the fraction of homogeneous and heterogeneous INP on different model layers, the following figure adds the fraction of dust and soot INP on the same model layers.

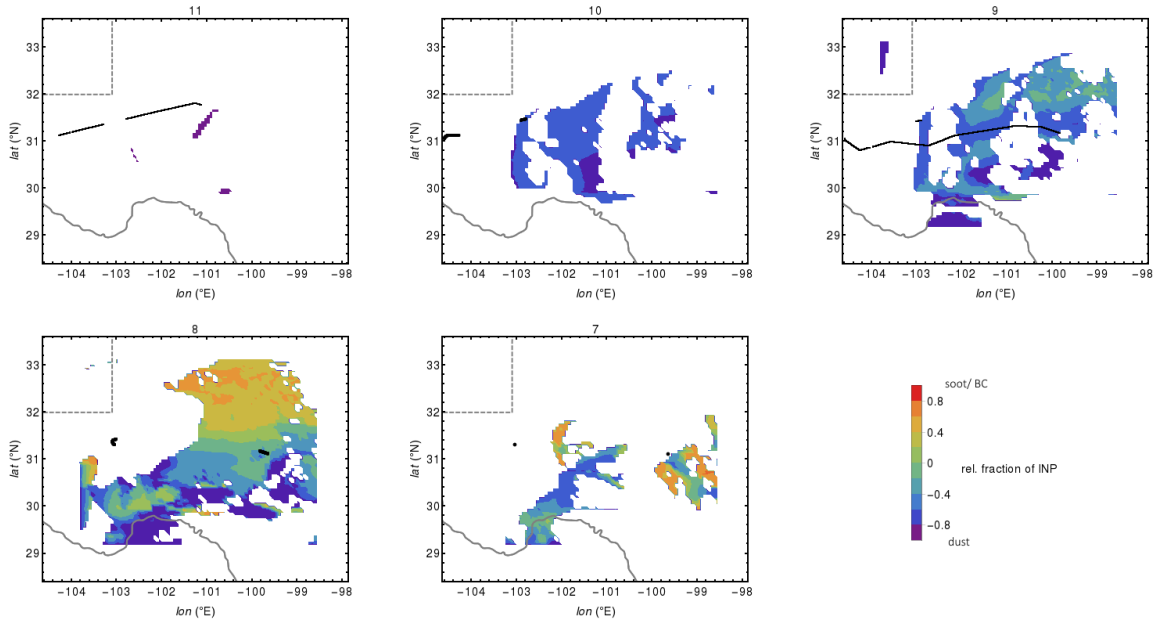

Figure B.3.: Spatial fraction of soot and dust INP. Black solid line is the approximated flight path. Small number above the single figures are the model layers from bottom to top.

Vertical Profiles of Ice Number Concentration, Activated INP Concentration and Aerosol Concentration for the Sensitivity Studies

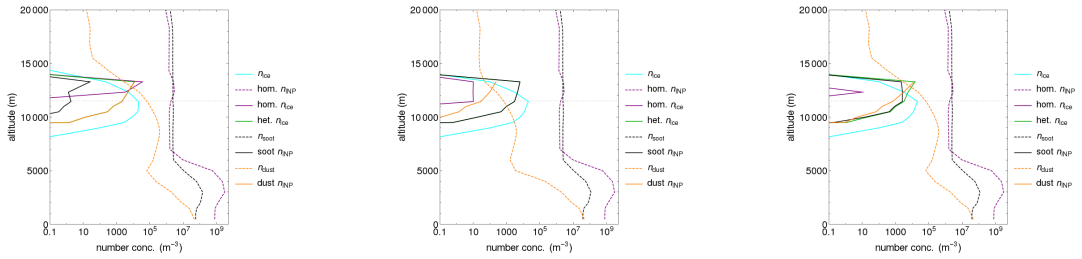

(a) Simulation S1 (b) Simulation S2 (c) Simulation S3

Figure B.4.: Vertical profiles of aerosol, INP and ice number concentration for (a) Simulation S1, (b) Simulation S2 and (c) Simulation S3 obtained from model simulation with the U16 framework.

Probability Distribution of Ice Saturation Ratio

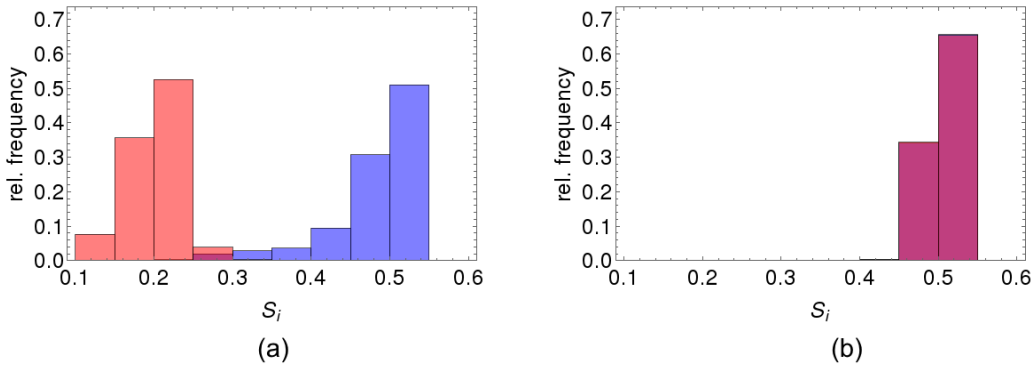

Figure B.5.: Relative frequency of S_i during heterogeneous ice formation from simulations using the (a) U16 framework and (b) sPDA08 scheme. The bluish bars show the control simulation and the reddish bars Simulation S3.

Note that the bars in Figure B.5 are shown overlapped. That means that in Figure B.5(b) the bars for both simulation are almost equal, whereas in (a) a distinct shift to lower S_i can be observed for Simulation S3.

C. Correction of the Aerosol Surface Area Concentration

C.1. Reduction due to incomplete CCN activation

As for some immersion freezing experiments in the AIDA cloud chamber not all aerosol particles are activated to droplets, the aerosol surface area available for freezing is not equal to the total surface area. Therefore, the total aerosol surface area has to be reduced by the part which was not activated to droplets. Assuming that the largest aerosol particles in the distribution activate first, then the CCN activated part of the total aerosol size distribution is given by

$$s_{ae} = \frac{1}{\sqrt{2\,\pi}} \int_{\ln d_{p,min}}^{\infty} \mathrm{d} \ln d_p \, \frac{s_{ae,0}}{\ln \sigma_g, s} \, \exp\left(-\frac{\left(\ln d_p - \ln \overline{d}_{p,s} \right)^2}{2 \, \ln^2 \sigma_{g,s}} \right) . \tag{C.1}$$

The total aerosol surface area concentration $s_{ae,0}$, and the appropriate median diameter $\overline{d}_{p,s}$ and geometric standard deviation $\sigma_{g,s}$ are obtained from the fit shown in Figure **??**. Therefore, $d_{p,min}$ is that aerosol particle diameter down to which the aerosol was activated to CCN. However, because equation C.1 includes two unknown variables ($d_{p,min}$ and s_{ae}), a second equation is needed. From the measurements the CCN activated fraction f_d can be calculated. Hence, the number size distribution of the CCN activated part of the aerosol size distribution is given by

$$f_d = \frac{n_d}{n_{ae,0}} = \frac{1}{\sqrt{2\,\pi}} \int_{\ln d_{p,min}}^{\infty} \mathrm{d} \ln d_p \, \frac{1}{\ln \sigma_{g,n}} \, \exp\left(-\frac{\left(\ln d_p - \ln \overline{d}_{p,n} \right)^2}{2 \, \ln^2 \sigma_{g,n}} \right) . \tag{C.2}$$

Where n_d is the droplet number concentration, $n_{ae,0}$ the total aerosol number concentration, and $\overline{d}_{p,n}$ and $\sigma_{g,n}$ the appropriate median diameter and geometric standard deviation obtained from the fit. Note, that the median diameter and geometric standard deviation are different from the surface area size distribution, because they are determined by two independent fit functions. By substituting the term in the exponential

function, the above equation reduces to the standard normal distribution function $\Phi(x_{min})$ with cutoff value x_{min}.

$$1 - f_d = \frac{1}{\sqrt{2\,\pi}} \int_{-\infty}^{x_{min}} \mathrm{d}x \, \exp\left(-\frac{x^2}{2}\right) \tag{C.3}$$

$$\text{with} \qquad x := \frac{\ln d - \ln \overline{d}_{p,n}}{\ln \sigma_{g,n}}$$

Using standard mathematics programs (e.g. MatLab, IDL), the cutoff value x_{min} can be determined and therewith the minimum diameter for INP activation can be recalculated by

$$d_{p,min} = \overline{d}_{p,n} \, \exp\left(x_{min} \, \ln \sigma_{g,n}\right) \; . \tag{C.4}$$

By applying this diameter in Equation C.1 and substituting the term in the exponential function in Equation C.1 analogous, the CCN activated aerosol surface area concentration available for INP activation is given by the following equation.

$$s_{ae} = s_{ae,0} \left(1 - \Phi\left(\frac{\ln d_{p,min} - \ln \overline{d}_{p,s}}{\ln \sigma_{g,s}}\right)\right) \tag{C.5}$$

C.2. Correction due to IN activation

In Section 3.1.3 the splitting of the ice nucleation interval in bins k was described. During each bin k a certain number of aerosol particles activate to ice crystals and therefore, is not available for further INP activation. Hence, the total aerosol surface area concentration has to be reduced after each bin k depending on the ice activated fraction f_i. Assuming that the largest aerosol particles activate first, the non- activated part of the total aerosol surface area size distribution in bin $k-1$ $s_{ae,k}$, which is available for ice nucleation in bin k is given by

$$s_{ae,k} = \frac{1}{\sqrt{2\,\pi}} \int_{-\infty}^{\ln d_{p,act,k-1}} \mathrm{d} \ln d_p \, \frac{s_{ae,0}}{\ln \sigma_{g,s}} \, \exp\left(-\frac{\left(\ln d_p - \ln \overline{d}_{p,s}\right)^2}{2 \, \ln^2 \sigma_{g,s}}\right) \; . \tag{C.6}$$

Where $s_{ae,0}$ is the total aerosol surface area concentration (if necessary, reduced due to incomplete CCN activation, Ch. C.1) obtained from the fit to the measured size distribution, and $\overline{d}_{p,s}$ and $\sigma_{g,s}$ the appropriate median diameter and geometric standard deviation, resp. However, because equation C.6 includes two unknown variables ($d_{p,act,k-1}$ and $s_{ae,k}$), a second equation is needed. From the measurements the INP activated

fraction f_i can be calculated. Hence, the number size distribution of the non- activated part of the aerosol size distribution is given by

$$1 - f_{i,k-1} = 1 - \frac{n_{i,k-1}}{n_{ae,0}} = \frac{1}{\sqrt{2\,\pi}} \int_{-\infty}^{\ln d_{p,act,k-1}} \mathrm{d} \ln d_p \, \frac{1}{\ln \sigma_{g,n}} \, \exp\left(-\frac{\left(\ln d_p - \ln \overline{d}_{p,n} \right)^2}{2 \, \ln^2 \sigma_{g,n}} \right) . \tag{C.7}$$

Where $n_{i,k-1}$ is the ice number concentration in bin $k-1$, $n_{ae,0}$ the total aerosol number concentration, and $\overline{d}_{p,n}$ and $\sigma_{g,n}$ the appropriate median diameter and geometric standard deviation obtained from the fit. Note, that the median diameter and geometric standard deviation are different from the surface area size distribution, because they are determined by two independent fit functions. By substituting the term in the exponential function, the above equation reduces to the standard normal distribution function $\Phi(x_{act,k-1})$ with cutoff value $x_{act,k-1}$. Using standard mathematics programs, $x_{act,k-1}$ can be calculated and the appropriate activation diameter for bin $k-1$ can be recalculated.

$$d_{p,act,k-1} = \overline{d}_{p,n} \, \exp\left(x_{act,k-1} \ln \sigma_{g,n} \right) \tag{C.8}$$

Applied in Equation (C.6), the available aerosol surface area concentration in bin k additionally corrected for dilution is given by

$$s_{ae,k} = s_{ae,0} \, \frac{p_k}{p_0} \Phi \left(\frac{\ln d_{p,act,k-1} - \ln \overline{d}_{p,s}}{\ln \sigma_{g,s}} \right) . \tag{C.9}$$

Note that $s_{ae,0}$ has to be corrected for incomplete CCN activation as described in the previous section.

List of Symbols and Abbreviations

Table C.1.: List and description of the symbols.

Symbol	Description
A	kinetic prefactor in CNT
d_i^*	diameter threshold for separating ice from cloud droplets/ aerosol particles
$d_{p,act,k-1}$	INP activation aerosol diameter for time bin $k-1$ in μm
$\overline{d}_p$	median diameter of the aerosol size distribution in μm
$d_{p,min}$	CCN activation aerosol diameter in μm
d_p	particle diameter, depending on the context particle means aerosol or ice
ΔG^*	maximum of difference in Gibbs Free energy before and after phase transition
Δg_{act}	energy barrier for liquid to ice phase transition
$e_{s,X}$	saturation vapor pressure wrt water or ice ($X = w, i$)
f	form factor
f_d/ f_i	CCN and ice activated fraction, resp.
f_N, f_S, f_V	particle number/ surface area and volume size distribution
j	ice nucleation rate in $\mathrm{m}^{-2}\,\mathrm{s}^{-1}$
k	index time bin
$k(T)$	number of activated INP per unit aerosol surface and unit temperature interval
k_B	Boltzmann constant ($1.381 \cdot 10^{-23}\,\mathrm{J\,K}^{-1}$)
l	index of particle size category
m_p	particle mass concentration, depending on the context particle means aerosol or ice
μ	shape factor for generalized Gamma distribution
μ_k^l	k-th moment of size category l
n_{ae}, $n_{ae,0}$	aerosol number concentration and n_{ae} measured by CPC at begin expansion in cm^{-3}

Table C.1 Continued:

n_{het}	number concentration of heterogeneously nucleated ice
n_{hom}	number concentration of homogeneously nucleated ice
n_i	ice particle number concentration
n_{ice}	modelled ice crystal number concentration in m^{-3}
n_{INP}	number concentration of ice nucleating particles in m^{-3}
N_p	particle number, depending on the context particle means aerosol or ice
n_p	particle number concentration, depending on the context particle means aerosol or ice
n_S	Ice Nucleating Active surface Site (INAS) density in m^{-2}
$n_{S,k}$, $n_{S,start}$	n_S for time bin k and the first time bin
$n_{S,max}$	upper limit n_S for soot immersion freezing
ν	shape factor for generalized Gamma distribution
p_k, p_0	chamber pressure for time bin k and at start of expansion in hPa
$\Phi(z)$	standard normal distribution function with cutoff value z
S_{ae}	aerosol surface area
s_{ae}	aerosol surface area concentration
$s_{ae,0}$, $s_{ae,k}$	aerosol surface area concentration at begin expansion and for each time bin in $\mu m^2 cm^{-3}$
S_i	ice saturation ratio
$S_{i,k}$, $S_{i,start}$	ice saturation ratio for time bin k and the first time bin
s_{max}	maximum ice saturation wrt. ice (Barahona and Nenes, 2009b)
s_{hom}	threshold ice saturation wrt. ice for homogeneous ice nucleation
σ_g	geometric standard deviation
T	temperature in K
T_k, T_{start}	temperature for time bin k and for the first time bin in K
$T_{droplet}$	temperature at start of droplet formation in K
T_{max}	temperature for upper limit n_S
T_{stop}	temperature at stop of expansion in K
θ	contact angle between particle surface and droplet
v_l	volume of a molecule in the liquid phase
α, β, γ, κ, λ	fit values for INAS density parametrization in deposition nucleation mode

Table C.2.: List and description of the abbreviations. Abbreviations of the desert dust samples can be found in Table 3.1.

Abbreviation	Description
AIDA	Aerosol Interaction and Dynamics in the Atmosphere
APS	Aerodynamic Particle Sizer
ART	Aerosol and Reactive Trace gases
BC	Black Carbon
BET	Brunauer-Emmett-Teller (method to measure the surface area of particles via gas adsorption)
(m)CAST	(miniature) Combustion Aerosol STandard
CCN	Cloud Condensation Nuclei
COSMO	COnsortium for Small- scale MOdelling
CNT	Classical Nucleation Theory
CPC	Condensation Particle Counter
EC	Elemental Carbon
FCAS	Focused Cavity Aerosol Spectrometer
GSG	Graphite Spark Generator
HVPS	High Volume Precipitation Spectrometer
HWV	Harvard Water Vapor
ICON	ICOsahedral Nonhydrostatic
INAS (density)	Ice Nucleation Active Site (density)
INP	Ice Nucleating Particle
IR/ IRP	ice residual and ice residual particle, resp.
IWP	Ice Water Path
MACPEX	Mid-latitude Airborne Cirrus Properties EXperiment
mmr	mass mixing ratio
NMASS	Nuclei-Mode Aerosol Size Spectrometer
OC	Organic Carbon
PAH	Polycyclic Aromatic Hydrocarbon
PALMS	Particle Analysis by Laser Mass Spectrometry
PCF	Pore Condensation and Freezing
PDF	Probability Density Function
PSD	Particle size Distribution
RBG	Rotating Brush Generator
SID	Small Ice Detector
SMPS	Scanning Mobility Particle Sizer

Table C.2 Continued:

SP2	Single Particle Soot Photometer
sPDA08	Phillips et al. (2008) parametrization scheme as implemented in the ART module
VIPS	Video Ice Particle Sampler
VOC	Volatile Organic Compound
welas	WhitE-Light Aerosol Spectrometer system
wt%	weigth percentage, means fraction as percentage by mass

Bibliography

American Meteorological Society, 2016: Glossary of meteorology. URL http://glossary.ametsoc.org/wiki/Main_Page.

Andreae, M., D. Hegg, and U. Baltensperger, 2009: Sources and Nature of Atmospheric Aerosols. *Aerosol Pollution Impact on Precipitation - A Scientific Review*, Levin, Z. and W. Cotton, Eds., Springer Netherlands, 1st ed., chap. 3, 45–89.

Ansmann, A., M. Tesche, D. Althausen, D. Müller, P. Seifert, V. Freudenthaler, B. Heese, M. Wiegner, G. Pisani, P. Knippertz, and O. Dubovik, 2008: Influence of saharan dust on cloud glaciation in southern morocco during the saharan mineral dust experiment. *J. Geophys. Res.*, **113**, D04 210, doi:10.1029/2007JD008785.

Atkinson, J., B. Murray, M. Woodhouse, T. Whale, K. Baustian, K. Carslaw, S. Dobbie, D. O'Sullivan, and T. Malkin, 2013: The importance of feldspar for ice nucleation by mineral dust in mixed-phase clouds. *Nature*, **498**, 355–358, doi:10.1038/nature12278.

Bangert, M., 2012: Interaction of aerosol, clouds, and radiation on the regional scale. Ph.D. thesis, Karlsruhe Institute of Technology, URL http://www.imk-tro.kit.edu/download/Dissertation_Bangert.pdf.

Bangert, M., A. Nenes, B. Vogel, H. Vogel, D. Barahona, V. Karydis, P. Kumar, C. Kottmeier, and U. Blahak, 2012: Saharan dust event impact on cloud formation and radiation over western Europe. *Atmos. Chem. Phys.*, **12**, 4045–4063, doi:10.1021/ef9008746.

Barahona, D., 2012: On the ice nucleation spectrum. *Atmos. Chem. Phys.*, **12**, 3733–3752, doi:10.5194/acp-12-3733-2012.

Barahona, D. and A. Nenes, 2008: Parameterization of cirrus cloud formation in large-scale models: Homogeneous nucleation. *J. Geophys. Res.*, **113**, D11 211, doi:10.1029/2007JD009355.

———, 2009a: Parameterizing the competition between homogeneous and heterogeneous freezing in cirrus cloud formation - monodispers ice nuclei. *Atmos. Chem. Phys.*, **9**, 369–381, URL www.atmos-chem-phys.net/9/369/2009/.

———, 2009b: Parameterizing the competition between homogeneous and heterogeneous freezing in ice cloud formation - polydispers ice nuclei. *Atmos. Chem. Phys.*, **9**, 5933–5948, URL www.atmos-chem-phys.net/9/5933/2009/.

Barahona, D., J. Rodriguez, and A. Nenes, 2010: Sensitivity of the global distribution of cirrus ice crystal concentration to heterogeneous freezing. *J. Geophys. Res.*, **115**, D23 213, doi:10.1029/2010JD014273.

Benz, S., K. Megahed, O. Möhler, H. Saathoff, R. Wagner, and U. Schurath, 2005: T-dependent rate measurements of homogeneous ice nucleation in cloud droplets using a large atmospheric simulation chamber. *J. Photochem. Photobiol. A*, **176**, 208–217, doi:10.1016/j.jphotochem.2005.08.026.

Blatt, N., 2002: Charakterisierung von Rußaerosol durch thermische Analyse. Master's thesis, University of Karlsruhe.

Bond, T., S. Doherty, D. Fahey, P. Forster, T. Berntsen, B. DeAngelo, M. Flanner, S. Ghan, B. Kärcher, D. Koch, S. Kinne, Y. Kondo, P. Quinn, M. Sorafim, M. Schultz, M. Schulz, C. Venkataraman, H. Zhang, S. Zhang, N. Bellouin, S. Guttikunda, P. Hopke, M. Jacobson, J. Kaiser, Z. Klimont, U. Lohmann, J. Schwarz, D. Shindell, T. Storelvmo, S. Warren, and C. Zender, 2013: Bounding the role of black carbon in the climate system: A scientific assessment. *J. Geophys. Res. Atmos.*, **118**, 5380–5552, doi:10.1002/jgrd.50171.

Boucher, O., D. Randall, P. Artaxo, C. Bretherton, G. Feingold, P. Forster, V.-M. Kerminen, Y. Kondo, H. Liao, U. Lohmann, P. Rasch, S. Satheesh, S. Sherwood, B. Stevens, and X. Zhang, 2013: Clouds and Aerosols. *Climate Change 2013: The Physical Science Basis. Contribution of Working Group I to he Fifth Assessment Report of the Intergovernmental Panel on Climate Change*, Stocker, T., D. Quin, G.-K. Plattner, M. Tignor, S. Allen, J. Boschung, Y. Nauels, A. ans Xia, V. Bex, and P. Midgley, Eds., Cambridge University Press, Cambridge, United Kingdom and New York, NY, USA, doi:10.1017/CBO9781107415324.016.

Chen, J.-P., A. Hazra, and Z. Levin, 2008: Parameterizing ice nucleation rate using contact angle and activation energy derived from laboratory data. *Atmos. Chem. Phys.*, **8**, 7431–7449, URL www.atmos-chem-phys.net/8/7431/2008/.

Colorado State University, 2011: NWS DIFAX weather map archive. Department of Atmospheric Science, http://archive.atmos.colostate.edu/data/misc/QHTA11/1104/.

Connolly, P., O. Möhler, P. Field, H. Saathoff, R. Burgess, T. Choularton, and M. Gallagher, 2009: Studies of heterogeneous freezing by three different desert dust samples. *Atmos. Chem. Phys.*, **9**, 2805–2824, URL www.atmos-chem-phys.net/9/2805/2009/.

Crawford, I., O. Möhler, M. Schnaiter, H. Saathoff, D. Liu, G. McMeeking, C. Linke, M. Flynn, K. Bower, P. Connolly, M. Gallagher, and H. Coe, 2011: Studies of propane flame soot acting as heterogeneous ice nuclei in conjunction with single particle soot photometer measurements. *Atmos. Chem. Phys.*, **11**, 9549–9561, doi:10.5194/acp-11-9549-2011.

Curry, J. and V. Khvorostyanov, 2012: Experiment of some parameterizations of heterogeneous ice nucleation in cloud and climate models. *Atmos. Chem. Phys.*, **12**, 1151–1172, doi:10.5194/acp-12-1151-2012.

Cziczo, D. and K. Froyd, 2014: Sampling the composition of cirrus ice residuals. *Atmos. Res.*, **142**, 15–31, doi:10.1016/j.atmosres.2013.06.012.

Cziczo, D., K. Froyd, S. Gallavardin, O. Möhler, S. Benz, H. Saathoff, and D. Murphy, 2009: Deactivation of ice nuclei due to atmospherically relevant surface coatings. *Environ. Res. Lett.*, **4**, 044 013, doi:10.1088/1748-9326/4/4/044013.

Cziczo, D., K. Froyd, C. Hoose, E. Jensen, M. Dioa, M. Zondlo, J. Smith, C. Twohy, and D. Murphy, 2013: Clarifying the dominant sources and mechanisms of cirrus cloud formation. *Science*, **340**, 1320–1324, doi:10.1126/science.1234145.

Cziczo, D., D. Thomson, T. Thompson, P. DeMott, and D. Murphy, 2006: Particle anaysis by laser mass spectrometer (PALMS) studies of ice nuclei and other low number density particles. *Int. J. Mass Spectrom.*, **258**, 21–29, doi:10.1016/j.ijms.2006.05.013.

DeCarlo, P., J. Slowik, D. Worsnop, P. Davidovits, and J. Jimenez, 2004: Particle Morphology and Density Characterization by Combined Mobility and Aerodynamic Diameter Measurements. Part 1: Theory. *Aerosol Science and Technology*, **38**, 1185–1205, doi:10.1080/027868290903907.

DeMott, P., 1990: An exploratory study of ice nucleation by soot aerosols. *J. Appl. Meteorol.*, **29**, 1072–1079.

DeMott, P., Y. Chen, S. Kreidenweis, D. Rogers, and D. Sherman, 1999: Ice formation by black carbon particles. *Geophys. Res. Lett.*, **26**, 2429–2432.

DeMott, P., D. Cziczo, A. Prenni, D. Murphy, S. Kreidenweis, D. Thomson, R. Borys, and D. Rogers, 2003: Measurements of the concentration and composition of nuclei for cirrus formation. *Proc. Natl. Acad. Sci. USA*, **100**, 14 655–14 660, doi:10.1073/pnas.2532677100.

DeMott, P., T. Hill, C. McCluskey, K. Prather, D. Collins, R. Sullivan, M. Ruppel, R. Mason, V. Irish, T. Lee, C. Hwang, T. Rhee, J. Snider, G. McMeeking, S. Dhaniyala, E. Lewis, J. Wentzell, J. Abbatt, C. Lee, C. Sultana, A. Ault, J. Axson, M. Martinez, I. Venero, G. Santos-Figueroa, M. Stokes, G. Deane, O. Mayol-Bracero, V. Grassian, T. Bertram, A. Bertram, B. Moffett, and G. Franc, 2015: Sea spray aerosol as a unique source of ice nucleating particles. *Proc. Natl. Acad. Sci. USA*, **113**, 5797–5803, doi:10.1073/pnas.1514034112.

DeMott, P., O. Möhler, O. Stetzer, G. Vali, Z. Levin, M. Petters, M. Murakami, T. Leisner, U. Bundke, H. Klein, Z. Kanji, R. Cotton, H. Jones, S. Benz, M. Brinkmann, D. Rzesanke, H. Saathoff, M. Nicolet, A. Saito, B. Nillius, H. Bingemer, J. Abbatt, K. Ardon, E. Ganor, D. Georgakopoulos, and C. Saunders, 2011: Resurgence in ice nuclei measurement research. *Bull. Amer. Meteor. Soc.*, **92**, 1623–1635, doi:10.1175/2011BAMS3119.1.

DeMott, P., M. Petters, A. Prenni, C. Carrico, S. Kreidenweis, J. Collet Jr., and H. Moosmüller, 2009: Ice nucleation behavior of biomass combustion particles at cirrus temperatures. *J. Geophys. Res.*, **114**, D16 205, doi:10.1029/2009JD012036.

DeMott, P., A. Prenni, X. Liu, S. Kreidenweis, M. Peter, C. Twohy, M. Richardson, T. Eidhammer, and D. Rogers, 2010: Predicting global atmospheric ice nuclei distributions and their impact on climate. *Proc. Natl. Acad. Sci. USA*, **107 (25)**, 11 217–11 222, URL www.pnas.org/cgi/doi/10.1073/pnas.0910818107.

Diehl, K. and S. Mitra, 1998: A laboratory study of the effects of a kerosene-burner exhaust on ice nucleation and the evaporation rate of ice crystals. *J. Atmos. Env.*, **32**, 3145–3151.

Emmons, L., S. Walter, P. Hess, J.-F. Lamarque, G. Pfister, D. Fillmore, C. Granier, A. Guenther, D. Kinnison, T. Laepple, J. Orlando, X. Tie, G. Tyndall, C. Wiedinmyer, S. Baughcum, and S. Kloster, 2010: Description and evaluation of the model for ozone and related chemical tracers, version 4 (mozart-4). *Geosci. Model Dev.*, **3**, 43–67, URL www.geosci-model-dev.net/3/43/2010/.

Fahey, D., R.-S. Gao, O. Möhler, H. Saathoff, C. Schiller, V. Ebert, M. Krämer, T. Peter, N. Amarouche, L. Avallone, R. Bauer, Z. Bozóki, L. Christensen, S. Davis, G. Durry,

C. Dyroff, R. Herman, S. Hunsmann, S. Khaykin, P. Mackrodth, J. Meyer, J. Smith, N. Spelten, R. Troy, H. Vömel, S. Wagner, and F. Wienhold, 2014: The AquaVIT-1 intercomparison of atmospheric water vapor measurement techniques. *Atmos. Meas. Tech.*, **7**, 3177–3213, doi:10.5194/amt-7-3177-2014.

Field, P., O. Möhler, P. Connolly, M. Krämer, R. Cotton, A. Heymsfield, H. Saathoff, and M. Schnaiter, 2006: Some ice nucleation characteristics of Asian and Saharan desert dust. *Atmos. Chem. Phys.*, **6**, 2991–3006, URL www.atmos-chem-phys.net/6/2991/2006/.

Gal-Chen, T. and R. Somerville, 1975: On the use of a coordinate transformation for the solution of the Navier-Stokes equations. *J. Comput. Phys.*, **17**, 209–228.

Gettelman, A., X. Liu, S. Ghan, H. Morrison, S. Park, A. Conley, S. Klein, J. Boyle, D. Mitchell, and J.-L. Li, 2010: Global ssimulation of ice nucleation and ice supersaturation with an iimprove cloud scheme in the community atmosphere model. *J. Geophys. Res.*, **115**, D18 216, doi:10.1029/2009JD013797.

Grice, S., J. Stedman, A. Kent, M. Hobson, J. Norris, J. Abbott, and S. Cooke, 2009: Recent trends and projections of primary NO_2 emissions in Europe. *Atmos. Env.*, **43**, 2154–2167.

Hande, L., C. Engler, C. Hoose, and I. Tegen, 2015: Seasonal variability of Saharan desert dust and ice nucleating particles over Europe. *Atmos. Chem. Phys.*, **15**, 4389–4397, doi:10.5194/acp-15-4389-2015.

Heintzenberg, J., 1994: Properties of the log-normal particle size distribution. *Aerosol Science and Technology*, **21:1**, 46–48, doi:10.1080/02786829408959695.

Henning, S., M. Ziese, A. Kiselev, H. Saathoff, O. Möhler, T. Mentel, A. Buchholz, C. Spindler, V. Michaud, M. Monier, K. Sellegri, and F. Stratmann, 2012: Hygroscopic growth and droplet activation of soot particles: uncoated, succinic or sulphuric acid coated. *Atmos. Chem. Phys.*, **12**, 4525–4537, doi:10.5194/acp-12-4525-2012.

Hill, T., P. DeMott, Y. Tobo, J. Fröhlich-Nowoisky, B. Moffett, G. Franc, and S. Kreidenweis, 2016: Sources of organic ice nucleating particles in soils. *Atmos. Chem. Phys.*, **16**, 7195–7211, doi:10.5194/acp-16-7195-2016.

Hiranuma, N., S. Augustin-Bauditz, H. Bingemer, C. Budke, J. Curtius, A. Danielczok, K. Diehl, K. Dreischmeier, M. Ebert, F. Frank, N. Hoffmann, K. Kandler, A. Kiselev, T. Koop, T. Leisner, O. Möhler, B. Nillius, A. Peckhaus, D. Rose, S. Weinbruch, H. Wex, Y. Boose, P. DeMott, J. Hader, T. Hill, Z. Kanji, G. Kulkarni, E. Levin,

C. McCluskey, M. Murakami, B. Murray, D. Niedermeier, M. Petters, D. O'Sullivan, A. Saito, G. Schill, T. Tajiri, M. Tolbert, A. Welti, T. Whale, T. Wright, and K. Yamashita, 2015: A comprehensive laboratory study on the immersion freezing behavior of illite NX particles: a acomparison of seventeen ice nucleation measurement techniques. *Atmos. Chem. Phys.*, **15**, 2489–2518, doi:10.5194/acp-15-2489-2015.

Hiranuma, N., N. Hoffmann, A. Kiselev, A. Dreyer, K. Zhang, G. Kulkarni, T. Koop, and O. Möhler, 2014a: Influence of surface morphology on the immersion mode ice nucleation efficiency of hematite particles. *Atmos. Chem. Phys.*, **14**, 2315–2324, doi:10.5194/acp-14-2315-2014.

Hiranuma, N., M. Paukert, I. Steinke, K. Zhang, G. Kulkarni, C. Hoose, M. Schnaiter, H. Saathoff, and O. Möhler, 2014b: A comprehensive parameterization of heterogeneous ice nucleation of dust surrogate: laboratory study with hematite particles and its application to atmospheric models. *Atmos. Chem. Phys.*, **14**, 13 135–13 158, doi:10.5194/acp-14-13145-2014.

Hoose, C. and O. Möhler, 2012: Heterogeneous ice nucleation on atmospheric aerosols: a review of results from laboratory experiments. *Atmos. Chem. Phys.*, **12**, 9817–9854, doi:10.5194/acp-12-9817-2012.

Hoose, J., C.and Kristjánsson, J.-P. Chen, and A. Hazra, 2010: A classical-theory-based parameterization of heterogeneous ice nucleation by mineral dust, soot, and biological particles in a global climate model. *J. Atmos. Sci.*, **67**, 2483–2503, doi:10.1175/2010JAS3425.1.

Ickes, L., A. Welti, C. Hoose, and U. Lohmann, 2015: Classical nucleation theory of homogeneous freezing of water: thermodynamic and kinetic parameters. *Phys. Chem. Chem. Phys.*, doi:10.1039/c4cp04184d.

Janssens-Maenhout, G., F. Dentener, J. van Aardenn, S. Monni, V. Pagliari, L. Orlandini, Z. Klimont, J. Kurokawa, H. Akimoto, T. Ohara, R. Wankmüller, B. Battye, D. Grano, A. Zuber, and T. Keating, 2012: EDGAR-HTAP: a harmonized gridded air pollution emission datdata based on national inventories. Tech. rep., European Commision Joint Reseach Centre, Institute for Environment and Sustainability.

Jensen, E., R. Lawson, J. Bergman, L. Pfister, T. Bui, and C. Schmitt, 2013: Physical processes controlling ice concentrations in synoptically forced midlatitude cirrus. *J. Geophys. Res. Atmos.*, **118**, 1–13, doi:doi:10.1002/jgrd.50421.

Jensen, E., L. Pfister, T.-P. Bui, P. Lawson, and D. Baumgardner, 2010: Ice nucleation and cloud microphysical properties in tropical tropopause layer cirrus. *Atmos. Chem. Phys.*, **10**, 1369–1384, doi:10.5194/acp-10-1369-2010.

Jensen, E. and O. Toon, 1997: The potential impact of soot particles from aircraft exhaust on cirrus clouds. *Geophys. Res. Lett.*, **24**, 249–252, doi:10.1029/96GL03235.

Jones, J., A. Saginor, and B. Smith, 2011: *2011 Texas Wildfires - Common Denominators of Home Destruction*. Texas A&M Forest Service, URL http://texasforestservice.tamu.edu/uploadedFiles/TFSMain/Preparing_for_Wildfires/Prepare_Your_Home_for_Wildfires/Contact_Us/2011%20Texas%20Wildfires.pdf.

Jonsson, H., J. Wilson, C. Brock, R. Knollenberg, R. Newton, J. Dye, D. Baumgardner, S. Borrmann, G. Ferry, R. Pueschel, D. Woods, and M. Pitts, 1995: Performance of a Focused Cavity Aerosol Spectrometer for measurements in the stratosphere of particle size in the 0.06-2.0-μm-diameter range. *J. Atmos. Ocean. Technol.*, **12**, 115–129.

Kaaden, N., A. Massling, A. Schladitz, T. Müller, K. Kandler, L. Schütz, B. Weinzierl, A. Petzold, M. Tesche, S. Leinert, C. Deutscher, M. Ebert, S. Weinbruch, and A. Wiedensohler, 2009: State of mixing, shape factor, number size distribution and hygroscopic growth of the Saharan anthropogenic and mineral dust aerosol at Tinfou, Morocco. *Tellus*, **61B**, 51–63, doi:10.1111/j.1600-0889.2008.00388.x.

Kamphus, M., M. Ettner-Mahl, T. Klimach, F. Drewnick, L. Keller, D. Cziczo, S. Mertes, S. Borrmann, and J. Curtius, 2010: Chemical composition of ambient aerosol, ice residues and cloud droplet residues in mixed-phase clouds: single particle analysis during the Cloud and Aerosol Characterization Experiment (CLACE 6). *Atmos. Chem. Phys.*, **10**, 8077–8095, doi:10.5194/acp-10-8077-2010.

Kanji, Z., P. DeMott, O. Möhler, and J. Abbatt, 2011: Results from theUniversity of Toronto continuous flow diffusion chamber at ICIS 2007: instrument intercomparison and ice onsets for different aerosol types. *Atmos. Chem. Phys.*, **11**, 31–41, doi: doi:10.5194/acp-11-31-2011.

Kärcher, B., J. Hendricks, and U. Lohmann, 2006: Physical based parameterization of cirrus cloud formation for use in global models. *J. Geophys. Res.*, **111**, D01 205, doi:10.1029/2005JD006219.

Kärcher, B., O. Möhler, P. DeMott, S. Pechtl, and F. Yu, 2007: Insights into the role of soot aerosol in cirrus cloud formation. *Atmos. Chem. Phys.*, **7**, 4203–4227, URL www.atmos-chem-phys.net/7/4203/2007/.

Kärcher, B. and P. Spichtinger, 2009: Cloud-controlling factors of cirrus. *Clouds in the Perturbed Climate System: Their Relationship to Energy Balance, Atmospheric Dynamics, and Precipitation, Strüngemann Forum Report*, Heintzenberg, J. and R. Charlson, Eds., MIT press, chap. 11, 235–268.

Khain, A., K. Beheng, A. Heymsfield, A. Korolev, S. Krichak, Z. Levin, M. Pinsky, V. Phillips, T. Prabhakaran, A. Teller, S. van den Heever, and J.-I. Yano, 2015: Representation of microphysical processes in cloud-resolving models: Spectral (bin) microphysics versus bulk parameterization. *Rev. Geophys.*, **53**, 247–322, doi:10.1002/2014RG000468.

Kienast-Sjögren, E., A. Miltenberger, B. Luo, and T. Peter, 2015: Sensitivities of lagrangian modeling of mid-latitude cirrus clouds to tranjectory data quality. *Atmos. Chem. Phys.*, **15**, 7429–7447, doi:10.5194/acp-15-7429-2015.

Knote, C., 2012: Regional scale impact of changing anthropogenic emissions on aerosol. Ph.D. thesis, ETH Zurich.

Koehler, K., P. DeMott, S. Kreidenweis, O. Popovicheva, M. Petters, C. Carrico, E. Kireeva, T. Khokhlova, and N. Shonija, 2009: Cloud condensation nuclei and ice nucleation activity of hydrophobic and hydrophilic soot particles. *Phys. Chem. Chem. Phys.*, **11**, 7909–7920.

Koehler, K., S. Kreidenweis, P. DeMott, M. Petters, A. Prenni, and O. Möhler, 2010: Laboratory investigation of the impact of mineral dust aerosol on cold cloud formation. *Atmos. Chem. Phys.*, **10**, 11 955–11 968, doi:10.5194/acp-10-11955-2010.

Koop, T., B. Luo, A. Tsias, and T. Peter, 2000: Water activity as the determinant for homogeneous ice nucleation in aqueous solutions. *Nature*, **406**, 611–614.

Krämer, M., C. Rolf, A. Luebke, A. Afchine, N. Spelten, A. Costa, J. Meyer, M. Zöger, J. Smith, R. Herman, B. Buchholz, V. Ebert, D. Baumgardner, S. Borrmann, M. Klingebiel, and L. Avallone, 2016: A microphysics guide to cirrus clouds - part 1: Cirrus types. *Atmos. Chem. Phys.*, **16**, 3463–3483, doi:10.5194/acp-16-3463-2016.

Krämer, M., C. Schiller, A. Afchine, R. Bauer, I. Gensch, A. Mangold, S. Schlicht, N. Spelten, N. Sitnikov, S. Borrmann, M. de Reus, and P. Spichtinger, 2009: Ice

supersaturation and cirrus cloud crystals numbers. *Atmos. Chem. Phys.*, **9**, 3505–3522, doi:10.5194/acp-9-3505-2009.

Laborde, M., M. Schnaiter, C. Linke, H. Saathoff, K.-H. Naumann, O. Möhler, S. Berlenz, U. Wagner, J. Taylor, D. Liu, M. Flynn, J. Allan, H. Coe, K. Heimerl, F. Dahlkötter, B. Weinzierl, A. Wollny, M. Zanatta, J. Cozic, P. Laj, R. Hitzenberger, J. Schwarz, and M. Gysel, 2012: Single particle soot photometer intercomparison at the AIDA chamber. *Atmos. Meas. Tech.*, **5**, 3077–3097, doi:10.5194/amt-5-3077-2012.

Lamb, D. and J. Verlinde, 2011: *Physics and Chemistry of Clouds*. Cambridge University Press.

Lawson, R., B. Baker, B. Pilson, and Q. Mo, 2006a: In situ observations of the microphysical properties of wave, cirrus, and anvil clouds. part ii: Cirrus clouds. *J. Atmos. Sci.*, **63**, 3186–3203.

Lawson, R., D. O'Connor, P. Zmarzly, K. Weaver, B. Baker, Q. Mo, and H. Jonsson, 2006b: The 2D-S probe: Design and preliminary ttest of a new airborne, high-speed, high resolution particle imaging probe. *J. Atmos. Oceanic Technol.*, **23**, 1462–1477.

Linke, C., O. Möhler, A. Veres, A. Moháesi, Z. Bozóki, G. Szabó, and M. Schnaiter, 2006: Optical properties and mineralogical composition of different Saharan mineral dust samples: a laboratory study. *Atmos. Chem. Phys.*, **6**, 3315–3323, URL www.atmos-chem-phys.net/6/3315/2006/.

Lohmann, U., F. Lüönd, and F. Mahrt, 2016: *An introduction to Clouds: From Microscale to Climate*. 1st ed., Cambridge University Press.

Lundgren, K., B. Vogel, H. Vogel, and C. Kottmeier, 2013: Direct radiative effects of sea salt for the Mediterranean region under conditions of low to moderate wind speeds. *J. Geophys. Res.*, **118**, 1906–1923, doi:10.1029/2012JD018629.

Marcolli, C., 2014: Deposition nucleation viewed as homogeneous or immersion freezing in pores and cavities. *Atmos. Chem. Phys.*, **14**, 2071–2104, doi:10.5194/acp-14-2071-2014.

Megahed, K., 2007: The impact of mineral dust aerosol particles on cloud formation. Ph.D. thesis, Rheinische Friedrich- Wilhelms- University Bonn.

Meyers, M., P. DeMott, and W. Cotton, 1992: New primary ice-nucleation parameterizations in an explicit cloud model. *J. Appl. Meteorol.*, **31**, 708–721.

Möhler, O., S. Benz, H. Saathoff, M. Schnaiter, R. Wagner, J. Schneider, S. Walter, V. Ebert, and S. Wagner, 2008: The effect of organic coating on the heterogeneous ice nucleation efficiency of mineral dust aerosols. *Environ. Res. Lett.*, **3**, 025 007, doi:10.1088/1748-9326/3/2/025007.

Möhler, O., S. Büttner, C. Linke, M. Schnaiter, H. Saathoff, O. Stetzer, R. Wagner, M. Krämer, A. Mangold, V. Ebert, and U. Schurath, 2005a: Effect of sulphuric acid coating on heterogeneous ice nucleation by soot aerosol particles. *J. Geophys. Res.*, **110**, D11 210, doi:10.1029/2004JD005169.

Möhler, O., P. Field, P. Connolly, S. Benz, H. Saathoff, M. Schnaiter, R. Wagner, R. Cotton, M. Krämer, A. Mangold, and A. Heymsfield, 2006: Efficiency of the deposition mode ice nucleation on mineral dust particles. *Atmos. Chem. Phys.*, **6**, 3007–3021, URL www.atmos-chem-phys.net/6/3007/2006/.

Möhler, O., C. Linke, H. Saathoff, M. Schnaiter, R. Wagner, A. Mangold, M. Krämer, and U. Schurath, 2005b: Ice nucleation on flame soot aerosol of different organic carbon content. *Meteorol. Z.*, **14**, 477–484, doi:10.1127/0941-2948/2005/0055.

Murray, B., S. Broadley, T. Wilson, J. Atkinson, and R. Wills, 2011: Heterogeneous freezing of water droplets containing kaolinite particles. *Atmos. Chem. Phys.*, **11**, 4191–4207, doi:10.5194/acp-11-4191-2011.

Murray, B., D. O'Sullivan, J. Atkinson, and M. Webb, 2012: Ice nucleation by particles immersed in supercooled cloud droplets. *Chem. Soc. Rev.*, **41**, 6519–6554, doi:10.1039/c2cs35200a.

NASA, 2011: VISST cloud product - MACPEX GEOS-E. Minnis, P., (Ed.), Langley Cloud and Radiation Research, URL http://cloudsgate2.larc.nasa.gov/cgi-bin/site/showdoc?docid=22&domain=MACPEX_GOES-EAST&lkdomain=Y.

NASA, 2012a: NASA airborne science instrument database. Justice, E., (Ed.), URL https://airbornescience.nasa.gov/instrument/all.

NASA, 2012b: NASA ESPO data archive - MACPEX WB-57 platform. Justice, E., (Ed.), URL https://espo.nasa.gov/macpex/archive/browse/macpex.

NASA FIRMS, 2012: MODIS Hotspot Active Fire Detection. URL https://firms.modaps.eosdis.nasa.gov/firemap/.

Niedermeier, D., R. Shaw, S. Hartmann, H. Wex, T. Clauss, J. Voigtländer, and F. Stratmann, 2011: Heterogeneous ice nucleation: exploring the transition from

stochastic to singular freezing behavior. *Atmos. Chem. Phys.*, **11**, 8767–8775, doi:10.5194/acp-11-8767-2011.

Nielsen-Gammon, J., 2011: *The 2011 Texas Drought*. The Office of the State Climatologist, Texas, URL http://climatexas.tamu.edu/index.php/drought.

Niemand, M., O. Möhler, B. Vogel, H. Vogel, C. Hoose, P. Connolly, H. Klein, H. Bingemer, P. DeMott, J. Skrotzki, and T. Leisner, 2012: A particle-surface-area-based parameterization of immersion freezing on desert dust particles. *J. Atmos. Sci.*, **69**, 3077–3092, doi:10.1175/JAS-D-11-0249.1.

O'Sullivan, D., B. Murray, T. Malkin, T. Whale, N. Umo, J. Atkinson, H. Price, K. Baustian, J. Browse, and M. Webb, 2014: Ice nucleation by fertile soil dusts: relative importance of mineral and biogenic components. *Atmos. Chem. Phys.*, **14**, 1853–1867, doi:10.5194/acp-14-1853-2014.

Petters, M., M. Parson, A. Prenni, P. DeMott, S. Kreidenweis, C. Carrico, A. Sullivan, G. McMeeking, E. Levin, C. Wold, J. Collet Jr., and H. Moosmüller, 2009: Ice nuclei emissions from biomass burning. *J. Geophys. Res.*, **114**, D07 209, doi:10.1029/2008JD011532.

Petzold, A., A. Döpelheuer, C. Brock, and F. Schröder, 1999: In situ observations and model calculations of black carbon emission by aircraft at cruise altitude. *J. Geophys. Res.*, **104**, 22 171–22 181, doi:10.1029/1999JD900460.

Phillips, V., P. DeMott, and C. Andronache, 2008: An empirical parameterization of heterogeneous ice nucleation for multiple chemical species of aerosol. *J. Atmos. Sci.*, **65**, 2725–2783, doi:10.1175/2007JAS2546.1.

Phillips, V., P. DeMott, C. Andronache, K. Pratt, K. Prather, R. Subramanian, and C. Twohy, 2013: Improvements to an empirical parameterization of heterogeneous ice nucleation and its comparison with observations. *J. Atmos. Sci.*, **70**, 378–409, doi:10.1175/JAS-D-12-080.1.

Phillips, V., L. Donner, and S. Garner, 2007: Nucleation processes in deep convection simulated by a cloud-system-resolving model with double-moment bulk microphysics. *J. Atmos. Sci.*, **64**, 738–761, doi:10.1175/JAS3869.1.

Pratt, K., P. DeMott, J. French, Z. Wang, D. Westphal, A. Heymsfield, C. Twohy, A. Prenni, and K. Prather, 2009: In situ detection of biological particles in cloud ice-crystals. *Nature Geosci.*, **2**, 398–401, doi:10.1038/NGEO521.

Prenni, A., J. Harrington, M. Tjernström, P. DeMott, A. Avramov, C. Long, S. Kreidenweis, P. Olsson, and J. Verlinde, 2007: Can ice-nucleating aerosols affect arctic seasonal climate? *Bull. Amer. Meteor. Soc.*, **88**, 541–550, doi:10.1175/BAMS-88-4-541.

Raes, F., R. Van Dingenen, E. Vignati, J. Wilson, J.-P. Putaud, S. J.H., and P. Adams, 2000: Formation and cycling of aerosols in the global troposphere. *Atmos. Env.*, **34**, 4215–4240.

Ren, C. and A. MacKenzie, 2005: Cirrus parameterization and the role of ice nuclei. *Q. J. R. Meteorol. Soc.*, **131**, 1585–1605, doi:10.1256/qj.04.126.

Rieger, D., M. Bangert, I. Bischoff-Gauss, J. Förstner, K. Lundgren, D. Reinert, J. Schröter, H. Vogel, G. Zängl, R. Ruhnke, and B. Vogel, 2015: ICON-ART 1.0 - a new online-coupled model system from the global to the regional scale. *Geosci. Model Dev.*, **8**, 1659–1676, doi:10.5194/gmd-8-1659-2015.

Roedel, W. and T. Wagner, 2011: *Physik unserer Umwelt: Die Atmosphäre*. 4th ed., Springer-Verlag Berlin Heidelberg.

Saathoff, H., K.-H. Naumann, M. Schnaiter, W. Schöck, E. Weingartner, U. Baltensperger, L. Krämer, Z. Bozóki, U. Pöschl, R. Niessner, and U. Schurath, 2003: Carbon mass determinations during the AIDA soot aerosol campaign 1999. *J. Aerosol Sci.*, **34**, 1399–1420, doi:10.1016/S0021-8502(03)00365-3.

Savre, J. and A. Ekman, 2015: A theory-based parameterization for heterogeneous ice nucleation and implications for the simulation of ice processes in atmospheric models. *J. Geophys. Res. Atmos.*, **120**, 4937–4961, doi:10.1002/2014JD023000.

Schaap, M., H. Denier Van Der Gon, F. Dentener, A. Visschedijk, M. Van Loon, H. ten Brink, J.-P. Putaud, B. Guillaume, C. Liousse, and P. Builtjes, 2004: Anthropogenic black carbon and fine aerosol distribution over Europe. *J. Geophys. Res.*, **109**, D18 207, doi:10.1029/2003JD004330.

Schell, B., I. Ackermann, H. Hass, F. Binkowski, and A. Ebel, 2001: Modeling the formation of secondary organic aerosol wiwith a comprehensive air quality model system. *J. Geophys. Res.*, **106 (D22)**, 28 275–28 293.

Schiebel, T., 2014: Homogeneous freezing of water droplets and its dependence on droplet size. Master's thesis, Karlsruhe Institute of Technology.

Schill, G., S. Jathar, J. Kodros, E. Levin, A. Galang, B. Friedman, M. Link, D. Farmer, J. Pierce, S. Kreidenweis, and P. DeMott, 2016: Ice-nucleating particle emissions

from photochemically aged diesel and biodiesel exhaust. *Geophys. Res. Lett.*, **43**, doi:10.1002/2016GL069529.

Schmitt, C., M. Schnaiter, A. Heymsfield, P. Yang, E. Hirst, and A. Bansemer, 2016: The microphysical properties os small ice particles measured by the small ice detector - 3 probe during the macpex field campaign. *J. Atmos. Sci.*, in press., doi:10.1175/JAS-D-16-0126.

Schnaiter, M., M. Gimmler, I. Llamas, C. Linke, C. Jäger, and H. Mutschke, 2006: Strong spectral dependence of light absorption by organic carbon particles formed by propane combustion. *Atmos. Chem. Phys.*, **6**, 2981–2990, URL www.atmos-chem-phys.net/6/2981/2006/.

Schwarz, J., R. Gao, D. Fahey, D. Thomson, L. Watts, J. Wilson, J. Reeves, M. Darbeheshti, D. Baumgardner, G. Kok, S. Chung, M. Schulz, J. Hendricks, B. Kärcher, J. Slowik, K. Rosenlof, T. Thompson, A. Langford, M. Loewenstein, and K. Aikin, 2006: Single-particle measurements of midlatitude black carbon and light-scattering aerosols from the boundary layer to the lower stratosphere. *J. Geophys. Res.*, **111**, D16 207, doi:10.1029/2006JD007076.

Scott, S., T. Bui, K. Chan, and S. Bowen, 1990: The Meteorological Measrurement System on the NASA ER-2 aircraft. *J. Atmos. Ocean. Technol.*, **7 (4)**, 525–540.

Seifert, A. and K. Beheng, 2001: A double-moment parameterization for simulating autoconversion, accretion and selfcollection. *Atmos. Res.*, **59-60**, 265–291.

———, 2006: A two-moment cloud microphysics parameterization for mixed-phase clouds. part 1: Model description. *Meteorol. Atmos. Phys.*, **92**, 45–66, doi:10.1007/s00703-005-0112-4.

Seinfeld, J. and S. Pandis, 1998: *Atmospheric Chemistry and Physics: From Air Pollution to Climate Change*. 1st ed., A Wiley interscience publication, Wiley.

Spice, A., D. Johnson, P. Brown, A. Darlison, and C. Saunders, 1999: Primary ice nucleation in orographic cirrus clouds: A numerical simulation of microphysics. *Q. J. R. Meteorol. Soc.*, **125**, 1637–1667, doi:10.1002/qj.49712555708.

Spichtinger, P. and D. Cziczo, 2010: Impact of heterogeneous ice nuclei on homogeneous freezing events in cirrus clouds. *J. Geophys. Res.*, **115**, D14 208, doi:10.1029/2009JD012168.

Steinke, I., R. Funk, J. Busse, A. Iturri, S. Kirchen, M. Leue, O. Möhler, T. Schwartz, M. Schnaiter, B. Sierau, E. Toprak, R. Ullrich, A. Ulrich, C. Hoose, and T. Leisner, 2016: Ice nucleation activity of agricultural soil dust aerosols from Mongolia, Argentina and Germany. *J. Geophys. Res. Atmos.*, **121**, doi:10.1002/2016JD025160.

Steinke, I., C. Hoose, O. Möhler, P. Connolly, and T. Leisner, 2015: A new temperature- and humidity-dependent surface site density approach for deposition ice nucleation. *Atmos. Chem. Phys.*, **15**, 3703–3717, doi:10.5194/acp-15-3703-2015.

Steinke, I., O. Möhler, A. Kiselev, M. Niemand, H. Saathoff, M. Schnaiter, J. Skrotzki, C. Hoose, and T. Leisner, 2011: Ice nucleation properties of fine ash particles from the Eyjafjallajökull eruption in April 2010. *Atmos. Chem. Phys.*, **11**, 12 945–12 958, doi:10.5194/acp-11-12945-2011.

Stier, P., J. Feichter, S. Kinne, S. Kloster, E. Vignati, J. Wilson, L. Ganzeveld, I. Tegen, M. Werner, Y. Balkanski, M. Schulz, O. Boucher, A. Minikin, and A. Petzold, 2005: The aerosol-climate model ECHAM5-HAM. *Atmos. Chem. Phys.*, **5**, 1125–1156, URL www.atmos-chem-phys.org/acp/5/1125/.

Textor, C., M. Schulz, S. Guibert, S. Kinne, Y. Balkanski, S. Bauer, T. Berntsen, T. Berglen, O. Boucher, M. Chin, F. Dentener, T. Diehl, J. Feichter, D. Fillmore, P. Ginoux, S. Gong, A. Grini, J. Hendricks, L. Horowitz, P. Huang, I. Isaksen, T. Iversen, S. Kloster, D. Koch, A. Kirkevåg, J. Kristjansson, M. Krol, A. Lauer, J. Lamarque, X. Liu, V. Montanaro, G. Myhre, J. Penner, G. Pitari, M. Reddy, O. Seland, P. Stier, T. Takemura, and X. Tie, 2007: The effect of harmonized emissions on aerosol properties in global models - an AeroCom experiment. *Atmos. Chem. Phys.*, **7**, 4489–4501, doi:10.5194/acp-7-4489-2007.

Thomson, D., M. Schein, and D. Murphy, 2000: Particle analysis by laser mass spectrometry WB-57F instrument overview. *Aerosol Science and Technology*, **33**, 153–169, doi:10.1080/027868200410903.

Thomson, E., X. Kong, P. Papagiannakopoulos, and J. Pettersson, 2015: Deposition-mode ice nucleation reexamined at temperatures below 200 K. *Atmos. Chem. Phys.*, **15**, 1621–1623, doi:10.5194/acp-15-1621-2015.

Tobo, Y., P. DeMott, T. Hill, A. Prenni, N. Swoboda-Colberg, G. Franc, and S. Kreidenweis, 2014: Organic matter matters for ice nuclei of agricultural soil origin. *Atmos. Chem. Phys.*, **14**, 8521–8531, doi:10.5194/acp-14-8521-2014.

Twohy, C. and M. Poellot, 2005: Chemical characteristics of ice residual nuclei in anvil cirrus clouds: evidence for homogeneous and heterogeneous ice formation. *Atm*, **5**, 2289–2297, URL www.atmos-chem-phys.org/acp/5/2289/.

University of Wyoming, 2011: Radio sounding. Oolman, L., (Ed.), Department of Atmospheric Science, URL http://weather.uwyo.edu/upperair/sounding.html.

Vali, G., 1971: Quantitative evaluation of experimental results on the heterogeneous freezing nucleation of supercooled liquids. *J. Atmos. Sci.*, **28**, 402–409.

Vali, G., P. DeMott, O. Möhler, and T. Whale, 2015: Technical note: A proposal for ice nucleation terminology. *Atmos. Chem. Phys.*, **15**, 10 263–10 270, doi:10.5194/acp-15-10263-2015.

VDI, 1999: Measurement of soot (ambient air) - thermographical determination of elemental carbon after thermal desorption of organic carbon. VDI/ DIN manual Air Pollution Prevention Volume 4: Analysis and Measurement Methods 2465/2, Beuth, Berlin, Germany.

Vochezer, P., E. Järvinen, R. Wagner, P. Kupiszewski, T. Leisner, and M. Schnaiter, 2016: In situ characterization of mixed phase clouds using the small ice detector and the particle phase discriminator. *Atmos. Meas. Tech.*, **9**, 159–177, doi:10.5194/amt-9-159-2016.

Vogel, B., C. Hoose, H. Vogel, and C. Kottmeier, 2006: A model of dust transport applied to the Dead Sea Area. *Meteorol. Z.*, **15**, 611–624, doi:10.1127/0941-2948/2006/0168.

Vogel, B., H. Vogel, D. Bäumer, M. Bangert, K. Lundgren, R. Rinke, and T. Stanelle, 2009: The comprehensive model system COSMO-ART - radiative impact of aerosol on the state of the atmosphere on the regional scale. *Atmos. Chem. Phys.*, **9**, 8661–8680, URL www.atmos-chem-phys.net/9/8661/2009/.

Wagner, R., A. Kiselev, O. Möhler, H. Saathoff, and I. Steinke, 2016: Pre-activation of ice-nucleating particles by the pore condensation and freezing mechanism. *Atmos. Chem. Phys.*, **16**, 2025–2042, doi:10.5194/acp-16-2025-2016.

Wagner, R. and O. Möhler, 2013: Heterogeneous ice nucleation ability of crystalline sodium chloride dihydrate particles. *J. Geophys. Res. Atmos.*, **118**, 4610–4622, doi:10.1002/jgrd.50325.

Walter, C., 2014: Einfluss von Aerosolpartikeln aus Vegetationsbränden auf die Wolkenbildung auf der regionalen Skala. Master's thesis, Karlsruhe Institute of Technology.

Weinstock, E., J. Smith, D. Sayres, J. Pittman, J. Spackman, E. Hintsa, T. Hanisco, E. Moyer, J. St. Clair, M. Sargent, and J. Anderson, 2009: Validation of the Havard Lyman-α in situ water vapor instrument: Implications for the meachanisms that control stratospheric water vapor. *J. Geophys. Res.*, **114**, D2331, doi: 10.1029/2009JD012427.

Welti, A., F. Lüönd, O. Stetzer, and U. Lohmann, 2009: Influence of particle size on the ice nucleating ability of mineral dusts. *Atmos. Chem. Phys.*, **9**, 6705–6715, URL www.atmos-chem-phys.net/9/6705/2009/.

Wentzel, M., H. Gorzawski, K.-H. Naumann, H. Saathoff, and S. Weinbruch, 2003: Transmission electron microscopical and aerosol dynamical characterization of soot aerosols. *J. Aerosol Sci.*, **34**, 1347–1370, doi:10.1016/S0021-8502(03)00360-4.

Whitby, K., 1978: The physical characteristics of sulfur aerosols. *Atmos. Env.*, **12**, 135–159.

Wicker, L. and W. Skamarock, 2002: Time-splitting methods for eleastic models using forward time schemes. *Mon. Weather Rev.*, **130**, 2088–2097.

Zobrist, B., T. Koop, B. Luo, C. Marcolli, and T. Peter, 2007: Heterogeneous ice nucleation rate coefficient of water droplet coated by a nonadecanol monolayer. *J. Phys. Chem. C*, **111**, 2149–2155, doi:10.1021/jp066080w.

Acknowledgements

First of all, I would like to thank Corinna Hoose, Ottmar Möhler and Thomas Leisner for giving me the chance to do my PhD and the opportunity to do research on this interesting topic. In particular, I thank you, Corinna and Ottmar, for the guidance and the enablement to visit a lot of conferences and therewith, to gain experiences.
Furthermore, I thank all colleagues at the AAF for the warm welcome.

I would like to thank Karl Froyd, Dan Cziczo, Shuka Schwarz, Carl Schmitt and Martin Schnaiter for providing the data sets from the MACPEX campaign and the support in the interpretation.
For the patient help by debugging the model, I want to mention Tobias Schad and Daniel Rieger.

At the end, I want to thank my family and my partner Carl for the non-scientific support and the sometimes needed diversion.